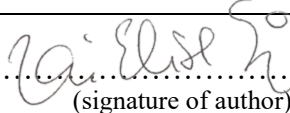




Universitetet
i Stavanger

FACULTY OF SCIENCE AND TECHNOLOGY

MASTER'S THESIS

Study programme/specialisation: Engineering Structures and Material	Spring / Autumn semester, 2019.. Open/ Confidential
Author: Kari Elise Nøstdahl Sørvåg	 (signature of author)
Programme coordinator: Supervisor(s): Jasna B. Jakobsen	
Title of master's thesis: Analysis of cable vibrations at Stavanger City bridge	
Credits: 30	
Keywords: Cable vibration Rain-wind induced vibration	Number of pages: 56..... + supplemental material/other: 23..... Stavanger, 14.06.2019..... date/year

Preface

This thesis marks the end of my master studies of Engineering Structures and Materials at the University of Stavanger. Immersing myself in the study of environmental loads and bridge design has been challenging, exciting and educational.

It is greatly appreciated that the thesis has been supported by the Norwegian Public Road administration. My contact person here has been Wang Jungao. I would like to thank my advisor Jasna Bogunovic Jakobsen for guidance and motivation. I would also like to thank Jonas Snæbjörnsson and Nicolo Daniotti for taking me on the bridge, and for helping me with coding in Matlab.

I would also like to take this opportunity to thank my friends, family and Eirik for their motivation, support and patience.

Stavanger, 14.06.2019

Kari Elise Nøstdahl Sørvåg

Abstract

After the opening of the cable-stayed bridge Stavanger City Bridge in 1978 there have been reports of vibrations of the stay cables. The bridge is 1066,6 m long, and has a main span of 185 m. The main span is supported by a pylon and 3 stay cable bundles on each side. The individual stay cables are interconnected by crossties to reduce vibrations.

Wind loads are known to induce various types of vibrations of structures. Flexible structural elements such as stay cables are especially prone to aerodynamic instabilities. A large amount of these vibrations is known to be rain-wind induced vibrations. This thesis will focus on the possibility of the vibrations at the Stavanger City Bridge being rain-wind induced vibrations.

The thesis has analysed the weather conditions at the time of observed vibrations, in order to evaluate the possibility of rain-wind induced vibrations at Stavanger City Bridge. There has also been an estimation of the number of hours the bridge may have been subjected to vibrations due to the combined action of rain and wind loads by analysing hourly weather data from eKlima.met.no.

The inherent parameters of the bridge are estimated based on six ten-minute periods of recorded accelerations at the bridge using MATLAB. The acceleration response of three cables and the bridge deck was analysed. Based on the recorded data an attempt to identify the first frequency mode of the cables and the bridge deck was performed by analysing the power spectral density. The damping ratio was estimated, and the identified frequencies were also compared to an estimation of frequencies of two of the stay cables. There was some difference in the estimated frequencies and the identified frequencies, most likely due to an oversimplification in the calculations of the estimated frequency.

The thesis found that for four of the five observed instances of vibrations it is reasonable to assume that vibrations could be rain-wind induced vibrations. The vibrations could also be due to other phenomena, e.g. wake effects from the pylon or the adjacent individual cables.

Table of Contents

1	Introduction	1
2	Cable-stayed bridges	4
2.1	Cable system.....	4
2.2	Design of cable stayed bridges	4
2.3	Stay cables.....	4
2.4	Pylon.....	5
2.5	Stiffening girder	5
3	Wind theory	6
3.1	Mean wind load	7
3.2	Reynolds number.....	8
3.3	Strouhal number	9
3.4	Scruton number	9
4	Dynamic response of cables.....	10
4.1	Parametric resonance.....	11
4.2	Anchorage excitation	11
4.3	Vortex-induced vibration.....	11
4.4	Buffeting.....	11
4.5	Wake effects.....	11
4.6	Galloping.....	12
4.7	Ice galloping	12
4.8	Rain-Wind Induced Vibration	12
4.8.1	Mechanisms of excitation	14
4.8.2	Instability mechanism	15
4.9	Mitigation of vibration.....	16
5	Case study: Bybrua in Stavanger.....	17
5.1	Stay cables.....	18
5.2	Measures to reduce vibrations	19
5.3	Weather conditions at Bybrua	21
5.4	Cable vibrations at Bybrua	23
5.5	Weather statistics.....	24
5.5.1	Estimated hours of vibration.....	24

5.5.2	Weibull distribution	25
5.6	Cable frequency.....	26
5.6.1	Estimation of vibration frequency based on video.....	26
5.7	Measuring vibrations	27
5.7.1	Accelerometer.....	27
5.7.2	Data acquisition	27
5.8	Signal processing.....	29
5.8.1	Spectral analysis	29
5.8.2	Nyquist frequency.....	29
5.9	Estimation of damping.....	30
6	Results and analysis.....	31
6.1	Weather conditions at Bybrua April 10 th , 2019.....	31
6.1.1	Axial, lateral and vertical accelerations of all nodes.....	32
6.1.2	Differences between stay cable 1 and stay cable 2	34
6.1.3	Combined vertical acceleration response for all nodes.....	35
6.1.4	Combined lateral acceleration response for all nodes.....	38
6.1.5	Frequency estimation	41
6.1.6	Cable frequencies from PSD-analysis	41
6.1.7	Damping estimation.....	46
6.2	Weather statistics.....	48
6.2.1	Wind rose.....	48
6.2.2	Weibull distribution of mean wind speed	49
6.2.3	Days with reported cable vibrations.....	50
6.2.4	Estimated hours of vibrations	52
7	Conclusion and further work.....	53
8	References.....	54
9	Appendix	56

Nomenclature

\bar{U}	Mean wind velocity
c	Scale parameter for Weibull distribution
C_D	Drag coefficient
C_L	Lift coefficient
C_M	Moment coefficient
D	Cable diameter
f	frequency
F_D	Drag force
F_L	Lift force
fps	Frames per second
k	Shape parameter for Weibull distribution
m	Cable mass per unit length
CDF	Cumulative density function
PDF	Probability density function
PSD	Power spectral density
RWIV	Rain-wind-induced vibration
VIV	Vortex induced vibration
WPD	Wind power density
α	Cable inclination
β	Wind yaw angle
ζ	Damping ratio
θ	Angle of rivulet on stay cable
ρ_a	Density of the air
σ	Standard deviations for turbulence components
ω_n	Natural frequency
δ	Logarithmic damping

List of figures

Figure 1.1 Flutter of Tacoma Narrows Bridge.....	1
Figure 1.2 Strömsund Bridge.....	2
Figure 2.1 Different cable arrangements.....	4
Figure 2.2 Cable cross sections from [4]	5
Figure 3.1 Dynamic excitation frequencies of structures by wind and earthquake, from [8].....	6
Figure 3.2 Wind direction.....	7
Figure 3.3 Reynolds number.....	8
Figure 4.1 Wake effects of pylon (left) and adjacent stay cables (right). From [10].	12
Figure 4.2 Meikonishi Bridge in Japan.....	13
Figure 4.3 Vibration amplitudes and weather conditions of a stay cable on Meikonishi Bridge. Figure from [5].....	14
Figure 4.4 Placement and formation of upper and lower rivulet. Figure from [5].	15
Figure 5.1 Overview of Bybrua. The bridge is marked in red. Map from [16].	17
Figure 5.2 Bybrua. From [18].	18
Figure 5.3 Stay cables of Bybrua.....	18
Figure 5.4 Overview of the cables of interest at Bybrua from the north side of the main span. Figure only for illustrational purposes, not to scale.....	19
Figure 5.5 Placement of crossties. From the Norwegian Public Road administration.	19
Figure 5.6 Cross ties of stay 1 (left) and stay 2 (right).....	20
Figure 5.7 Wind rose at Sola from 2008 to 2018 [23].....	21
Figure 5.8: Wind speeds at Sola over the last 10 years	22
Figure 5.9 Average monthly rainfall in Rogaland.....	22
Figure 5.10 Wind direction for possible RWIV at Bybrua.....	24
Figure 5.11 Snapshot from video	26
Figure 5.12 Node placement at the bridge. The red dots indicate node placement.....	28
Figure 6.1 Wind velocity recorded on 10/04/2019	31
Figure 6.2 Wind direction recorded on 10/04/2019.....	31
Figure 6.3 Wind rose on 10/04/2019 from 09:50-11:48. Sampling frequency 0,5 Hz. MATLAB code borrowed from [27].	32
Figure 6.4 Axial (x-direction), lateral (y-direction) and vertical (z-direction) accelerations of all four nodes during a ten-minute period.....	33
Figure 6.5 Acceleration of stay 1 and 2 in the vertical plane the 1st measurement.....	34

Figure 6.6 Acceleration of stay 1 and 2 in the vertical plane from the 6th measurement 35

Figure 6.7 Vertical acceleration of all nodes..... 37

Figure 6.8 Lateral acceleration of all nodes..... 40

Figure 6.9 Power Spectral Density of the “vertical” acceleration of cable 3, 5th dataset..... 41

Figure 6.10 Wind rose from Sola from 2005-2018. MATLAB code borrowed from [27]..... 48

Figure 6.11 Wind speeds and Weibull distribution..... 49

Figure 6.12 Visualization of possible wake effects at Bybrua 51

List of tables

Table 1 Observations of cable vibrations 23

Table 2 Frequency estimation in stay no. 1 and 2 from tension 41

Table 3 Identified frequencies of stay cable 1 from PSD..... 42

Table 4 Identified frequencies of stay cable 2 from PSD..... 43

Table 5 Difference between estimated frequencies and averaged identified frequencies from PSD-analysis of stay cable 1 44

Table 6 Difference between estimated frequencies and averaged identified frequencies from PSD-analysis of stay cable 2 44

Table 7 Identified frequencies from stay cable 3 from PSD-analysis..... 45

Table 8 Identified frequencies of bridge deck from PSD-analysis..... 46

Table 9 Estimated damping ratio..... 47

Table 10 Weather at the time of observed cable vibrations..... 50

Table 11 Is there a possibility of RWIV based on different criteria?..... 51

Table 12 Possible hours of RWIV from 2005-2018..... 52

Table 13 Estimated number of hours with possible RWIV for the whole lifetime of Bybrua 52

1 Introduction

Bridges are becoming slenderer, with longer and increasingly record-breaking spans. Longer spans and leaner stay cables leaves the bridge more vulnerable to excitation by wind loads. Wind loads can cause flutter of the bridge decks, most notably was the collapse of the suspension bridge Tacoma Narrows Bridge in 1940. The bridge deck collapsed as a result of flutter of the deck exposed to wind speeds around 19 m/s, as seen in Figure 1.1 [1]. Following the collapse, the aerodynamic instability of cable supported bridges was put on the agenda and caused a rapid rise in the research of wind-induced loads and its effects.

Cable supported bridges can be divided into suspension bridges and cable-stayed bridges. Cable-stayed bridges were first built in the seventeenth century, but it was not until the middle of the twentieth century they gained popularity. The earliest bridges were unsafe and flexible, favouring the more structurally stable suspension bridges. As the calculation techniques and construction materials improved in the twentieth century the modern cable-stayed bridges gained higher stability and stiffness due to pre-stressed cables with higher strength.

Strömsund Bridge (Figure 1.2) in Sweden was built in 1956 and marked the first of the modern cable-stayed bridges. After this the cable-stayed bridges increased in popularity, leading to more experimental designs with longer spans and augmented height. Cable-stayed bridges are now widely used in bridge designs, and worldwide there are now over 1000 cable-stayed bridges[2].



Figure 1.1 Flutter of Tacoma Narrows Bridge



Figure 1.2 Strömsund Bridge

Looking at the evolution of cable-stayed bridges, the first bridges were built with few stay cables, with large amounts of tension in each stay. This left the cable-stayed bridges more susceptible to vibrations due to wind loads [3]. Many individual stays shorter distances apart later became the norm, a result of their ease of structural detailing and construction [4].

While there has been a surge in the research of aerodynamic instability of cable-stayed bridges, some phenomena are still left to be fully understood. Among these is rain-wind induced vibration (RWIV), which was first reported and studied in detail in 1988 [5]. Although the mechanisms of the vibrations are largely understood today, some of the instability mechanisms are yet to be established. Understanding the dynamic between wind loads and cable structures is essential for keeping a bridge safe and in operation.

Large vibrations of the stay cables can lead to fatigue fractures of the cables and excessive stresses at the anchorage of the bridge, ultimately limiting the life span of the bridge. It is therefore necessary to understand the subject to be able to put appropriate measures into place to reduce the vibrations [1]. Rain-wind induced vibrations could therefore potentially be very damaging. As the name suggests, rain-wind induced vibrations are vibrations caused by the presence of rain combined with wind loads. The west coast of Norway, where Stavanger is placed, is known as windy and rainy, and it is reasonable to assume that vibrations of this kind could be present here. The thesis will focus on Stavanger City Bridge, known in Norwegian as Bybrua in, which was the first cable-stayed bridge in Norway, and the longest bridge in Rogaland when built.

Aim of thesis

The subject of this thesis was proposed by the Norwegian Public Roads Administration. The thesis will include an overview of the current research of cable vibrations of cable-stayed bridges. Of special interest is rain-wind induced vibrations, which have been reported to produce large amplitudes. It is followed by an analysis of the cable-stayed bridge Stavanger City Bridge, throughout the rest of the thesis called

Bybrua, where there have been reports of vibrations. The reported vibrations could be rain-wind induced vibrations.

The thesis will attempt to identify inherent parameters of the bridge. This includes an assessment of the accelerations, the natural frequency and the damping ratio of the cables and the bridge deck. This will be done by examining and analysing data collected from an accelerometer and a weather station mounted on Bybrua.

Furthermore, the weather conditions on Bybrua at the time of reported vibrations will be analysed in order to determine whether the observed vibrations could be rain-wind induced vibrations. Based on weather data from the portal eKlima.no, records of wind speed, wind direction and rainfall will be used to estimate how many hours the bridge may have been subjected to RWIV.

2 Cable-stayed bridges

Cable-stayed bridges consist of four main elements; stiffening girder/deck, cable system, pylon/tower and anchor block. The cable system connects the stiffening girder to the pylons. The anchor cable connects the end support to the pylon top and plays a dominant role in the structure [6].

2.1 Cable system

The cable system can be arranged in several ways, as depicted in Figure 2.1 [6].

- a) Pure fan, in which anchoring points of all cables are at the pylon top
- b) Harp, of which cables are arranged in parallel, and anchoring points are arranged in a downwards fashion along the pylon ensuring parallel arrangement of the stays.
- c) Modified/intermediate fan system, a composite of pure fan and harp arrangement.

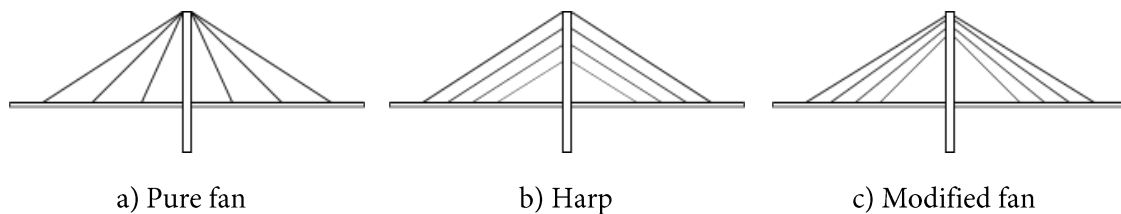


Figure 2.1 Different cable arrangements

The design of the cable system and pylons can be made with both symmetrical or asymmetrical spans, and there is also the possibility of multi-spans. Asymmetric designs typically occur when there are two spans with one pylon. The earliest modern cable-stayed bridges usually had larger spacing between the stays, which required a stiffer deck, typically steel decks [7].

2.2 Design of cable stayed bridges

The popularity of cable-stayed bridges comes down to the reduction in bending moments in the bridge deck, combined with greater spans. The moments are reduced by the transfer of loads through the stay cables to the pylons, and thus minimizing the moments from permanent loads. In addition to this, the construction process is less challenging as the force flow during construction is virtually unchanged after completion [4].

2.3 Stay cables

There are several types of cables used for cable-stayed bridges. While there have been some bridges constructed with concrete stays, steel cables are by far the most used. Most common are the helical bridge strands (spiral strands), locked-coil strands/ropes, parallel wire cables and parallel strand cables [4, 6]. The latter three are presented in Figure 2.2.

Locked-coil ropes

Locked-coil ropes were used in all the earliest cable-stayed bridges in Germany. They consist of layers of internal round wires and outer layers of z-shaped wires. Diameter of the internal wires are typically 5 mm, and the diameter z-shaped wires are 6-7 mm. The z-shaped outer layers ensure a compact cross

section with a small air ratio, as well as a tight surface of the stay. The diameter of the cable ranges from 40-180 mm, where the smallest sized cables (up to 80 mm) are used for cables consisting of several strands [6].

Parallel wire

Parallel wire cables are straight wire cables, surrounded by a polyethylene (PE) cover. The wires are shop fabricated and transported to the construction site on reels. The cables are typically made with 7 mm wires, with number of wires ranging from seven to up to 400 [4, 6].

Parallel strand

Parallel strand cables consist of seven wire strands as tension elements inside a PE cover. These are different from wire cables as they are made on site and stressed individually [4].

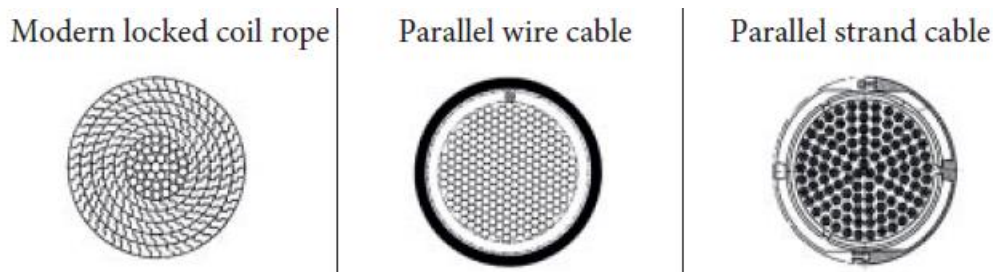


Figure 2.2 Cable cross sections from [4]

2.4 Pylon

Although pylons can be constructed in steel, pylons are usually constructed in concrete, as its loading is in compression and concrete proves the most cost-effective option. For bridges with two outer cable planes A-shaped pylons, H-shaped pylons and diamond-shaped pylons are the most common. Generally, A-shaped pylons consist of two inclined legs, joining at the top, whereas H-shaped pylons have two vertical or slightly inclined legs, either free standing or connected horizontally at the top. The bridge can also have just one central cable plane. Foot bridges often have more experimental designs, and can include inclined pylons [4].

2.5 Stiffening girder

The stiffening girder is subjected to most of the applied external load and must therefore locally be able to transfer the horizontal cable components by axial compression or tension. Included in the stiffening girder is the bridge deck, which provides strength and stiffness. Concrete and steel are the most common materials for the deck. There are also composite decks, where steel and concrete are used. Steel decks and concrete decks basically act in the same way. While concrete is generally cheaper than steel, concrete provides a higher dead load than steel, thus needing increased cross-sections of piers and pylons. Open cross-sections and box girders are used with both steel and concrete bridge decks. Separate beams are mainly used for steel structures, and solid cross-sections are used for concrete cross-sections[4, 6].

3 Wind theory

Suspension bridges and cable stayed bridges are especially exposed to the effects of wind loads due to their slender structure and low natural frequency. The wind velocity field is turbulent and fluctuating. Unlike the frequencies from other natural phenomena, such as earthquakes, wind exhibit low excitation frequencies, which can cause resonance in structures such as bridges, as depicted in Figure 3.1. [2, 8].

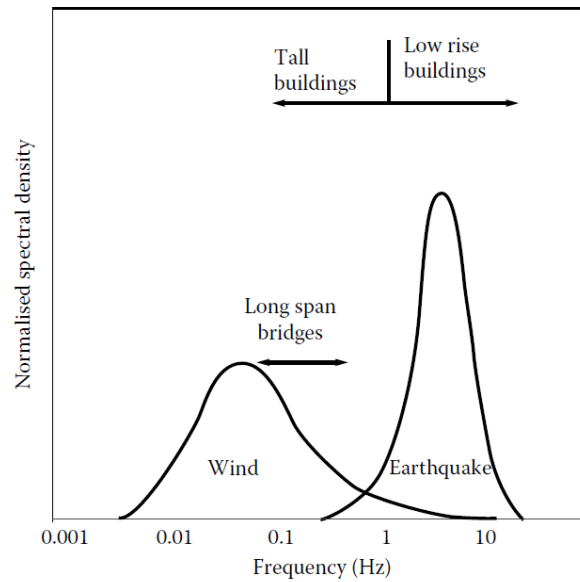


Figure 3.1 Dynamic excitation frequencies of structures by wind and earthquake, from [8].

The wind field can be characterised by the following three velocity components:

$$\bar{U}(z) + u(x, y, z, t) \tag{3.1}$$

$$v(x, y, z, t) \tag{3.2}$$

$$w(x, y, z, t) \tag{3.3}$$

As shown in Figure 3.2, \bar{U} is the mean wind velocity in the mean wind direction, often referred to as the static component of the wind. The u , v and w are fluctuating components, also called turbulence components in the x -, y - and z -directions respectively [2]. The mean wind speed at a height z above the ground can be calculated from [1].

$$\bar{U}(z) = \frac{1}{T} \int_0^T U(x, y, z, t) dt \tag{3.4}$$

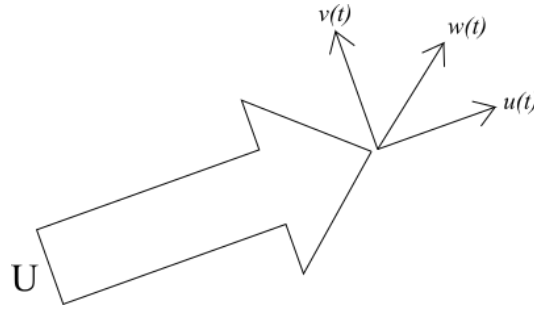


Figure 3.2 Wind direction

To measure the mean wind speed, a ten-minute average or hourly average is most common. The wind profile for the mean wind speed represents the wind. There are several mean wind speed profiles. Most common are the “logarithmic law” and the “power law”. Generally, the wind speed increases with height, and turbulence increases due to unevenness of the terrain and decreases with height.

The turbulence components are considered random stationary processes, and the mean value of these components is zero. Turbulence is measured by its standard deviation

$$\sigma_{u,v,w} = \sqrt{\frac{1}{T} \int_0^T u, v, w(t)^2 dt} \quad 3.5$$

The intensity of the turbulence is then calculated by dividing the standard deviation by the mean wind speed

$$I_{u,v,w} = \frac{\sigma_{u,v,w}}{\bar{U}} \quad 3.6$$

These components cause time-varying surface pressures to form when a body is present in the flow.

3.1 Mean wind load

Three components make up the mean wind load in a 2D analysis. These are the drag force, F_D , the lift force, F_L , and the moment M . For a circular cylinder with diameter D they are

$$F_D = \frac{1}{2} \rho_a U^2 D C_D \quad 3.7$$

$$F_L = \frac{1}{2} \rho_a U^2 D C_L \quad 3.8$$

$$M = \frac{1}{2} \rho_a U^2 D C_M \quad 3.9$$

The shape coefficients C_D , C_L and C_M depend on the surface of the body and the Reynolds number described in section 3.2 [2].

The drag force acts along the mean wind direction and the lift force acts perpendicular to the mean wind direction. The moment acts at the centroid of the structure and is equal to the resultant wind

force times the distance from the centroid [1, 8]. Wind analysis are often based on the quasi-steady assumption, where it is assumed that the present aerodynamic forces only impact on the immediate location of the considered body [9].

3.2 Reynolds number

Reynolds number is a dimensionless parameter defined as the ratio of the wind forces and the viscous forces acting on a body. For a cylinder the Reynolds number is defined as

$$Re = \frac{UD}{\nu} \quad 3.10$$

U = mean wind velocity

D = Diameter of cylinder

ν = kinematic viscosity of air

The movement of the flow around a cylinder of the same diameter is depicted in Figure 3.3. As the flow increases, the Reynolds number increases. Symmetrical vortices form at $Re \approx 20$, and as it increases to $Re \approx 30$, the vortices break off into separate vortices forming a vortex trail. This is known as the *Von Karman vortex trail*. The flow is laminar. As the Reynolds number exceeds about 5000, the wake widens and becomes turbulent, while the flow around stays laminar. Above $Re \approx 200\,000$ less forces act on the body and the wake narrows as a result [1, 2].

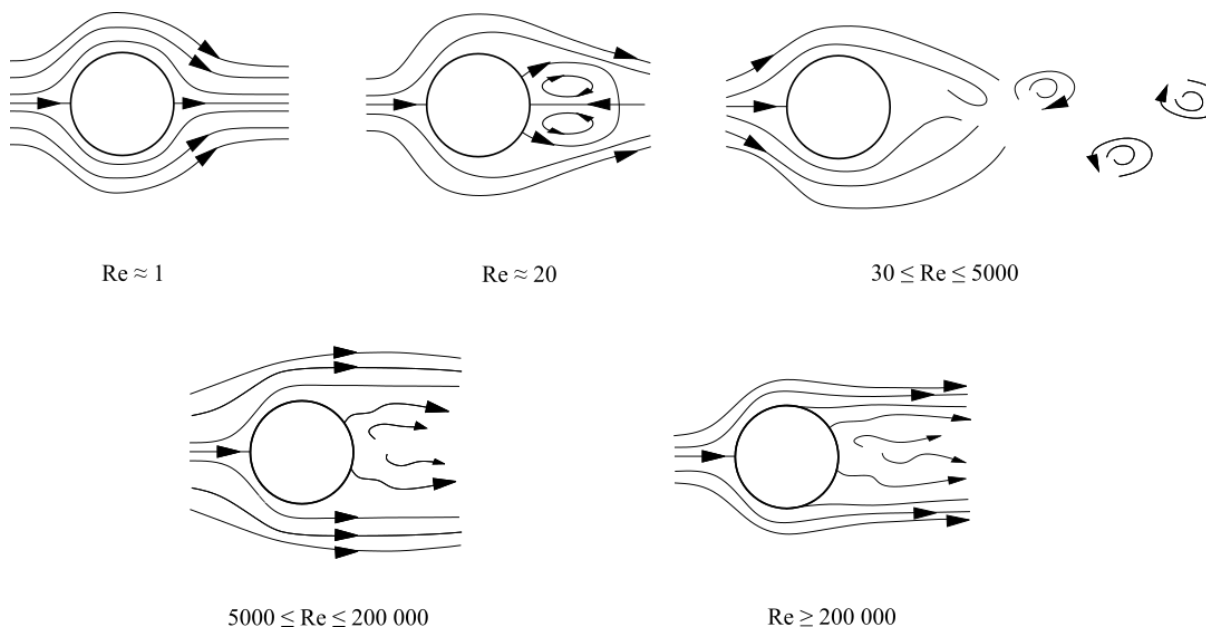


Figure 3.3 Reynolds number.

Flow past a circular cylinder at varying Reynolds numbers. From [2].

There are three ranges of Reynolds numbers that are of importance regarding vortex shedding. These ranges are referred to as *sub-critical* ($30 \leq Re \leq 200\,000$), *super-critical* ($200\,000 \leq Re \leq 4\,000\,000$) and *hyper-critical* ($Re \geq 4\,000\,000$).

3.3 Strouhal number

The Strouhal number is a relation between the vortex shedding frequency and the flow velocity. The Strouhal number is defined as

$$S_t = \frac{f_{st} D}{U} \quad 3.11$$

Where S_t is equal to the Strouhal number, U is the mean wind velocity, D is the stay diameter and f_{st} is the vortex shedding frequency. For a stay cable within the sub-critical range the Strouhal number is fixed at 0,18, increasing up to 0,30 for hyper-critical Reynolds numbers [6, 8]. By rearranging equation 3.11, the vortex shedding frequency can be expressed as

$$f_{st} = S_t \frac{U}{D} \quad 3.12$$

3.4 Scruton number

The Scruton number, S_c , is a non-dimensional number indicating the cable's susceptibility to vibration due to wind loads. The structural "mass-damping" parameter is defined as

$$S_c = \frac{\zeta m}{\rho_a D^2} \quad 3.13$$

Where ζ is the damping ratio, m is cable mass per unit length, D is cable diameter and ρ_a is the density of the air [3, 6].

4 Dynamic response of cables

Due to the turbulence of the wind flow, pressures and the resulting forces fluctuate around the body. As a stay cable is not fixed, the developed pressures result in vibrations, i.e. aeroelastic excitation of the stay.

Stay cables are characterised as very easily excited, as their inherent damping is extremely low, usually ranging from 0,010 to 0,012. In addition, the cables are long and slender with low mass. The single stay cable can be idealised as a taut string, with its stiffness arising from the longitudinal prestressing. Due to the variations in the cable tension, the cables' natural frequency varies, and thus the cable can have several resonant frequencies [4]. The natural frequency is found by the equation

$$\omega_n = \frac{n\pi}{L} \sqrt{\frac{T}{m}}, \quad n = 1, 2, \dots \quad 4.1$$

The frequency has the corresponding mode shapes

$$W_n(x) = A_n \sin \frac{n\pi x}{L}, \quad n = 1, 2, \dots \quad 4.2$$

The undamped free vibration of a taut string is

$$w(x, t) = \sum_{i=1}^n A_n \sin \left(\frac{n\pi x}{L} \right) \sin \left(\frac{n\pi}{L} \sqrt{\frac{T}{m}} t \right) \quad 4.3$$

Due to the uncoupled nature of the vibration modes, each mode can be treated as a single-degree-of-freedom oscillation [1].

Following equation 4.1, the frequency can be found by [2]

$$f_n = \frac{n}{2L} \sqrt{\frac{T}{m}}, \quad n = 1, 2, \dots \quad 4.4$$

Aerodynamic instability arises when small disturbances initiate unstable motions with increasing vibration amplitudes. This self-excitation occurs for flexible wind-sensitive structures such as stay cables as galloping and can also be seen on bridge girders in the form of flutter [2, 8].

Possible responses to the wind loads include buffeting, vortex-induced vibrations, galloping, wake galloping, ice galloping, rain-wind-induced vibration, wake effects, high speed vortex excitation and dry inclined cable galloping [3, 4]. In addition, vibrations can occur due to cable end movements caused by the loads on the bridge deck and the tower and excitation from adjacent structural members.

For inclined cables, such as stay cables, the main responses of concern are rain-wind induced vibration, high-speed vortex excitation and dry inclined cable galloping. The two latter phenomena are not very common. High-speed vortex excitation has been observed in the field during typhoons and wind tunnel testing, and dry inclined cable galloping has been seen even more rarely. Even though this type of vibration has not been observed frequently in full-scale bridge stay cables, the vibrations observed in

laboratory conditions have been of great amplitudes and of concern for bridge operation. Understanding this phenomenon is thought to be of importance, in order to be able to timely develop the appropriate countermeasures [9].

Flutter, as was the case for the Tacoma Narrows Bridge, is mainly of concern for bridge girders and other plate-like structures and will not be discussed further in this thesis.

4.1 Parametric resonance

Parametric resonance occurs on single cables and can produce large amplitudes, but they do not occur often after bridge construction. In stay cables parametric resonance arises due to rhythmic movements of adjacent structural members. If the exciting oscillation has a frequency double that of the natural frequency of the cable, resonance takes place. This is the fundamental and most significant case of resonance [4].

4.2 Anchorage excitation

This type of vibration, also denoted internal resonance or coupled vibrations, occurs only when cable frequencies equal the frequency of a heavy pylon or girder. Internal resonance seldom occurs, as the cable, pylon and deck frequencies are coupled, and the cable's natural frequencies are above that of the deck and pylon. The mass ratios of deck or pylon to cable must be 500:1 or larger for independent frequencies to appear, thus internal resonance is only a problem for bridges with very high girder or pylon masses. When this type of vibrations occurs, the oscillations are transferred from the structure to the cables [4, 6].

4.3 Vortex-induced vibration

Vortex-induced vibration (VIV) was for a long time thought to be the main cause for cable oscillations. VIV is a response to a wind velocity equivalent to a Reynolds number producing a vortex trail and occurs at relatively low wind speeds [1, 8].

As the frequency of the shedding and the cable's natural frequency coincide a phenomenon called *lock-in* causes the vibrations of the structure to contain the shedding frequency at resonance levels, within a range of wind velocities. This causes local oscillations with relatively small amplitudes to occur [4].

4.4 Buffeting

The vibration response from buffeting is due to the turbulent, fluctuating components of the wind in the along-wind, $u(t)$, and the across-wind direction, $v(t)$. The vibration amplitudes resulting from buffeting are notably smaller than those resulting from galloping. Due to the increased damping at high wind speeds, significant cable vibrations usually do not occur due to buffeting loads [2].

4.5 Wake effects

Wake effects is an umbrella term used to describe vibrations resulting from wakes generated by other cables or structural elements. The adjacent structural elements disturb the flow of the wind and cause

the local flow to fluctuate, which can trigger the cable vibration, as seen in Figure 4.1. The vibrations can be of the type buffeting, vortex resonance, interference effects and galloping [2].

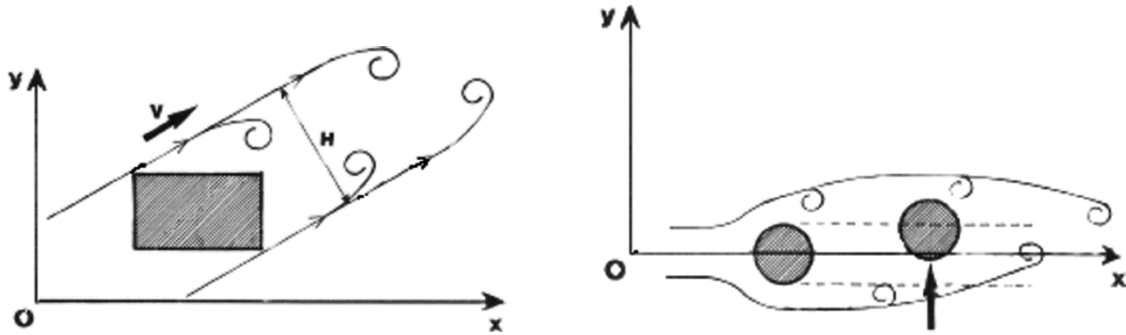


Figure 4.1 Wake effects of pylon (left) and adjacent stay cables (right). From [10].

4.6 Galloping

The term galloping refers to vibrations of larger amplitudes than those of vortex-induced vibrations and buffeting, occurring at lower frequencies. It is a single-degree-of-freedom type of aerodynamic instability which can arise for slender structures of non-circular cross-sections. The vibrations are translational in the across-flow direction and occur once a critical wind speed is reached. The criterion for instability is known as the Den-Hartog criterion, defined as

$$\left(\frac{dC_L}{d\beta} + C_D\right) < 0 \quad 4.5$$

The critical wind speed is defined as

$$U_{crit} = -\frac{4m\omega\zeta}{\rho D \left(\frac{C_L}{d\alpha} + C_D\right)} \quad 4.6$$

Where m is mass per unit length, ζ is the damping ratio and ω is the natural frequency of the body. This refers only to non-circular cross sections of body. Perfectly circular bodies such as stay cables should not experience vibrations due to instabilities such as galloping or flutter [1, 2].

4.7 Ice galloping

First observed on power lines and transmission cables, ice galloping is due to the build-up of ice around a cable, causing the cables' cross section to alter shape. This altered shape causes the aerodynamic force coefficients to change [4].

4.8 Rain-Wind Induced Vibration

Rain-wind induced vibrations (RWIV) of stay cables were first recorded by Hikami and Shiraishi [5] in 1988 during the construction of the Meikonishi Bridge in Japan (Figure 4.2). Vibrations on power lines had previously been observed during wind and rainfall and denoted *rain vibrations* [1, 2].



Figure 4.2 Meikonishi Bridge in Japan

Picture from <http://bridgeworld.net/asce-2008-bridges-calendar/>

This type of vibration generates oscillations of the cables, producing large amplitudes. The largest recorded amplitudes have been reported to be 2 m. The frequencies for which the vibrations have been observed range from 0,5-3 Hz. However, there have been reports of RWIV at up to 3,3 Hz [6]. This type of vibration is believed to be the cause for about 95% of reported vibrations in cable-stayed bridges.

Although there have been extensive research efforts after the first reported instances of rain-wind induced vibrations in the 1980s, the exact parameters and mechanisms of rain-wind induced vibrations are complex and still not completely understood. However it is known that rainfall combined with wind at a moderate wind speed from a specific direction must be present for the vibrations to start [3].

Hikami and Shiraishi [5] observed that the vibrating stay cables were declining in the direction of the wind and that the vibrations were only present during rainfall, as depicted in the bottom graph in Figure 4.3. Following their full-scale measurement of the bridge, they carried out wind-tunnel test to investigate the role of rain on the vibration. They hypothesized that the vibrations occurred due to the formation of rivulets on the cable surface. Subsequent research has confirmed the formation of an upper and lower rivulet to be of importance for the vibrations to start, perhaps due to their alteration of the cable cross-section [11].

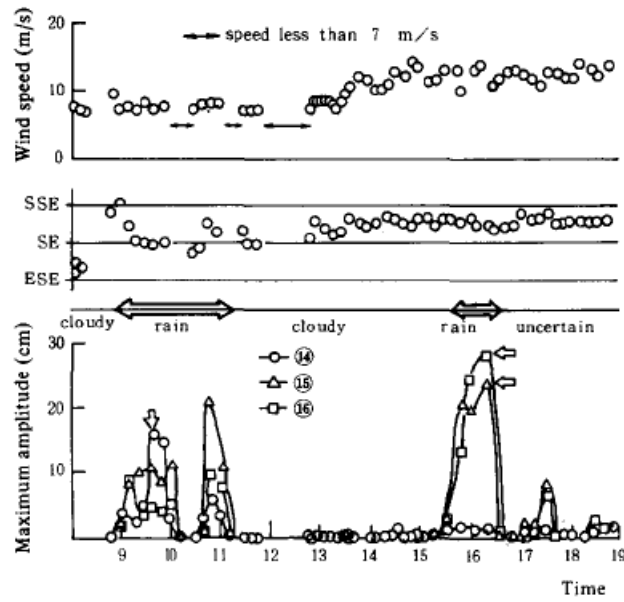


Figure 4.3 Vibration amplitudes and weather conditions of a stay cable on Meikonishi Bridge. Figure from [5].

4.8.1 Mechanisms of excitation

The majority of the research indicates that the formation of an upper and a lower rivulet initiates the vibration. At low wind speeds the rivulet on the underside of the cable takes its shape. As seen in Figure 4.4, the second upper rivulet forms as the wind speed increases [8]. The upper rivulet leads to a negative shift in the lift curve and a drag force reduction, which in turn causes a den Hartog instability of galloping [9]. Hikami and Shiraishi [5] also concluded that the role of the lower rivulet was that of a stabilizing one, with the upper rivulet providing the excitation force responsible for the aerodynamic instability. Together the rivulets act as trigger points for the separation of wind flow [8]. The cable vibration is further enhanced by the oscillation of the upper rivulet as the cable moves [10].

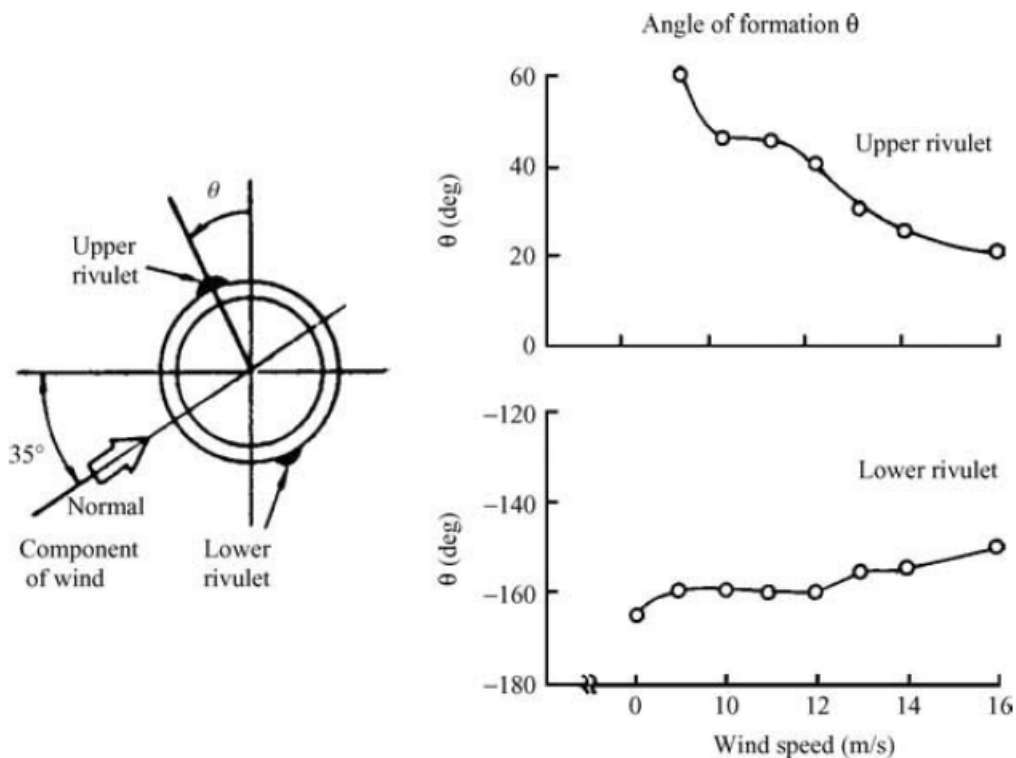


Figure 4.4 Placement and formation of upper and lower rivulet. Figure from [5].

Several important parameters are identified for the vibrations to start. These include rainfall, average wind speed, stay cable length and cross section, cable inclination, wind yaw angle (β) and damping.

Precipitation is needed for the vibrations to start, as it leads to the formation of the rivulets. However, the amount of rainfall does not need to be plentiful [10]. The cables need only be dampened from a drizzle to form rivulets [6]. Very heavy rain is thought to prevent the rivulet formation [1]. Smooth stay cables, such as cables with a polyethylene coating, painted or metal coated surfaces are observed to experience RWIV. The cross sections of stay cables with reported RWIV range from 80-200 mm, and have a cable inclination in the range 20-45°[2]. The wind yaw angle also plays a role, and vibrations increase as the wind approaches an orthogonal yaw angle.

RWIV do not require high wind speeds to commence. Vibrations are recorded for wind speeds ranging from 6 to 18 m/s, with the majority of observations found at wind speeds of 8-12 m/s [9]. At wind speeds above 20 m/s, the upper rivulet disappears as a result of the increased pressure pulling it away [12]. For wind speeds lower than 5 m/s, the amount of energy produced is considered insufficient to excite the stay cables[6].

4.8.2 Instability mechanism

RWIV was previously regarded as a classical type of galloping, but there has been debate as to whether the vibrations actually could be a different phenomenon of instability, or a combination of several instability mechanisms [2, 11]. These include galloping instabilities and high-speed vortex excitation[13].

An axial flow created in the wake of the cable could exacerbate the already established galloping of the cable caused by the presence and movement of the upper rivulet. The common vortex shedding described in section 4.3 could also act simultaneously causing an increase the vibrations. [2].

High-speed vortex excitation is a type of vortex-induced vibration discovered following the research efforts on rain-wind induced vibrations. First mentioned by Matsumoto, Shiraishi [14], they found that in addition to the von Karman vortex trail, an axial flow was generated along the cylinder. This axial flow acted as a splitter plate behind the cylinder. The interaction between the vortices across and along the cable can cause the cable vibrations [9]. The axial vortex shedding had a frequency $1/3$ that of the von Karman vortices. The vibration happens at a reduced velocity $U_R=U/fD=20, 40, 60\dots$, thus at higher velocities than that of classical vortex-induced vibration, which occur around $U_R=5$ [15]. This results in an augmented vortex for every 3rd vortex formed [2].

4.9 Mitigation of vibration

It is important to minimise cable vibrations as excessive oscillations increase the bending stresses near the anchorage. This can lead to both corrosion and fatigue. Increasing axial forces of the cable also leads to a higher bending moment, even if the amplitudes are not large [4]. In addition, people generally feel unsafe crossing bridges of palpable and visual vibration, as human bodies can detect very small vibrations [4].

To minimise cable vibrations several mitigation measures have been developed. Measures include increasing the damping of the structure, altering of the cross section to prevent the formation of an upper rivulet or structural alterations in the form of connecting the individual cables together.

Crossties or interconnecting ropes increase the cables' natural frequency to reduce the probability of resonance, as well as increasing the damping of the structure [2]. However, this method is not favoured, not only because it alters the aesthetic of the structure, but also because there have been cases of crossties breaking due to fatigue and their installation can hinder the easiness of inspection and surface repairs [6].

Aerodynamic measures generally work by altering the cross section of the cables. Helical fillets, dimpled or axially protuberated cable surfaces have shown to be effective [8].

Mechanical measures refer to different type of dampers. Examples of external dampers include oil dampers, hydraulic dampers and viscous friction dampers[9]. They are most often installed near the anchorage. There are also internal dampers, where a rubber ring is placed inside a chamber of oil around the cable near the anchorage. Rubber rings are also placed on the outside of stay cables near the anchorage to reduce bending stresses [2].

5 Case study: Bybrua in Stavanger

The planning of Bybrua (Stavanger City Bridge) started in 1972, and construction began in 1974. The bridge was opened to the public in December of 1978. The bridge connects the city of Stavanger to Buøy through Sølyst, stretching over Badedammen, Straumsteinsundet, Grasholmen and Grasholmsundet as shown in Figure 5.1 and Figure 5.2. Along with the smaller bridges across Engøysundet and Pyntesundet it is currently the only connection between the Hundvåg district and the mainland.



Figure 5.1 Overview of Bybrua. The bridge is marked in red. Map from [16].

There are several reasons as to why the bridge was built as a cable-stayed bridge. It was not the most economical alternative. But due to its placement in the city, aesthetics played a crucial part of the decision making, favouring a slender construction not to interfere with the landscape. In addition, one desired a bridge with no pillars in the canal, leaving it open for sea traffic [17].



Figure 5.2 Bybrua. From [18].

Bybrua was built as a free-cantilever bridge. The bridge is 1066,6 m in total length and has a width of 15.5 m, with three driving lanes and two pedestrian/bike lanes. It has one A-shaped pylon of two legs with 23 side spans and an asymmetric cable system. The pylon is a slender concrete construction, at 70 m, each leg 2.25 m wide. The main span is 185 m and consists of a single cell box girder in steel. The rest of the bridge is reinforced concrete [17]. Bybrua is today highly trafficated, with an annual average daily traffic (AADT) of 16250 [19]. A tunnel from Stavanger to Buøy is under construction and is set to open in 2019, relieving the bridge of some traffic. The bridge is proposed protected by the Norwegian Public Roads Administration [20].

5.1 Stay cables

The pylon has three stays on each side. The stay cables are of the type locked-coil ropes. The two outermost stays on each side (Stay number 1,2, 6 and 7) have 4 individual cables on each side, whereas the two innermost have two individual cables. The stay cables of interest in this thesis are presented in Figure 5.4. They are anchored at the edge of the bridge deck and the pylon allowing for replacement of the stays in the future if necessary.

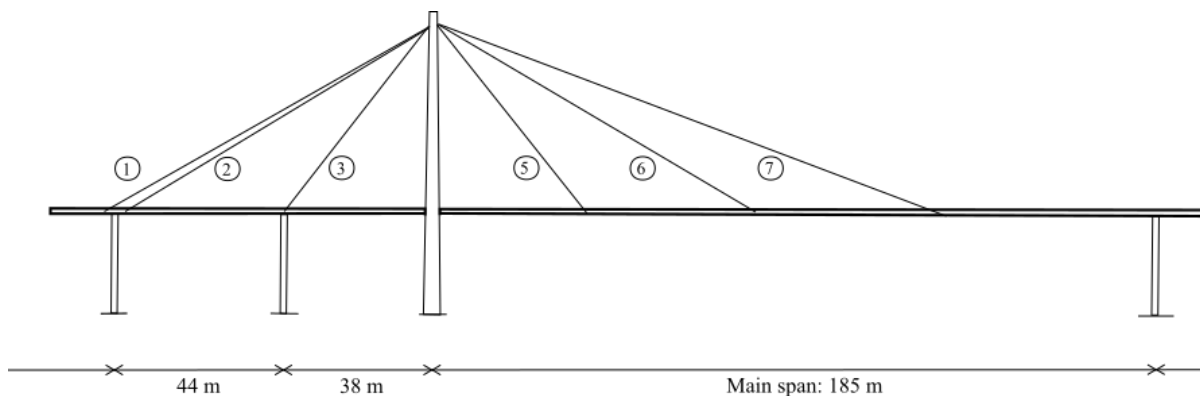


Figure 5.3 Stay cables of Bybrua

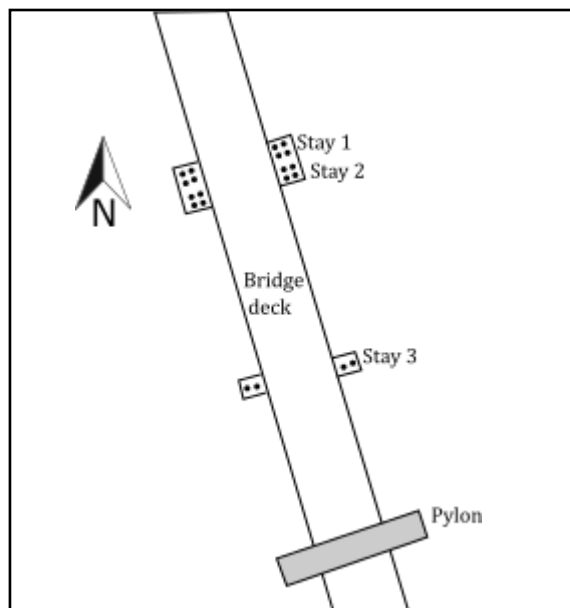


Figure 5.4 Overview of the cables of interest at Bybrua from the north side of the main span. Figure only for illustrational purposes, not to scale.

5.2 Measures to reduce vibrations

Due to the windy weather conditions on the site, a simplified full model of the bridge was built and tested at 1st and 2nd oscillation modes to understand the impact of the cable mass on the system. When adding weight to the cables, damping increased. High wind speeds were the main concern regarding aerodynamic instability and rubber dampers were installed to reduce oscillations and movements at the anchor heads. A several prototypes of the main span of the bridge deck were also tested in a wind tunnel to obtain the most aerodynamically stable bridge deck [21]. Additionally, there is installed cross-connections /crossies between the cables in each stay, to give the cables different frequencies and thus increase the damping of the stays [17]. The placement of the connections is depicted in Figure 5.5. The connection stay number 2 on the east side of the bridge is not properly connected as seen in Figure 5.6. This is one of the stays most prone to instability and RWIV. The stay cables have a metal coating.

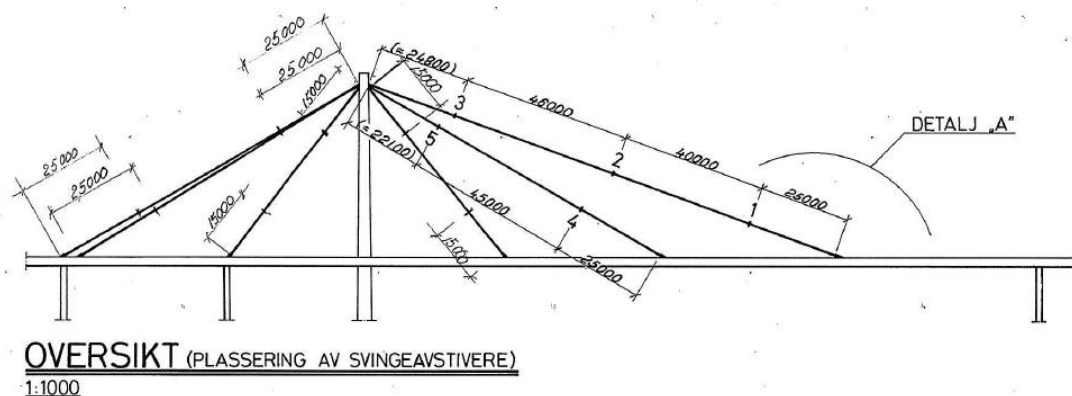


Figure 5.5 Placement of crossies. From the Norwegian Public Road administration.

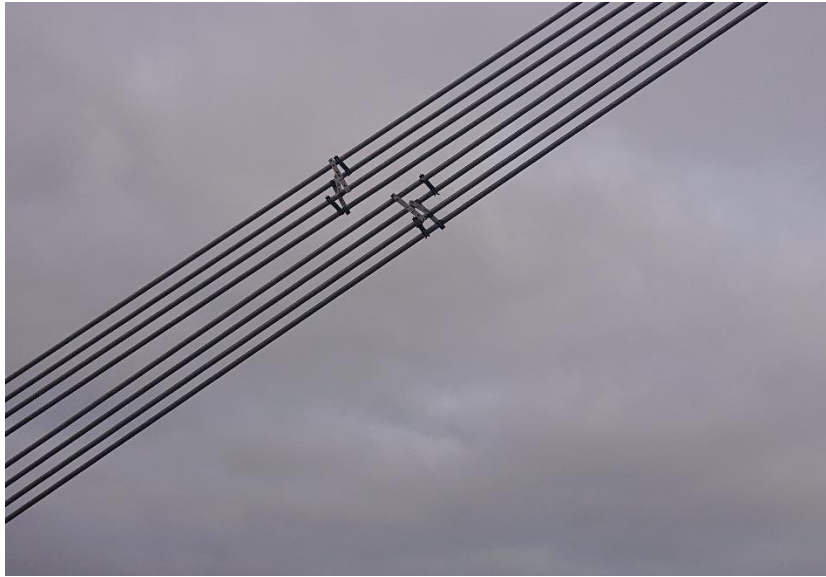


Figure 5.6 Cross ties of stay 1 (left) and stay 2 (right)

5.3 Weather conditions at Bybrua

The Norwegian climate varies within the country, with a wet and temperate coastline and drier climate in the inlands. Stavanger lies in the south west region of Norway along the coast. The Stavanger climate is classified as a temperate oceanic climate, with temperatures averaging between 0°C and 15°C [22]. As depicted in Figure 5.7, the main wind direction changes throughout the year. During winter months, from October to March, the wind usually comes from the south-east. During the remaining months, the main wind direction is the north-west. The wind speeds from the last 10 years are depicted in Figure 5.8. The average wind speed from the last 10 years is 4,6 m/s, with a median of 4,1 m/s. The west coast is known as rainy, and has an average rainfall of 1000-1200 mm.

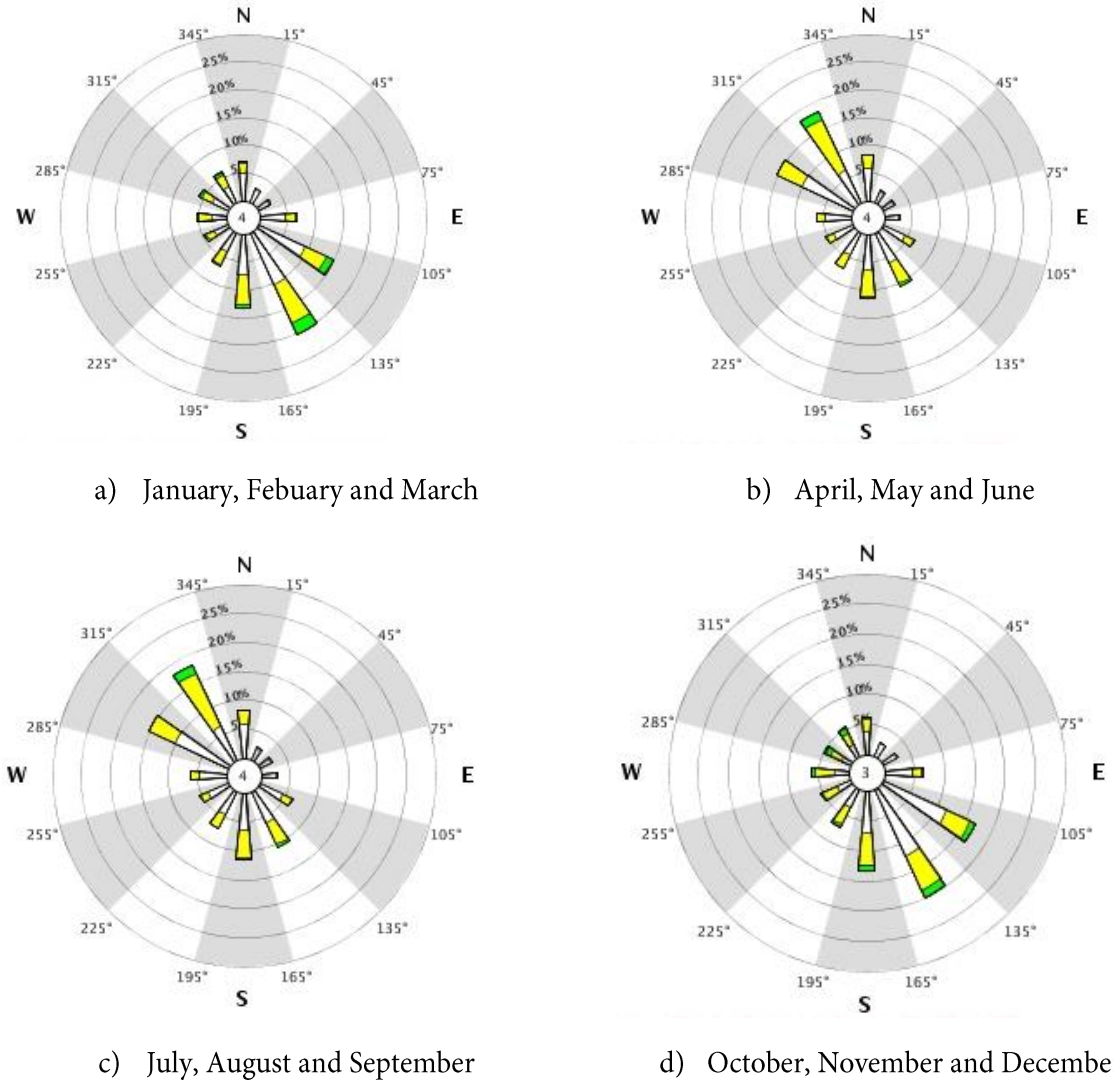


Figure 5.7 Wind rose at Sola from 2008 to 2018 [23].

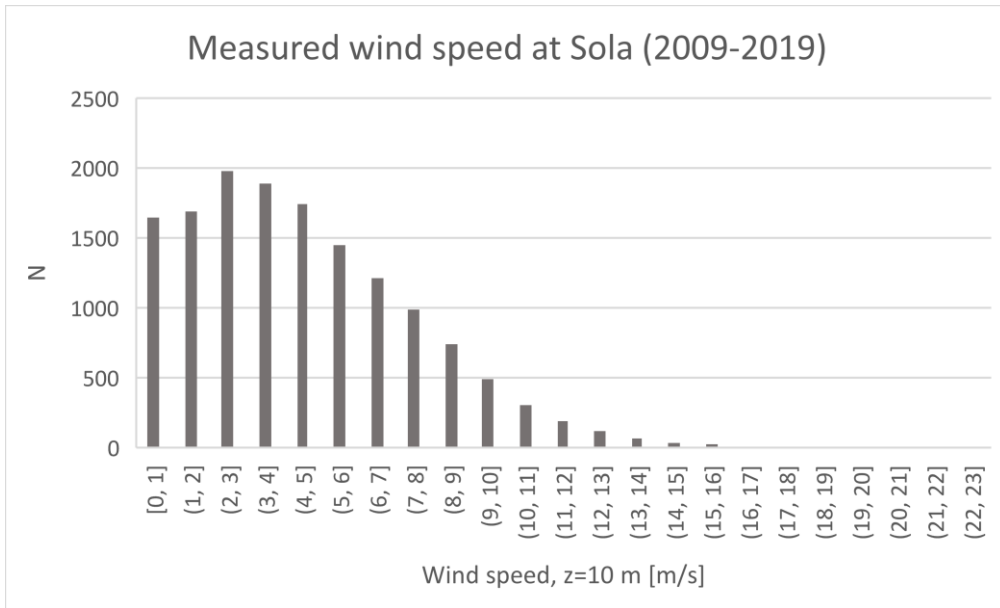


Figure 5.8: Wind speeds at Sola over the last 10 years
 Wind speeds (10m above the ground, 10 min mean) are measured four times each day (01:00, 07:00, 13:00 and 19:00) from 01.01.2009 to 31.12.2018. Data collected from eklima.no.

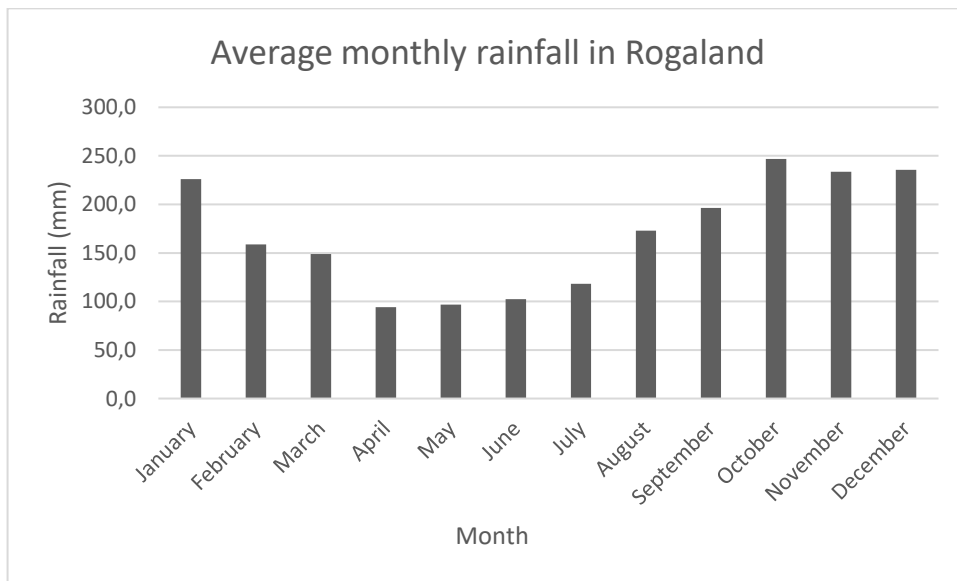


Figure 5.9 Average monthly rainfall in Rogaland

5.4 Cable vibrations at Bybrua

Vibrations of the stay cables at Bybrua have been observed on several occasions after the opening of the bridge. The time of the observations are listed in Table 1. According to the associated weather data, the vibrations seem to be rain-wind induced vibrations.

Table 1 Observations of cable vibrations

Observation	Date	Time
1	30.11.1999	13:15
2	06.09.2006	15:20
3	15.02.2014	10:35
4	01.11.2018	14:45
5	07.12.2018	14:40

5.5 Weather statistics

Cable vibrations on the bridge are reported by the public to the Norwegian Roads Administration. To analyse the weather conditions on the days of observed cable vibrations data from the portal eKlima.no and yr.no was used. Data from eKlima.no is provided by The Norwegian Meteorological Institute and is open to all and free of use. It consists of data from all weather stations in operation today, data from weather stations operated earlier and data others let eKlima distribute. Yr is a free weather service provided the Norwegian Meteorological Institute and the Norwegian Broadcasting Corporation (NRK). It contains detailed weather forecasts and is free of use.

Weather stations used for data collection:

The weather stations used to obtain data are Sola, Våland and Hundvåg. Sola is located farthest away, at 12 km from Bybrua, but this is the only weather station where wind speed and wind direction has been consistently recorded. Precipitation data from Våland, which is 2,3 km from the bridge, is used for all observations, except 2006, of which there was no recorded data. Here, data from Hundvåg (3,2 km from Bybrua) is examined.

5.5.1 Estimated hours of vibration

To estimate how many hours the cables of Bybrua might have experienced cable vibrations due to RWIV, hourly data from eKlima were analysed. Included data are the main parameters for RWIV, i.e. rainfall, wind speed and wind direction.

Reported cases of RWIV range from 5-20 m/s. However, the majority of the cases are reported at wind speeds at 8-12 m/s. Both cases are therefore used in the analysis. The bridge inclination is 162° as depicted in Figure 5.10. According to Caetano [2], the range of wind direction is $20-60^\circ$ to the longitudinal bridge axis. The range for RWIV at Bybrua is therefore taken to be $100-220^\circ$, i.e. the south/south-east direction.

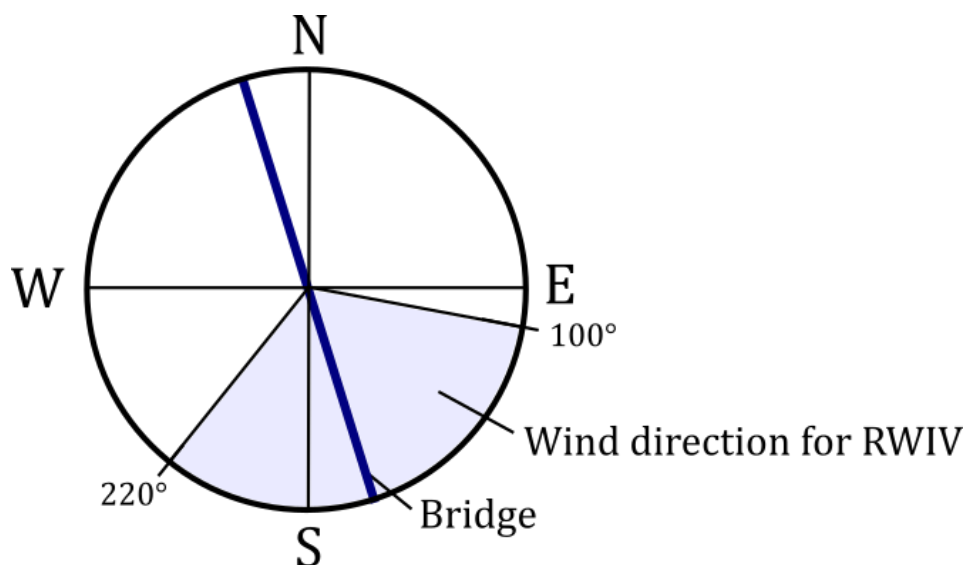


Figure 5.10 Wind direction for possible RWIV at Bybrua

Rainfall in most reported cases of RWIV is observed to be moderate, i.e. hourly rainfall exceeding 2.5 mm per hour, but there are also vibrations reported at lighter rain intensities. Therefore, the possibility of RWIV are checked for light rainfall both exceeding 0 mm/hour and 0,1 mm/hour and at moderate rainfall (>2,5 mm/hour).

5.5.2 Weibull distribution

Along with the Gaussian (normal) distribution and the Rayleigh distribution, the Weibull distribution is one of the most commonly used probability distributions in wind engineering [24]. The advantage of the Weibull distribution over the two former distribution forms mentioned, is that it has two parameters – a shape parameter and a scale parameter. The shape parameter, k , is dimensionless, whereas the scale parameter, c , has the same unit as the wind speed. The Weibull distribution is also better suited to describe the low to moderate wind speeds of which RWIV are a problem, but one limitation is that it does not take wind direction into account [1]. The cumulative distribution function (CDF) and the probability density function (PDF) defined as

$$p(x) = \frac{k}{c} \left(\frac{x}{c}\right)^{k-1} \exp\left(-\left(\frac{x}{c}\right)^k\right) \quad 5.1$$

$$p(> x) = \exp\left(-\left(\frac{x}{c}\right)^k\right) \quad 5.2$$

The hourly weather data from January 2005 to December 2018 from Sola is used to fit the wind speeds to a Weibull distribution. By matching the wind power density (WPD) of the existing data and with the WPD of a Weibull distribution, the shape parameter k was estimated using Excels solver function.

5.6 Cable frequency

Stay cables can be modelled as a taut string. The sag of the inclined cable due to its self-weight is not included in estimating the frequency of the cables but should be included for more exact calculations of cable frequency. For the purpose of this thesis, the frequency is estimated based on modelling the cable as a taut string with no sag.

As cable-stayed systems are indeterminate systems, an approximate calculation of the forces in the back stay of the cable system has been performed following Svensson [4]. Only dead loads, i.e. loads from self-weight, is included in the calculation, as they are larger than the live loads, and will give an approximate estimate of the cable forces. Due to the proximity of the 16 individual back stay cables, they will be regarded as one cable in the calculations.

5.6.1 Estimation of vibration frequency based on video

A very simple analysis of the video footage taken on 15/02/2014 at 10:28 was done to estimate the frequency of the vibrations. The video is shot in 29,97 fps. By examining each frame within one second, the time between the local minima and maxima of the vibrations was found and based on this the frequency was estimated.

The video shows that the four individual cables of stay cable one acting as one, i.e. none of the individual cables oscillate or vibrate on their own. For stay cable no. 2, where the crosstie is undone, larger oscillations and individual vibrations were visually observed.



Figure 5.11 Snapshot from video

The video was recorded on 15th of February 2014 and show vibrations of significant amplitudes of both cross tied stay cables.

5.7 Measuring vibrations

5.7.1 Accelerometer

To measure vibrations of a system, sensors such as accelerometers are used to identify changes. The basic principle of an accelerometer is to sense the pressures applied by a mass on an object when a force acts on it. From Newtons second law we have

$$F = ma = kx \quad 5.3$$

If a system has a given spring constant k , and mass m , the acceleration is a function of x : $a=x(t)$. Hence, a change in length x represents a change in the acceleration.

There are several different types of accelerometers. Mechanical accelerometers, e.g. seismometers have a lightweight outer casing with a heavier mass inside attached to a spring. To determine the force, the distance the spring stretches is measured. Capacitive accelerometers work in a similar manner, but instead of measuring force by the stretched length of the spring, they use electric or magnetic signals. In this way a force is measured by the change in capacitance. Piezoelectric accelerometers work by pressing the mass against a crystal. As the crystal is squeezed it generates a voltage to determine the force.

Technical progress in recent years have made micro-electrical-mechanical systems (MEMS) available for measuring vibrations. MEMS contain both mechanical and electrical components and measure changes in capacitance to determine the acceleration acting on the body. These complete vibration monitoring systems consist of accelerometers placed in wireless node(s) and a data acquisition station/transmitter to generate data accessible through cloud-based solutions [1].

For measuring the vibrations at Bybrua a wireless accelerometer node G-Link-200 will be used. This is a battery driven wireless triaxial MEMS accelerometer inside a weatherproof enclosure. The data acquisition station is WASDA 2000.

5.7.2 Data acquisition

Data from Bybrua was obtained on the 10th of April 2019. Four nodes were placed on the bridge. They were placed on the inner most stay cable of the cable bundle of stay 1, 2, 3 and the bridge deck as depicted in Figure 5.12. They were placed on the north side of the bridge as this is the place of observed vibrations. The accelerometers of the stays were placed about two meters above the bridge deck. There was no manual excitation of the cables, thus the measured accelerations reflect the normal usage of the bridge.

The gathered data was divided into six data sets of 10 minutes, which were used to locate the natural frequencies of the cables and the bridge deck. The response was measured in each local x-, y- and z-direction as shown in the diagram in

The weather at the location was measured with a Kestrel 5500 Weather Meter. The measurements included wind speed, wind direction, temperature.

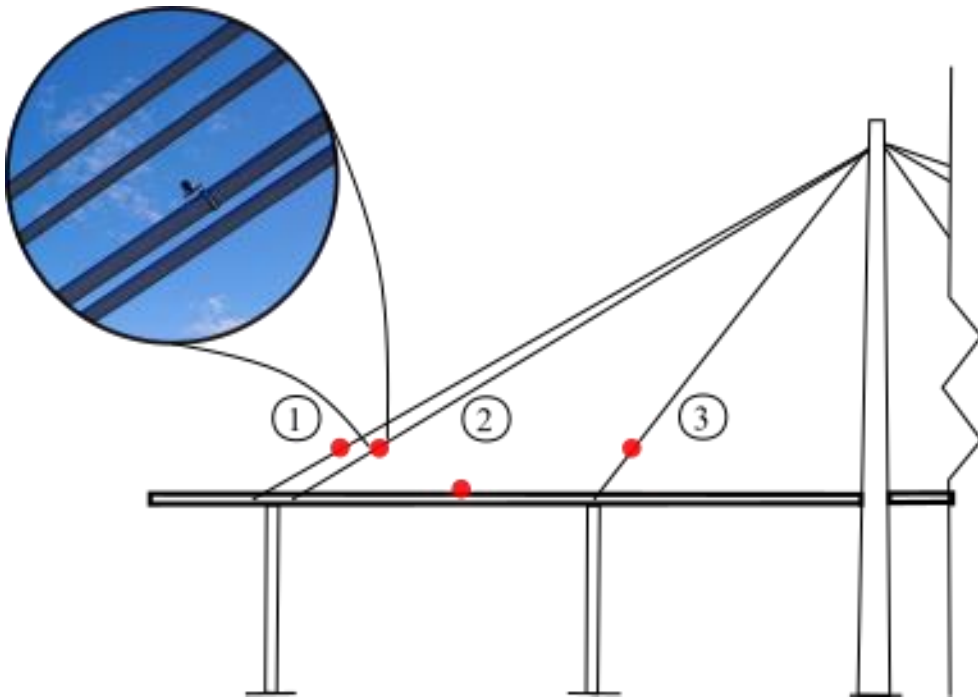


Figure 5.12 Node placement at the bridge. The red dots indicate node placement.

5.8 Signal processing

5.8.1 Spectral analysis

To analyse a random process, $x(t)$, such as vibrations due to wind is done by analysing the autocorrelation function $R(\tau)$, as it indirectly gives information on the frequencies in a random process [25]. The autocorrelation function of a random process is the mean value of the product $x(t)+x(\tau+t)$. It is defined as

$$R(t) = x^2 = \lim_{T \rightarrow \infty} \frac{1}{T} \int_0^T x(\tau)x(\tau + t)d\tau \quad 5.4$$

Rewriting equation 5.4 as a digital signal

$$R(n, \Delta t) = \frac{1}{N - n} \sum_{j=0}^{N-n} x_j x_{j+n} \quad 5.5$$

Here the number of samples is N , Δt is the interval of sampling and n is a parameter used to control the number of points used in the computation [26]. A random process will show the function $R(t)$ approaching zero as $T \rightarrow \infty$. The Fourier transform of the autocorrelation function is called the power spectral density (PSD). This spectrum, $S(\omega)$, of the random signal is defined as

$$S(\omega) = \frac{1}{2\pi} \int_{-\infty}^{\infty} R(\tau)e^{-i\omega\tau} d\tau \quad 5.6$$

Which in digital terms is equal to

$$S(\Delta\omega) = \frac{|x(\omega)|^2}{N\Delta t} \quad 5.7$$

The PSD gives a measure of the rate of which the signal turns within the frequency domain. For the digital signal, the magnitude of the Fast Fourier transform is represented by $|x(\omega)|^2$ [26]. From the PSD, the eigenfrequencies of the cables can be determined by peak picking of the spectrum in MATLAB.

5.8.2 Nyquist frequency

In spectral analysis, the Nyquist frequency, f_N , describes the highest frequency from the sampled data which can be defined. The frequency is defined by

$$f_N = \frac{1}{2\Delta} \quad 5.8$$

Where Δ is the time step of the sampling. Thus, frequencies above this cannot properly be described by spectral analysis [9].

5.9 Estimation of damping

One technique to estimate the damping in the cables is the Random Decrement Technique (RDT). Over time the random signals are inclined to average out and leave the free response of a signal to be interpreted [9]. The damping ratio using this technique can be found by the logarithmic decrement, δ :

$$\delta = \ln \frac{x_n}{x_{n+1}} = \frac{2\pi\zeta}{\sqrt{1-\zeta^2}} \quad 5.9$$

Where the successive amplitudes are given by x_n and x_{n+1} . For small damping ratio, one can assume

$$\zeta = \frac{\delta}{2\pi} \quad 5.10$$

A Butterworth bandpass filter is used to filter the acceleration response. By specifying either a low or high frequency or two bandpass or bandstop frequencies, the desired frequencies pass through the filter. The order of the filter determines the steepness of the cutoff curve. Appropriate filters are obtained using trial and error.

An alternative method to estimate the damping ratio is the “half-power bandwidth method”, as the width of the PSD is in proportion to the damping ratio of the system. In a PSD-analysis it is defined as

$$\zeta = \frac{f_2 - f_1}{2f_r} \quad 5.11$$

Where f_1 and f_2 refer to the half-peak readings, and f_r is the resonant frequency, i.e. the spectral peak. Although this method is not as reliable as the RDT, it gives a rough estimate of the damping ratio.[9].

6 Results and analysis

This chapter will present the results from the acquired data from Bybrua the 10/04/2019 and analysed data from eKlima. The data is analysed by using MATLAB and Excel.

6.1 Weather conditions at Bybrua April 10th, 2019

The wind speed recorded at the site from 09:50 to 11:48 on the day of data acquisition is shown in the graph in Figure 6.1, and the wind direction is depicted in Figure 6.2. The mean wind velocity of the recording period was 1,63 m/s, thus lower than the required wind speed for RWIV. There was no rainfall and the wind direction ranged from about 0 to 120°, as shown in the wind rose from the collected wind data depicted in Figure 6.3. The primary wind direction between 09:50 and 10:55 was 100°. This was also the period of the highest measured wind speeds. After 10:55 there was a shift in both the wind speed and wind direction, with a lower average wind speed and wind from the north/north east direction. At lower wind speeds the wind direction is also less stable.

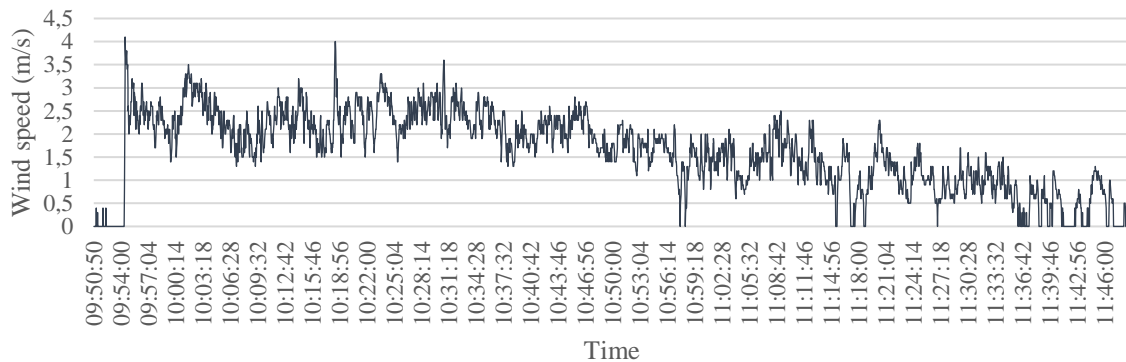


Figure 6.1 Wind velocity recorded on 10/04/2019

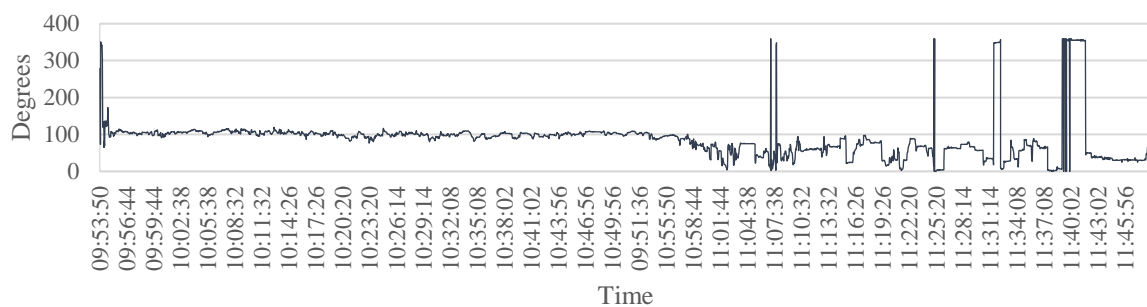


Figure 6.2 Wind direction recorded on 10/04/2019

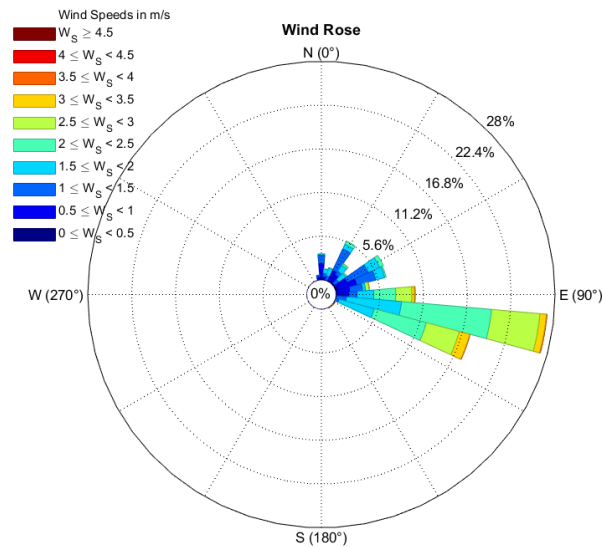


Figure 6.3 Wind rose on 10/04/2019 from 09:50-11:48. Sampling frequency 0,5 Hz. MATLAB code borrowed from [27].

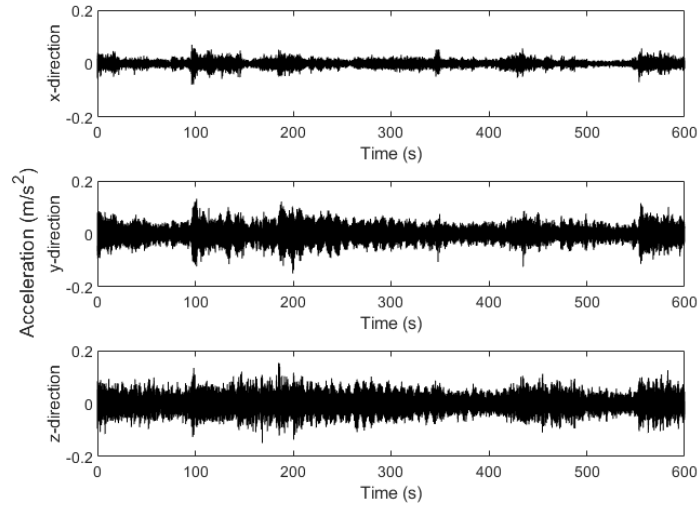
6.1.1 Axial, lateral and vertical accelerations of all nodes

The third ten-minute interval of sampling was chosen to compare the accelerations of all the four nodes in local axial, lateral and vertical directions as x, y and z, respectively. This data set was chosen as it was recorded during a time of variable wind speed and wind direction. For accelerometers installed on the cables, the z-direction is perpendicular to the cable axis, in the vertical plane.

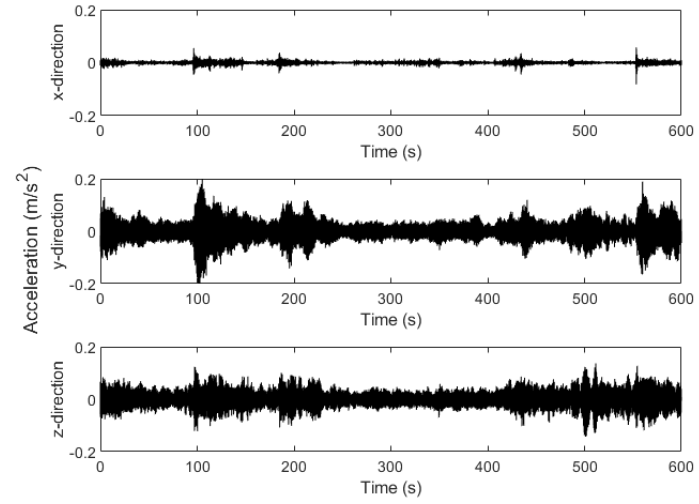
Stay cable 1 and stay cable 2 display larger accelerations in the y- and z-direction than stay cable 3. This is expected, as the third stay is shorter than the other two stays examined. Overall, the acceleration response of stay 2 is larger than that of the other nodes. This may be due to the broken crosstie holding the four individual cables together. Stay 1 is longer than stay 2 and its material properties and cross section is the same. Thus, theoretically stay 1 should exhibit greater vibrations than stay 2.

The acceleration of the cables is far greater than the accelerations at the railing of the bridge deck. The largest response seems to coincide with the short duration large response of the bridge deck. Acceleration peaks appear to decay faster at the bridge deck than at either of the stays. The excitation energy provided by the traffic in the bridge is transferred to and partly spent by the cables which are likely to have lower damping levels than the concrete bridge deck.

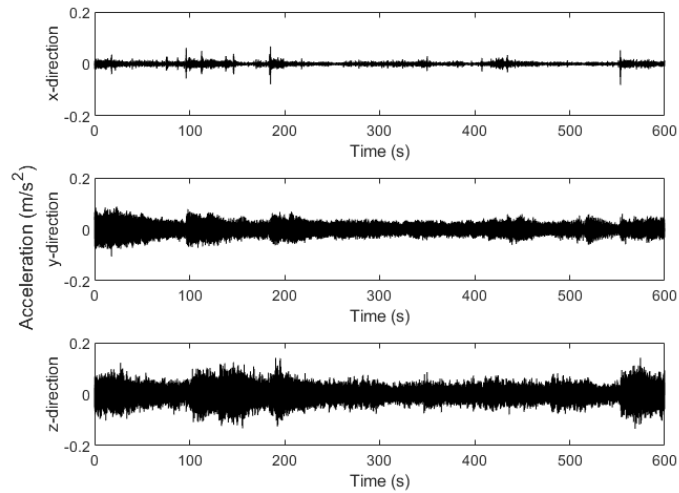
Stay cable 1



Stay cable 2



Stay cable 3



Bridge deck

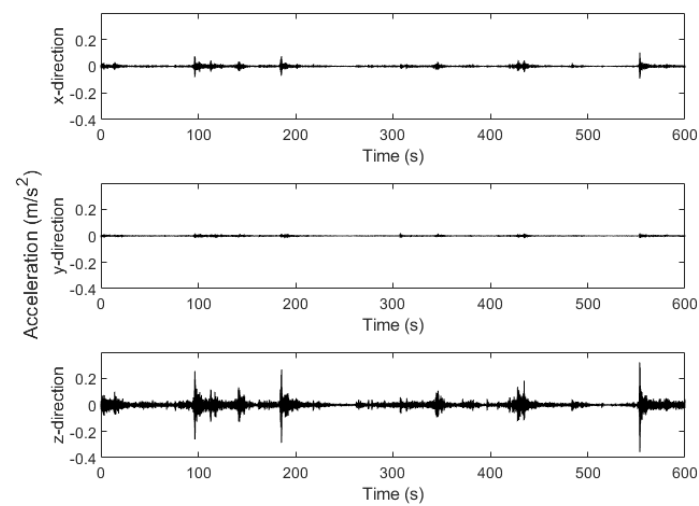


Figure 6.4 Axial (x-direction), lateral (y-direction) and vertical (z-direction) accelerations of all four nodes during a ten-minute period.

6.1.2 Differences between stay cable 1 and stay cable 2

Figure 6.5 shows the vertical raw acceleration of stay 1 and 2 from the first set of recorded data. The acceleration of stay 2 are somewhat larger than those of stay 1. This is also noticeable in Figure 6.6, which shows the acceleration of the last set of recorded data. This could possibly be due to the broken cross tie of stay 2. The difference in the amount of acceleration is also apparent. At the time of recording the first data set, the wind speed was considerably higher than the wind speed of the last data set. The largest accelerations of the last recorded set are therefore presumably due to traffic loads.

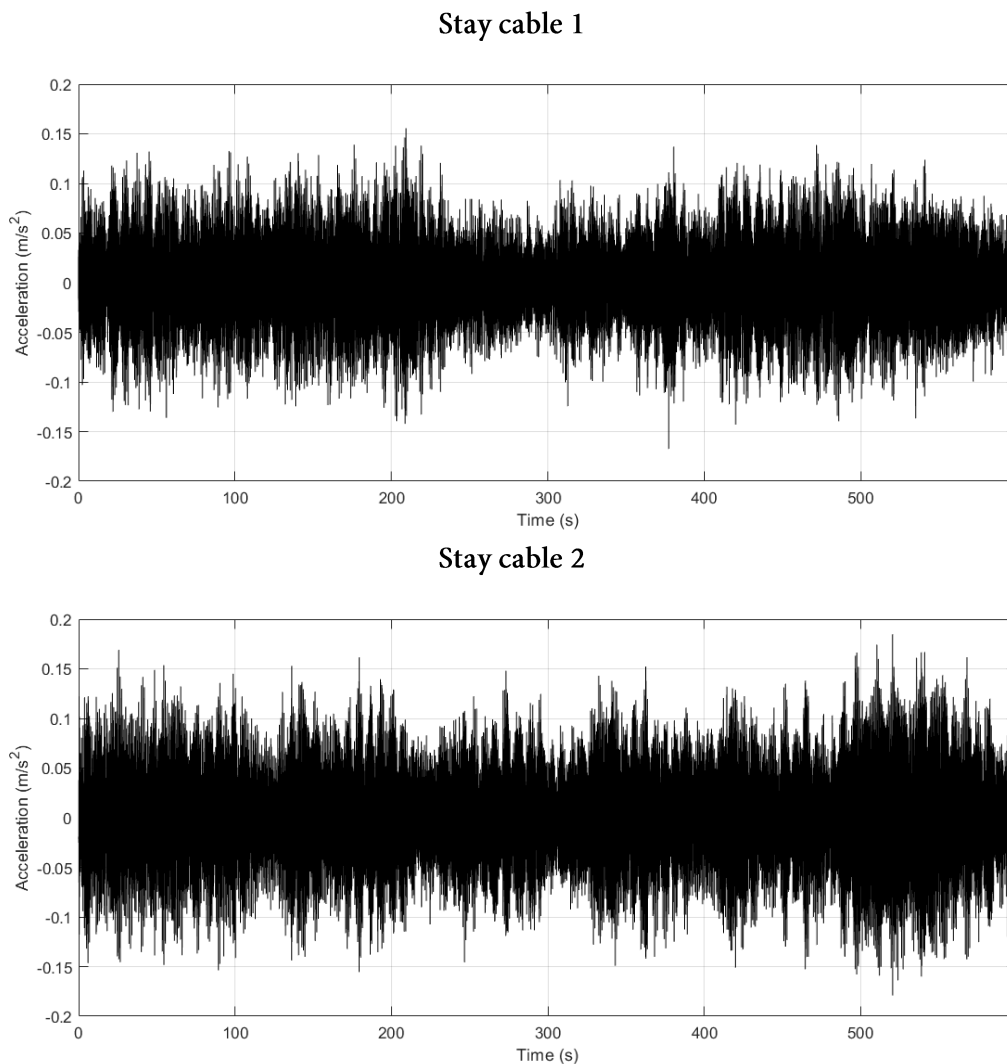
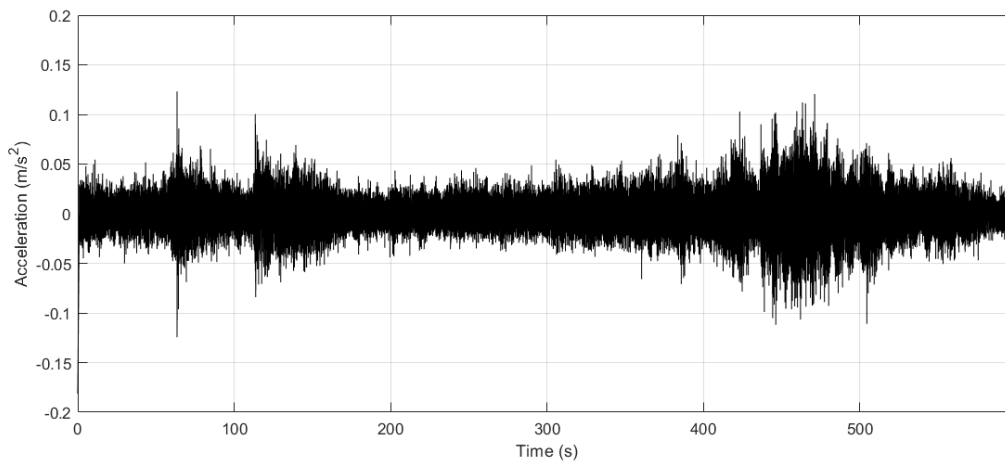


Figure 6.5 Acceleration of stay 1 and 2 in the vertical plane the 1st measurement

Stay cable 1



Stay cable 2

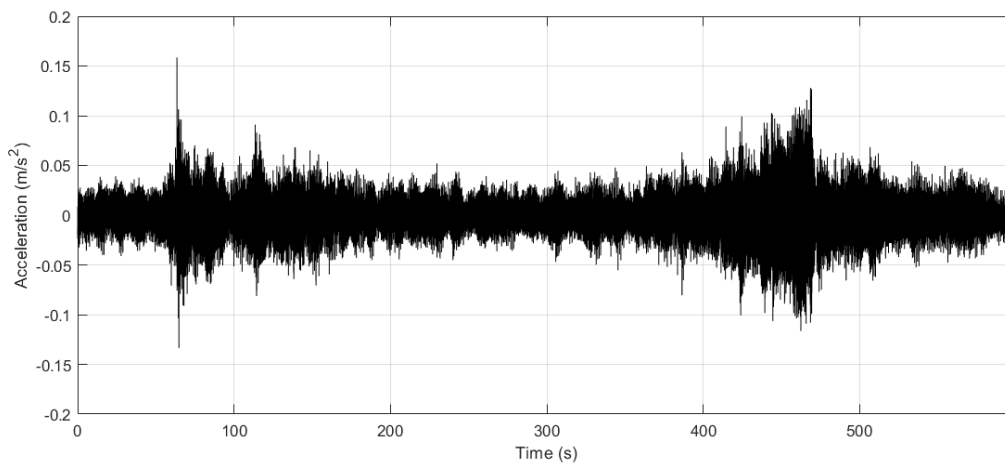


Figure 6.6 Acceleration of stay 1 and 2 in the vertical plane from the 6th measurement

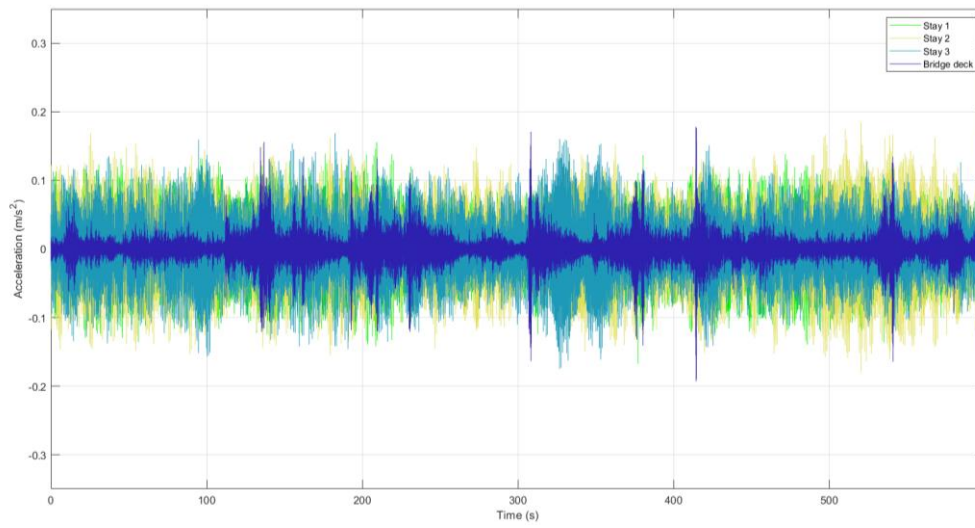
6.1.3 Combined vertical acceleration response for all nodes

Figure 6.7 shows the “vertical” acceleration response for all four nodes for all six periods. By visually examining the unfiltered vertical response graphs from all the six data sets, several observations can be made. The data sets indicate that the response of all the stay cables are greater in the first measurements, while the bridge deck response seem to be almost unchanged for all the data sets. This cause of this might be the declining wind speeds at the time of observation.

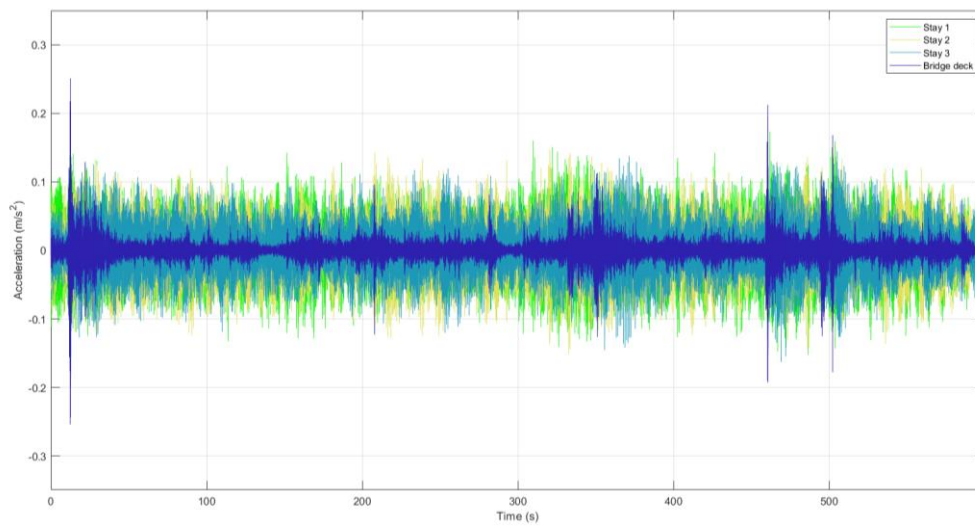
Particularly noticeable is the rapid decline of the accelerations at the bridge deck compared to the cables. Despite the peaks of the bridge deck being larger, the lower damping of the cables likely causes the intervals with the notable response to be longer.

The figure also presents the cables’ response to excitation of the bridge deck, likely due to heavy vehicles passing the location of the accelerometer. The response is most clearly seen in Figure 6.7 d) and e). The response is most noticeable for stay 3. It is reasonable to assume that this is due to its proximity to the accelerometer of the bridge deck.

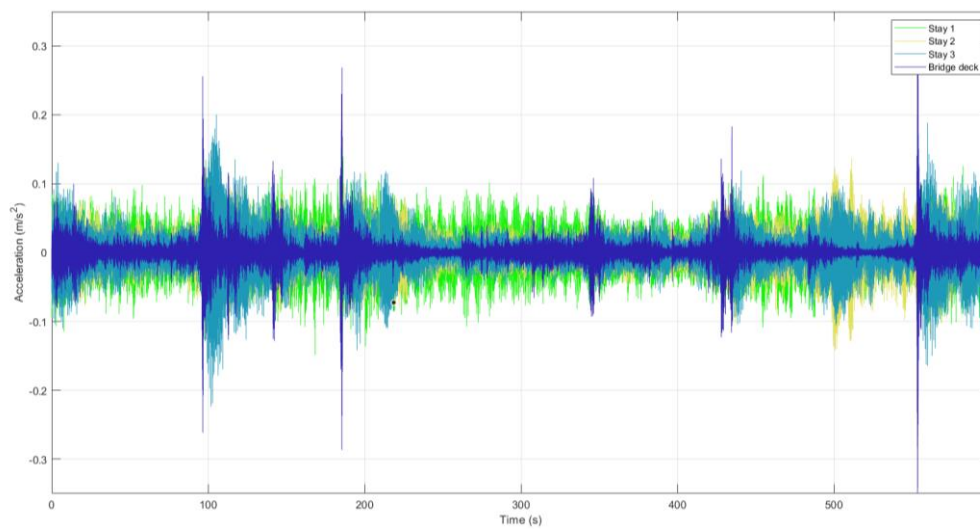
a) 1st dataset



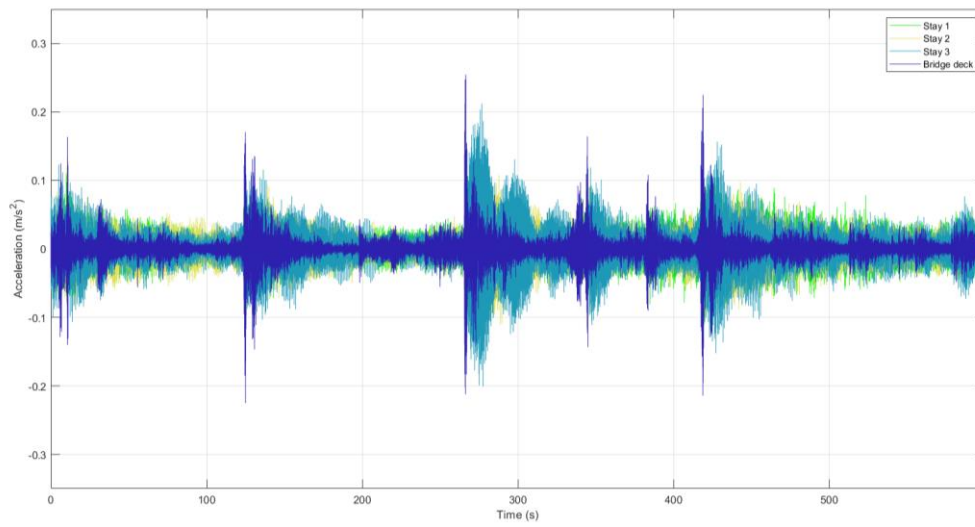
b) 2nd dataset



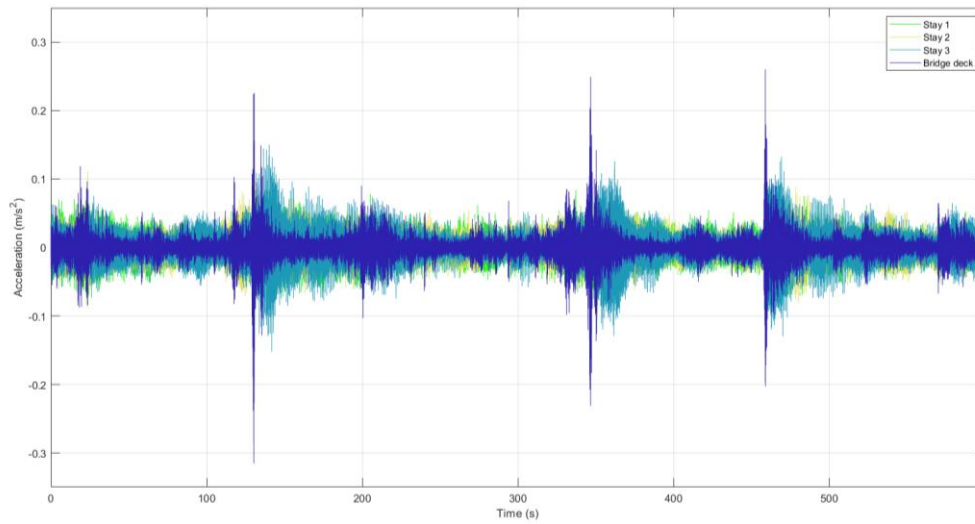
c) 3rd dataset



d) 4th dataset



e) 5th dataset



f) 6th dataset

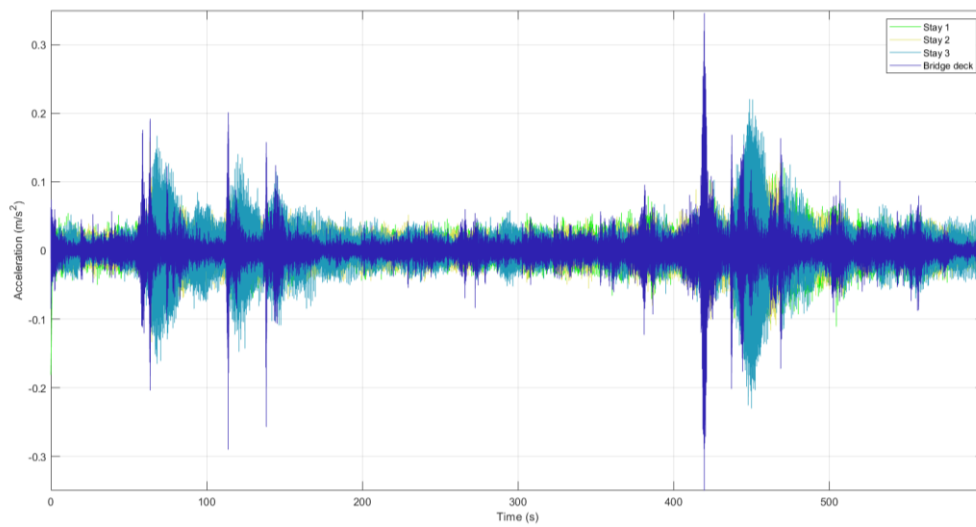


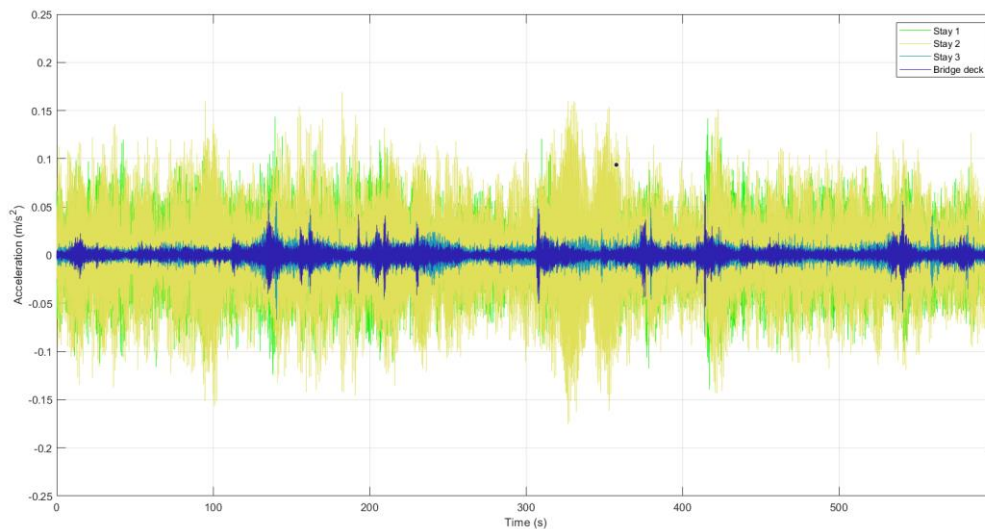
Figure 6.7 Vertical acceleration of all nodes

6.1.4 Combined lateral acceleration response for all nodes

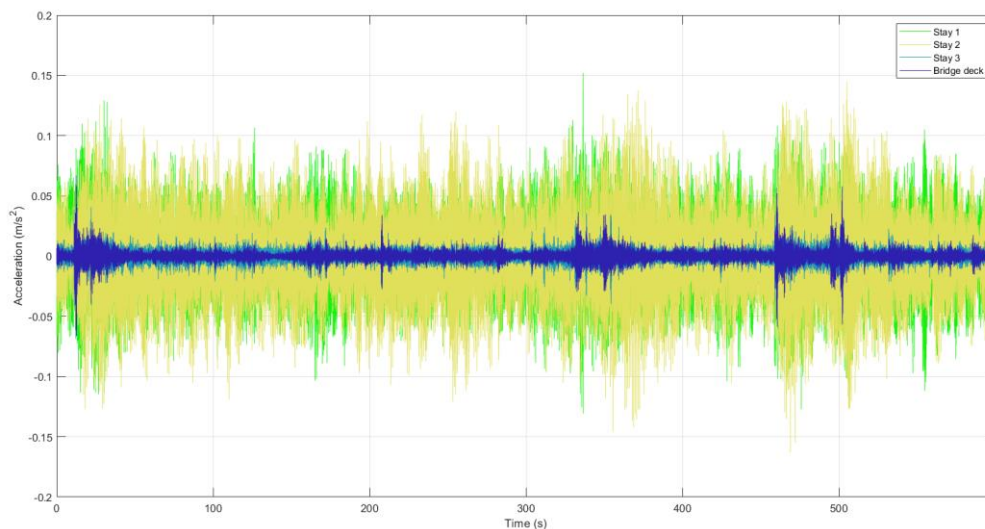
Like the displacement response in the vertical direction, stay 1 and 2 exhibit larger accelerations in the first two ten-minute measurements when the wind speed was higher. The graphs also show greater accelerations of stay 1 and 2 than stay 3 and the bridge deck. Especially clear is the lower acceleration response of stay cable 3 in the lateral direction as opposed to the vertical direction. The response of the bridge deck is noticeably smaller in the lateral than the vertical direction, with less peak accelerations.

In the 6th data set in both the vertical and lateral direction there is a peak in the response at approximately $t=450$ s, from stay cable 3 and stay cable 2 respectively. Unlike the response earlier in the data set, where a peak response in the bridge deck is followed by an immediate response in the stay cables, the response accelerations from the stay cables is delayed by a considerable amount of time.

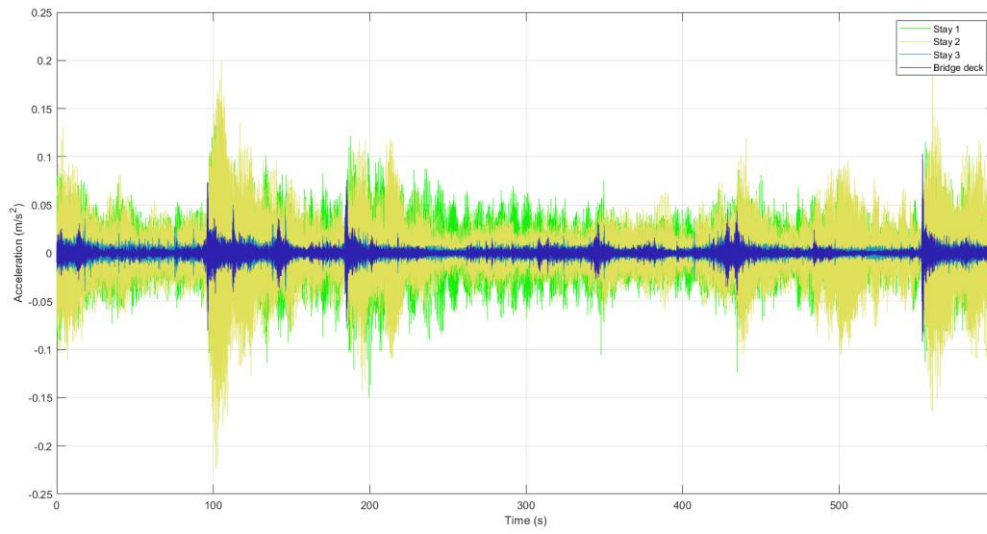
a) 1st dataset



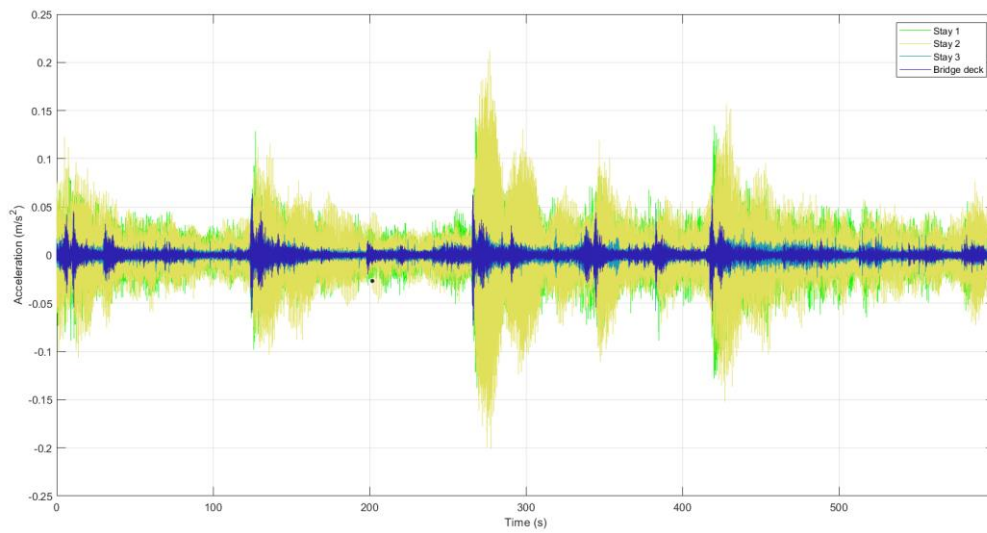
b) 2nd dataset



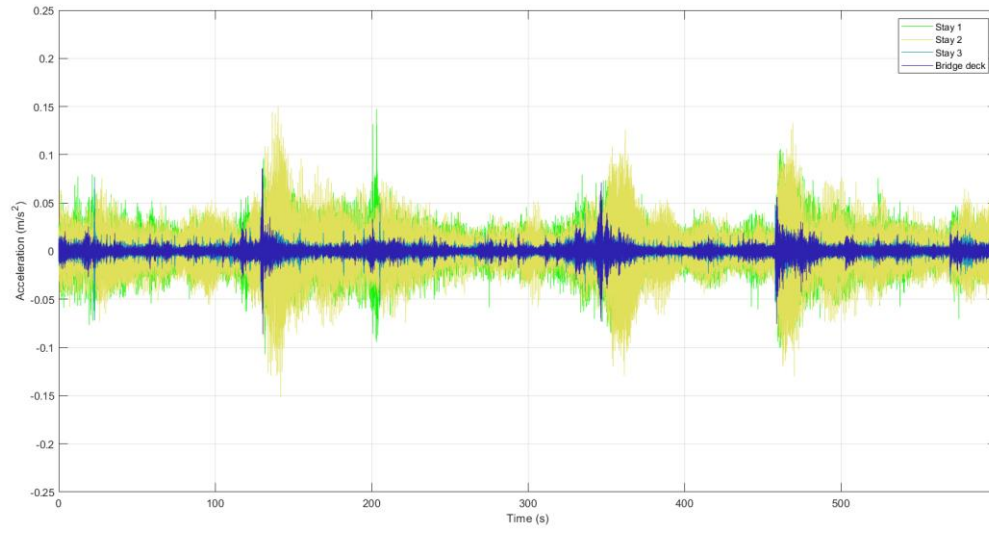
c) 3rd dataset



d) 4th dataset



e) 5th dataset



f) 6th dataset

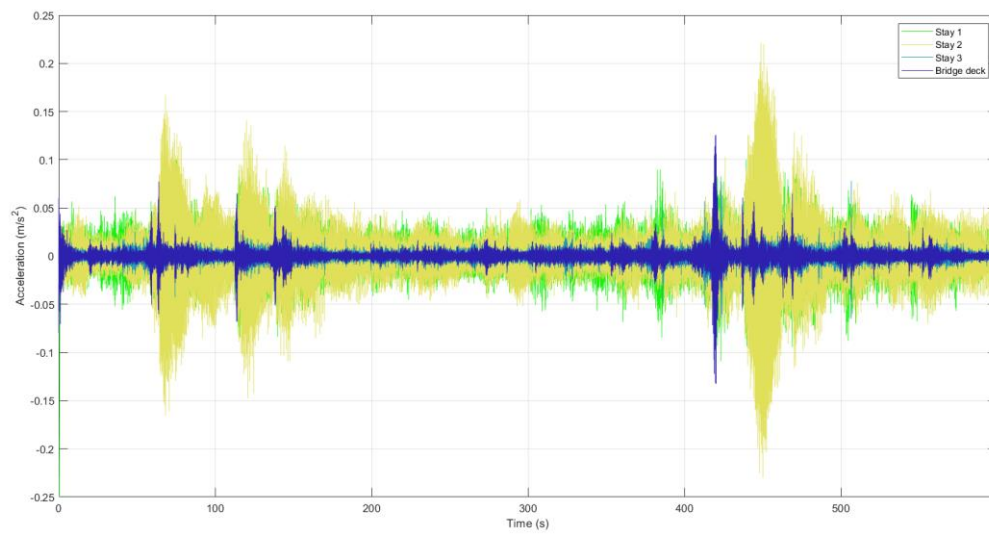


Figure 6.8 Lateral acceleration of all nodes

6.1.5 Frequency estimation

Based on an approximate calculation the tension in the back stay (stay 1) was estimated to be 940 kN in each individual stay, i.e. 3760 kN in the four stays modelled as one stay due to the crossties. The tension is likely higher than the calculated value used in the analysis, as it does not take variable loads such as traffic into account. Thus, the natural frequency is likely to be higher than the estimate.

Table 2 Frequency estimation in stay no. 1 and 2 from tension

Stay cable	No. of individual stays	Length (m)	Cable inclination	Eigenfrequency (Hz)					
				f_1	f_2	f_3	f_4	f_5	f_6
1	8	98,263	29,8	0,9	1,7	2,6	3,4	4,3	5,2
2	8	95,639	30,7	0,9	1,8	2,7	3,5	4,4	5,3

From the video taken on 15/02/2014 the frequency of the vibration of stay cable 2, which was most visible, was estimated to be in the range 3-3,3 Hz, which is slightly higher than the range for RWIV at 1-3 Hz.

6.1.6 Cable frequencies from PSD-analysis

The sampling frequency of the recording was 64 Hz and the Nyquist frequency is therefore 32 Hz for the acquired data. Natural frequencies were identified by tracing the local peak values of the density spectrum manually on the screen as depicted in the example in Figure 6.9. Some of the PSD-plots displayed several peaks not listed in the tables of identified frequencies. These are expected to be a result of global bridge vibrations, and the author has picked the peaks regarded as the result of local cable vibrations.

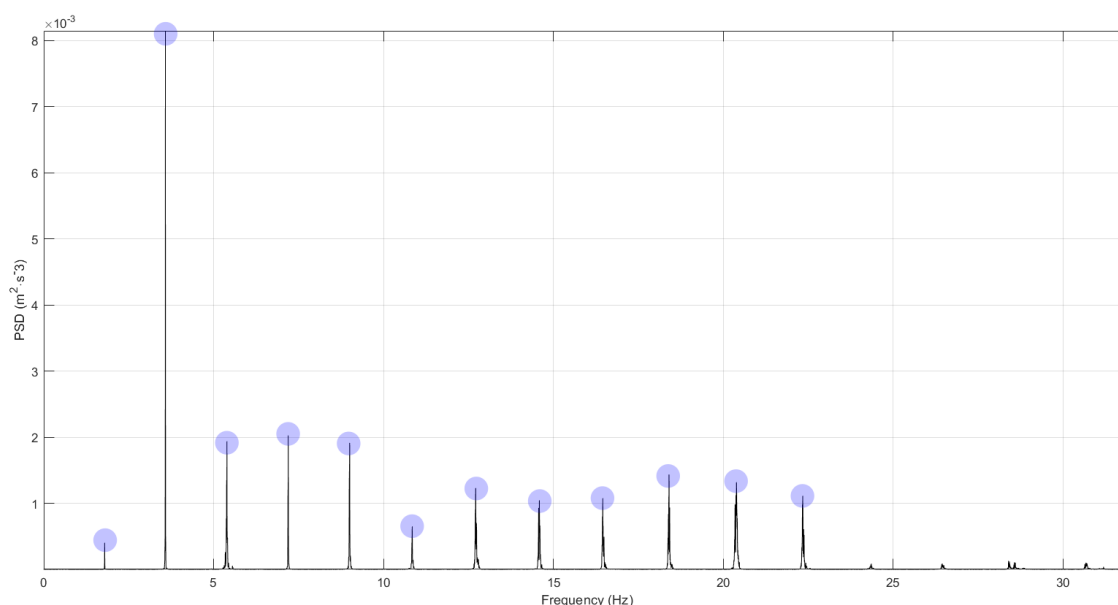


Figure 6.9 Power Spectral Density of the “vertical” acceleration of cable 3, 5th dataset

The first ten identified modes in the lateral direction and vertical direction of stay cable 1 are presented in Table 3. Generally, the identified modes in lateral and vertical direction seem to be in accordance with each other. The differences in identified frequencies for the ten data sets is relatively small. Mode 1 was not recognised in the vertical direction. The first two data sets also display modes not present in the last three data sets, and vice versa in both directions.

Table 3 Identified frequencies of stay cable 1 from PSD

Identified frequencies in y-direction (lateral)							
Identified mode	Data set						Maximum difference
	1 (Hz)	2 (Hz)	3 (Hz)	4 (Hz)	5 (Hz)	6 (Hz)	
1	-	-	-	-	-	-	-
2	2,067	2,053	2,053	2,050	2,053	2,050	0,017
3	3,100	3,090	3,087	3,083	3,080	3,083	0,020
4	4,197	4,187	4,183	4,137	4,133	4,140	0,064
5	5,160	5,147	5,143	5,137	5,153	5,143	0,023
6	-	-	5,267	5,260	5,257	5,260	0,010
7	6,230	6,19	6,203	6,203	6,200	6,200	0,040
8	6,373	6,367	-	-	-	-	0,006
9	7,220	7,200	7,220	7,203	7,213	7,220	0,020
10	7,347	7,340	7,333	-	7,303	7,313	0,044
Identified frequencies in z-direction (“vertical”)							
Identified mode	Data set						Maximum difference
	1 (Hz)	2 (Hz)	3 (Hz)	4 (Hz)	5 (Hz)	6 (Hz)	
1	1,040	1,037	1,037	1,037	1,037	1,037	0,003
2	2,060	2,057	2,053	2,053	2,050	2,050	0,010
3	3,093	3,087	3,080	3,080	3,077	3,077	0,016
4	4,197	4,187	4,183	4,173	4,173	4,170	0,027
5	-	-	4,927	4,873	4,863	-	0,064
6	5,160	5,147	5,143	5,137	5,133	5,137	0,027
7	6,207	6,190	6,187	6,180	6,167	6,177	0,040
8	6,373	6,367	6,353	-	-	-	0,020
9	7,210	7,200	-	7,190	7,183	-	0,027
10	7,347	7,340	7,333	7,327	7,313	7,313	0,034

The ten first identified natural frequencies of stay cable 2 is presented in Table 4. The frequencies are to slightly larger than the frequencies of stay cable 1, which is considered to be consistent with a slightly shorter length and higher inclination angle of cable 2 compared to cable 1. There were fewer natural modes identified in the last three data sets than the first.

Table 4 Identified frequencies of stay cable 2 from PSD

Identified frequencies in y-direction (lateral)							
Identified mode	Data set						Maximum difference
	1 (Hz)	2 (Hz)	3 (Hz)	4 (Hz)	5 (Hz)	6 (Hz)	
1	1,067	1,063	1,063	1,063	1,063	1,063	0,004
2	2,133	2,127	2,127	2,120	2,120	2,120	0,013
3	3,203	3,197	3,187	3,190	3,183	3,197	0,020
4	4,267	4,260	4,250	4,267	4,250	4,250	0,017
5	5,330	5,137	-	-	5,310	5,327	0,193
6	5,436	5,453	5,437	5,317	5,440	-	0,136
7	6,413	6,400	6,420	6,407	6,410	6,410	0,020
8	6,563	6,543	-	-	-	-	0,020
9	7,467	7,457	7,450	7,460	7,487	7,447	0,040
10	7,530	7,507	-	-	-	-	0,023
Identified frequencies in z-direction (“vertical”)							
Identified mode	Data set						Maximum difference
	1 (Hz)	2 (Hz)	3 (Hz)	4 (Hz)	5 (Hz)	6 (Hz)	
1	1,073	1,073	1,073	1,070	1,070	1,070	0,003
2	2,130	2,127	2,123	2,120	2,120	2,120	0,010
3	3,197	3,190	3,187	3,183	3,183	3,193	0,014
4	4,343	4,337	4,330	4,327	4,250	4,247	0,096
5	5,327	5,317	5,307	5,327	5,323	5,327	0,020
6	5,467	5,450	5,440	-	-	-	0,027
7	6,413	6,400	6,420	6,390	6,410	6,413	0,030
8	6,563	6,543	6,543	-	-	-	0,020
9	-	-	7,503	7,493	7,487	7,447	0,056
10	7,593	7,573	-	-	-	7,513	0,080

Table 5 and Table 6 show the six estimated frequencies compared to the first identified frequencies of stay cable 1 and stay cable 2, respectively. As expected, the estimated frequencies were lower than the observed frequencies. Common for the modes 2-5 in all the cases is an average percentage of difference for the estimated and identified frequencies around 20%, whereas the difference percentage drops significantly for the 6th mode for all the cases to around 2%. Overall, the frequencies of stay cable 2 is slightly higher than the frequencies of stay cable 1. Overall the difference between consecutive frequencies remained consistent, both for the estimated frequencies and the identified average frequencies in the y-and z-direction.

Table 5 Difference between estimated frequencies and averaged identified frequencies from PSD-analysis of stay cable 1

Mode	Estimated frequency	Average identified frequency in y-direction	Difference (%)	Average identified frequency in z-direction	Difference (%)
1	0,9	-	-	1,0	15,3
2	1,7	2,1	20,8	2,1	20,8
3	2,6	3,1	18,7	3,1	18,6
4	3,4	4,2	22,4	4,2	23,0
5	4,3	5,1	19,7	4,9	13,7
6	5,2	5,3	1,2	5,1	-1,1

Table 6 Difference between estimated frequencies and averaged identified frequencies from PSD-analysis of stay cable 2

Mode	Estimated frequency	Average identified frequency in y-direction	Difference (%)	Average identified frequency in z-direction	Difference (%)
1	0,9	1,1	18,2	1,1	19,1
2	1,8	2,1	18,0	2,1	18,0
3	2,7	3,2	18,3	3,2	18,1
4	3,5	4,3	21,6	4,3	23,0
5	4,4	5,3	19,9	5,3	20,9
6	5,3	5,4	2,2	5,5	2,9

Table 7 shows the identified frequencies of stay cable 3. This is the shortest cable in the analysis, and the natural frequencies are clearly higher than the frequencies for the other two stay cables considered. In addition, the difference between the consecutive identified modes are greater than for stay cable 1 and 2. There are also several frequency modes not present in the identified frequencies in a given direction. Most noticeable is that mode 6 and 8 are not present in the lateral direction. In both directions, there are several frequencies present in the first two and three data sets, which are not present in the subsequent data sets. The difference between identified frequencies in y- and -z-direction does not seem to be large.

Table 7 Identified frequencies from stay cable 3 from PSD-analysis

Identified frequencies in y-direction (lateral)							
Identified mode	Data set						Maximum difference
	1 (Hz)	2 (Hz)	3 (Hz)	4 (Hz)	5 (Hz)	6 (Hz)	
1	1,800	1,797	1,797	1,797	1,793	1,800	0,007
2	3,597	3,587	3,583	3,583	3,583	3,583	0,014
3	5,410	5,393	5,397	5,390	5,383	5,394	0,027
4	6,727	6,700	6,697	-	-	-	0,030
5	7,233	7,213	7,203	7,210	7,200	7,220	0,033
6	-	-	-	-	-	-	-
7	9,040	9,023	9,010	9,017	9,013	9,023	0,030
8	-	-	-	-	-	-	-
9	10,900	10,860	10,860	10,870	10,850	10,860	0,050
10	12,780	12,740	12,730	12,730	12,730	12,740	0,050
Identified frequencies in z-direction ("vertical")							
Identified mode	Data set						Maximum difference
	1 (Hz)	2 (Hz)	3 (Hz)	4 (Hz)	5 (Hz)	6 (Hz)	
1	1,797	1,797	1,793	1,793	1,793	1,793	0,004
2	3,593	3,587	3,583	3,580	3,580	3,580	0,013
3	5,407	5,393	5,390	5,390	5,393	5,403	0,017
4	5,577	5,573	5,563	5,560	-	-	0,017
5	7,223	7,207	7,203	7,197	7,197	7,203	0,026
6	7,483	7,467	-	-	-	-	0,016
7	9,033	9,017	9,000	9,007	9,007	9,010	0,033
8	9,427	9,403	-	-	-	-	0,024
9	10,880	10,860	10,850	10,840	10,850	10,860	0,040
10	12,750	12,730	12,710	12,710	12,720	12,730	0,040

Table 8 presents the identified natural frequencies from the bridge decks. In comparison with the identified frequencies for the cables, the difference between the modes in y- and z-direction is much more obvious since the bridge deck and the global bridge structural system have different stiffnesses in the two directions. The tracing of peaks to identify natural frequencies of the bridge deck was more challenging because of the nature of the graph. Therefore, only the first eight modes are presented. Generally, the identified frequencies are lower than those found for the stay cables, reflecting the flexibility of the bridge, as the main span is 185 m and supported only by the 10 stay cables and the pylon.

Table 8 Identified frequencies of bridge deck from PSD-analysis

Identified frequencies in y-direction (lateral)							
Identified mode	Data set						Maximum difference
	1 (Hz)	2 (Hz)	3 (Hz)	4 (Hz)	5 (Hz)	6 (Hz)	
1	0,210	0,2167	0,170	0,153	0,123	0,4067	0,283
2	0,9633	0,903	0,917	0,890	0,860	0,8733	0,103
3	1,650	1,653	1,667	1,757	1,677	1,723	0,107
4	2,030	1,873	2,017	-	-	2,067	0,194
5	2,770	2,600	2,617	-	-	2,557	0,213
6	3,687	2,857	2,937	2,933	3,010	2,990	0,830
7	4,223	4,107	4,220	4,150	4,183	4,207	0,116
8	4,877	4,883	4,953	4,943	4,940	5,000	0,123
Identified frequencies in z-direction (“vertical”)							
Identified mode	Data set						Maximum difference
	1 (Hz)	2 (Hz)	3 (Hz)	4 (Hz)	5 (Hz)	6 (Hz)	
1	0,216	-	-	0,270	0,213	-	0,057
2	0,310	-	-	-	-	-	-
3	0,447	0,460	0,403	0,447	-	0,407	0,057
4	0,937	0,953	0,937	0,890	-	0,870	0,083
5	1,457	1,277	1,493	1,490	1,493	1,537	0,260
6	-	-	-	-	-	1,953	-
7	2,543	2,990	-	-	2,983	2,950	0,447
8	3,660	3,643	3,637	3,657	3,647	3,647	0,023

6.1.7 Damping estimation

As no recording of passing vehicles was performed, it is difficult to ascertain which vibrations can be considered free oscillations after short transient excitation (e.g. by traffic) and which vibrations are due to wind loads, traffic loads or other variables.

An attempt at estimating the damping of the stay cables and the bridge was conducted by filtering the acceleration response. However, it was difficult to obtain a satisfactory result, which could be fit to an exponential equation.

As an alternative the so-called “half-power bandwidth method” based on the influence of damping on the resonant part of the response power spectral density has been used to estimate the damping level.

The first six peaks of the PSD of the 4th data set were used to obtain an average value for the cables and the bridged deck. The average damping ratio is presented in Table 9. As the average values were noticeably influenced by several high values, the median is also presented. The damping ratio of the bridge deck has the highest value, both the average and the median are higher than either of the stay cables. This matches the acceleration responses seen in Figure 6.7 and Figure 6.8. Although the initial response amplitude is greater, the consecutive bridge deck response declines rapidly.

Surprisingly, the average damping ratio of stay cable 2 is slightly higher than the damping ratio of stay cable 1 and stay cable 3. This could be due to uncertainties regarding the method used, as it is not viewed as the most reliable. Further research is recommended to determine the damping ratio. The values for each mode are attached in appendix G.

Table 9 Estimated damping ratio

	Average estimated damping ratio (%)	Median of estimated damping ratio (%)
Stay cable 1	0,122	0,114
Stay cable 2	0,172	0,162
Stay cable 3	0,090	0,074
Bridge deck	0,568	0,288

6.2 Weather statistics

6.2.1 Wind rose

In Figure 6.10 a wind rose from hourly wind data from 2005-2018 is presented. The main wind direction is the south/south-east direction (120-180°), and the north/north-east direction (300-360°). Wind speeds vary from zero to 15 m/s, with wind speeds exceeding 15 m/s primarily from the north/north-west. This substantiates that the conditions favourable for the RWIV can be expected at Bybrua. As seen in section 0, there are quite large seasonal differences. The majority of the wind from the south-east direction can therefore be assumed to occur in the period October to March.

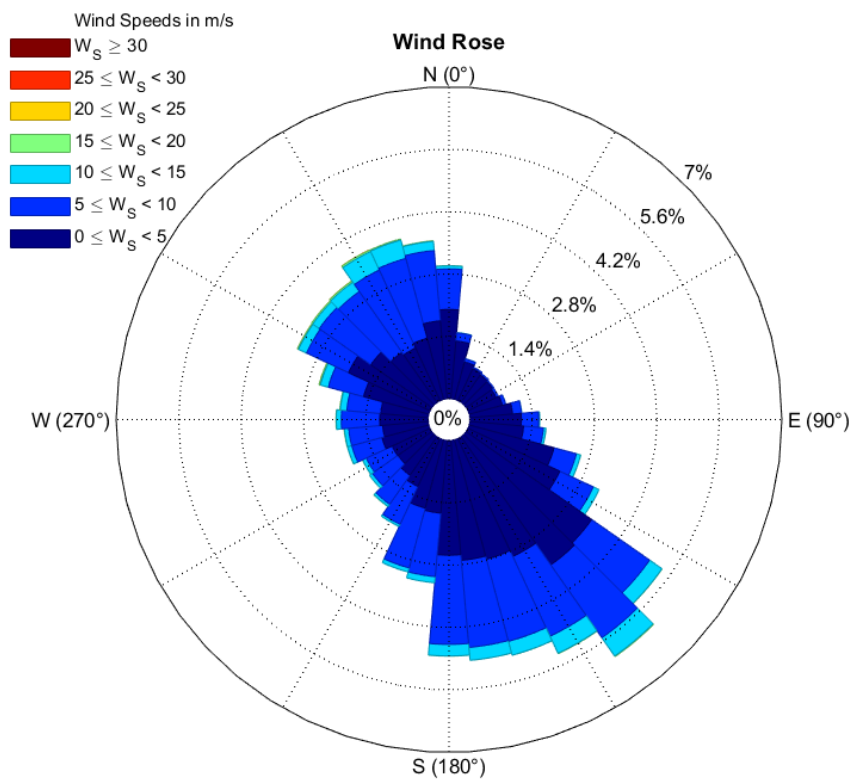


Figure 6.10 Wind rose from Sola from 2005-2018. MATLAB code borrowed from [27].

6.2.2 Weibull distribution of mean wind speed

The hourly mean wind speeds were fitted to a Weibull distribution as depicted in Figure 6.11. The shape parameters best fit were found to be $k=1,56991$ and $c=5,11254$. Although the distribution seems to overestimate the values around 2 m/s and 3 m/s to some extent, it is considered a reasonable result. The CFD for this sample is therefore

$$p(x) = \frac{1,56991}{5,11254} \left(\frac{x}{5,11254} \right)^{1,56991-1} \exp\left(-\left(\frac{x}{5,11254}\right)^{1,56991}\right) \quad 6.1$$

Ans the PDF is

$$p(> x) = \exp\left(-\left(\frac{x}{5,11254}\right)^{1,56991}\right) \quad 6.2$$

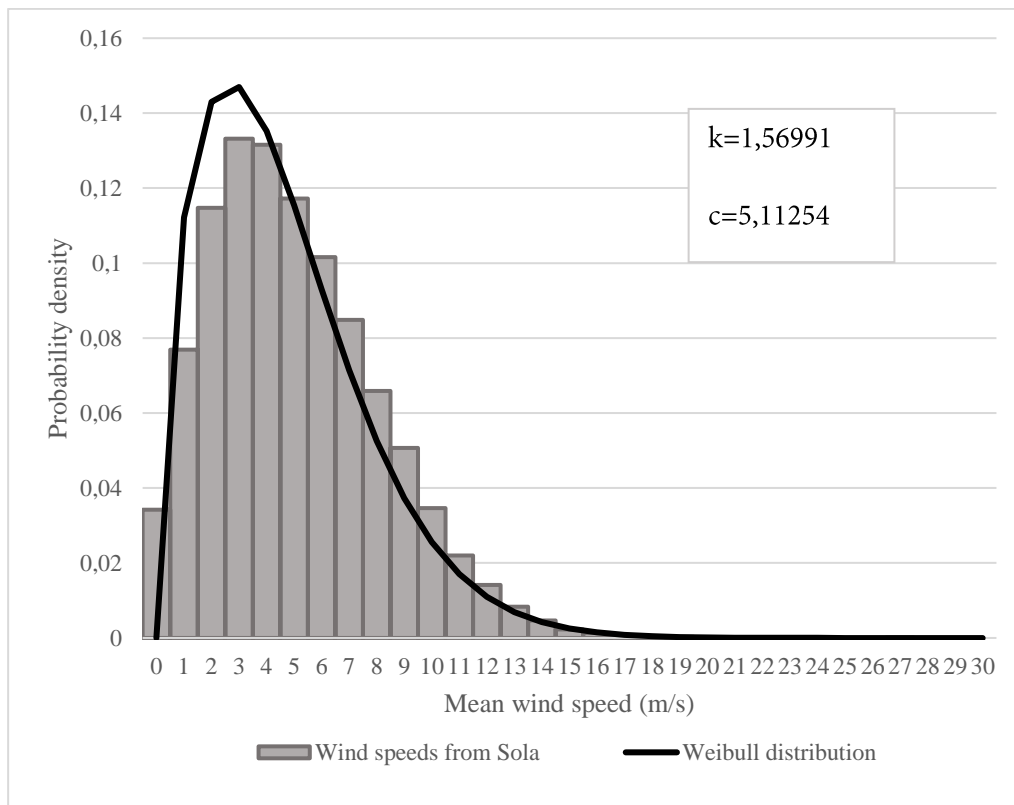


Figure 6.11 Wind speeds and Weibull distribution

6.2.3 Days with reported cable vibrations

Table 10 shows the weather conditions at the time of reported cable vibrations. The hours closest to the reported time of observed vibrations are included. For observation 1, on 30/11/1999, there were only reports for every three hours, so only one hour is included. The wind direction on 30/11/1999 is 220°. This is just within the wind direction related to RWIV. The temperatures for the observations ranged from 5,3 to 14 °C. There were no temperatures below zero. The wind speed ranges from 2,0 to 11,8 m/s. The lowest value is seen in observation 2, where we also see the heaviest rainfall with 5,3 mm/hour.

Table 10 Weather at the time of observed cable vibrations

Observation	Date and time	Time of observation	Wind direction (°)	Wind speed (m/s)	Rainfall (mm/hr)	Temperature °C
1	30/11/1999 13:00	13:15	220	11,8	1,9	9,1
2	06/09/2009 15:00	15:20	304	2,0	3,2	13,3
	06/09/2009 16:00		108	2,8	5,3	13,7
3	15/02/2014 10:00	10:35	149	8,7	1	5,4
	15/02/2014 11:00		154	9,4	1,6	6,4
4	01/11/2018 14:00	14:45	131	9,8	0,1	10,2
	01/11/2018 15:00		125	11,1	0,3	11,2
5	7/12/2018 14:00	14:40	118	6,9	0,9	7
	7/12/2018 15:00		100	5,9	1,1	6,9

From Table 11, the possibility of the vibrations being RWIV based on criteria described in section 5.5.1 is presented. Of the five dates of reported cable vibrations, only observation 2 had heavier rainfall than 2,5 mm/hour. Therefore, none of the other observations had vibrations which were present in what is known as moderate rainfall, where the majority of reported RWIV find themselves. Nevertheless, the vibrations could be RWIV, as four of the reported incidents have reported rainfall above 0,1 mm/hour. While the amount of rain for observation 2 was substantial, the wind speed of this observation was well below the wind speed assumed to induce cable vibrations. In addition, the wind direction for this observation shifted from 304° at 15:00 to 108° at 16:00.

Table 11 Is there a possibility of RWIV based on different criteria?

Observation	Date and time	Rainfall >0 mm/hour		Rainfall > 0,1 mm/hour		Rainfall >2,5 mm/hour	
		Wind speed	Wind speed	Wind speed	Wind speed	Wind speed	Wind speed
		5-20 m/s	8-12 m/s	5-20 m/s	8-12 m/s	5-20 m/s	8-12 m/s
1	30/11/1999 13:00	Yes	Yes	Yes	Yes	No	No
2	06/09/2009 15:00	No	No	No	No	No	No
	06/09/2009 16:00	No	No	No	No	No	No
3	15/02/2014 10:00	Yes	Yes	Yes	Yes	No	No
	15/02/2014 11:00	Yes	Yes	Yes	Yes	No	No
4	01/11/2018 14:00	Yes	Yes	No	No	No	No
	01/11/2018 15:00	Yes	Yes	Yes	Yes	No	No
5	7/12/2018 14:00	Yes	No	Yes	No	No	No
	7/12/2018 15:00	No	No	No	No	No	No

Vibrations in stay number 3, the cable closest to the pylon could perhaps be due to wake effects, as it theoretically does not fit the criteria for RWIV. Vibrations at this stay is visible, but the oscillations may be due to the turbulent flow from the pylon or the adjacent individual cables. If the wind is blowing in a south/south-east direction, the pylon and the other stay cables could create wakes affecting stay cable 1,2, and 3. This is visualised in Figure 6.12.

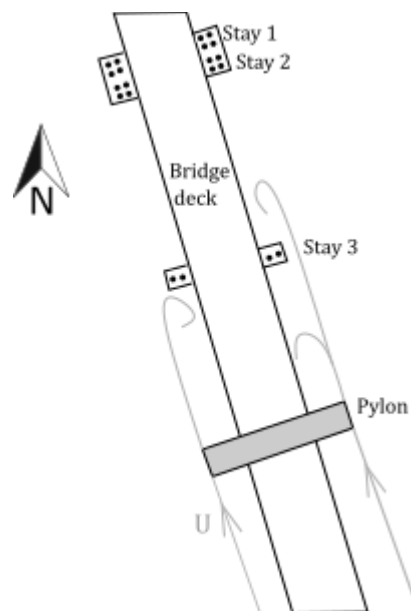


Figure 6.12 Visualization of possible wake effects at Bybrua

6.2.4 Estimated hours of vibrations

The aim was initially to examine data for the whole lifetime of the bridge, from 1978-2019, but prior to 1999 rainfall and wind data were not reported hourly and were therefore excluded from the analysis. As a result, data on wind direction and wind velocity from Sola from 2005 up until 2019 were used, and data on hourly rainfall from either Våland or Hundvåg were used. These weather stations were in operation at different times during the years examined. Rain data from Våland was preferred, due to its proximity of the bridge. However, data was only reported here from 1999-2000, and after this from July 2008 to 2019. Thus, data from either Hundvåg was used for rain data in the period in between. As a result, hourly data from January 2005 until December 2018 was included in the analysis. Hours where data of either wind speed, wind direction or rain was missing were excluded.

Number of hours with weather conditions favourable for the RWIV and their percentage of the total hours considered are presented in Table 12. The total number of hours examined was 121625, corresponding to 99,17% of the total number of hours from January 1st 2005 until December 31st 2018. The table shows the percentage of hours where RWIV could be expected to occur, with varying amount of rainfall and within two different wind speed ranges. The wind direction considered is $\pm 60^\circ$ from the bridge axis as described in section 5.5.1. The percentage of hours of possible RWIV decreases as the criteria for vibrations are narrowed down.

As this is only performed for the years 2005-2018, the hours only represent 13 years. The bridge has been in use for almost 41 years. Assuming the weather conditions has remained somewhat consistent, the percentage of hours will likely be within the same range. The number of hours where the weather conditions could facilitate RWIV for the whole lifetime of the bridge are presented in Table 13. There is not much difference between the estimated number of hours between >0 mm/hour and $>0,1$ mm/hour. But for moderate rainfall ($>2,5$ mm/hour), the number drops significantly. This number does not consider that heavy rainfall may hinder a rivulet formation. The biggest difference is between the ranges of wind speed. All but two cases of observed cases of reported vibrations were found to have wind speeds in the range 8-12 m/s.

Table 12 Possible hours of RWIV from 2005-2018

Wind speed (m/s)	Rainfall					
	>0 mm/hour		$>0,1$ mm/hour		$>2,5$ mm/hour	
	No. of hours	Percentage, %	No. of hours	Percentage, %	No. of hours	Percentage, %
5-20	6404	5,27	5303	4,36	687	0,57
8-12	2263	1,86	1921	1,58	303	0,25

Table 13 Estimated number of hours with possible RWIV for the whole lifetime of Bybrua

Wind speed (m/s)	Numbers of hours		
	>0 mm/hour	$>0,1$ mm/hour	$>2,5$ mm/hour
5-20	18928	15659	2047
8-12	6680	5675	898

7 Conclusion and further work

The thesis aimed to assess the possibility of rain-wind induced vibrations at Bybrua by examining weather conditions at the time of observed vibrations and estimate the possible number of hours the bridge could have been subjected to RWIV. The acceleration response, frequency and damping ratio based on six ten-minute recordings has been evaluated, along with recorded wind velocity and wind directions from the same period. The identified frequencies differed from the estimated frequencies by about 20%. This was consistent for the first five modes, however the difference for the 6th mode was in the range -1,1 to 5,4%. There were not large differences in the identified frequencies in the lateral (y-direction) and the vertical (z-direction) of either of the stays or the bridge deck. The differences in the estimated and the identified frequency of stay cable 1 and stay cable 2 is likely due to an oversimplification in the calculations of the estimated frequency

Based on the findings it is reasonable to assume that the bridge has been, and in the future could be subjected to cable vibrations in the form of RWIV. Based on the weather data presented in this thesis, it can also be assumed that four of the observed incidents of cable vibrations has been due to the combined effects of rain and wind loads. Nevertheless, long-term monitoring of the bridge should be implemented, in order to measure the acceleration response, amplitude and weather conditions at the time of believed RWIV to be able to ascertain the presence of these vibrations at Bybrua.

Also, the possibility of the vibrations being a product of wake effects should be explored. As the south/south-east direction is the most prominent wind direction in the winter months, the vibrations could also be wake effects. Additionally, a Weibull distribution could be fit to different wind directions and a probability function for rainfall to obtain a joint probability function for RWIV.

Further work should be done to establish the damping ratio and the frequencies of the bridge deck and the cables, in order to evaluate the impact of possible vibrations on the fatigue life of the bridge.

8 References

1. Xu, Y.L., *Wind Effects on Cable-Supported Bridges*. 2013: Singapore: John Wiley & Sons Inc.
2. Caetano, E.d.S., *Cable vibrations in cable-stayed bridges*. Structural engineering document, ed. B. International Association for and E. Structural. Vol. 9. 2007, Zürich: International Association for Bridge and Structural Engineering IABSE.
3. Christiansen, H., f. Universitetet i Stavanger Det teknisk-naturvitenskapelige, and m. Universitetet i Stavanger Institutt for konstruksjonsteknikk og, *Aerodynamics of bridge stay cables : wind tunnel studies*. 2016, University of Stavanger, Faculty of Science and Technology, Department of Mechanical and Structural Engineering and Materials Science: Stavanger.
4. Svensson, H., *Cable-stayed bridges : 40 years of experience worldwide*, in *Cable-stayed bridges : forty years of experience worldwide*. 2012, Ernst & Sohn: Zeuthen.
5. Hikami, Y. and N. Shiraishi, *Rain-Wind Induced Vibrations of Cables in Cable Stayed Bridges*. Vol. 29. 1988. 409-418.
6. Gimsing, N.J. and C.T. Georgakis, *Cable supported bridges : concept and design*. 2012, John Wiley & Sons: Chichester, U.K.
7. Walther, R., *Cable stayed bridges*. 1999: Thomas Telford.
8. Holmes, J.D., *Wind loading of structures*. 3rd ed. ed. 2015, Boca Raton, Fla: CRC press.
9. Wenzel, H., *Health monitoring of bridges*. 2009, Wiley: Chichester, U.K.
10. Virlogeux, M., *State-of-the-art in cable vibrations of cable-stayed bridges*. Bridge Structures, 2005. **1**(3): p. 133-168.
11. Seidel, C. and D. Dinkler, *Rain-wind induced vibrations – phenomenology, mechanical modelling and numerical analysis*. Computers & Structures, 2006. **84**(24): p. 1584-1595.
12. Flamand, O., *Rain-wind induced vibration of cables*. Journal of Wind Engineering and Industrial Aerodynamics, 1995. **57**(2): p. 353-362.
13. Simiu, E. and D.H. Yeo, *Wind Effects on Structures: Modern Structural Design for Wind*. 2019: Wiley.
14. Matsumoto, M., et al., *Aerodynamic behavior of inclined circular cylinders-cable aerodynamics*. Journal of Wind Engineering and Industrial Aerodynamics, 1990. **33**(1): p. 63-72.
15. Matsumoto, M., et al., *Vortex-induced cable vibration of cable-stayed bridges at high reduced wind velocity*. Journal of Wind Engineering & Industrial Aerodynamics, 2001. **89**(7): p. 633-647.
16. Norkart AS. 2019: <https://kommunekart.com/>.
17. Selberg, A., P. Aune, and I. Holand. *Norwegian bridge building : a volume honouring Arne Selberg*. 1981. [Trondheim]: Tapir.
18. International Database and Gallery of Structures. 2019 [cited 2019 14.06]; Available from: <https://structurae.net/structures/stavanger-city-bridge>.
19. Statens Vegvesen, *Vegkart*. 2019, Statens Vegvesen.
20. Devold, E.M., et al., *Vegvalg: nasjonal verneplan : veger, bruer, vegrelaterte kulturminner*. 2002, [Oslo]: Statens vegvesen, Vegdirektoratet. 293 s. ill. 30 cm.
21. Hjorth-Hansen, E. and R. Sigbjörnsson, *Aerodynamic stability of box girders for the proposed Strømstein bridge*. 1975, Trondheim: Division of Structural Mechanics, The Norwegian Institute of Technology, University of Trondheim.
22. Dannevig, P. *Rogaland - klima*. Klima i Norge 2019 07.05.2019]; Available from: https://snl.no/Rogaland_-_klima.

23. Meteorologisk Institutt. *eKlima*. 2019; Available from: <http://eklima.met.no>.
24. Strømmen, E., *Theory of Bridge Aerodynamics*. 2 ed. ed. 2010: Germany: Springer Verlag.
25. Newland, D.E., *An introduction to random vibrations, spectral & wavelet analysis*. 3rd. ed, ed. D.E. Newland. 2005, Mineola, N.Y: Dover.
26. Rao, S.S. and Y.F. Fah, *Mechanical vibrations*. 5th ed.in SI Units. ed. Always learning. 2011, Singapore: Pearson/Prentice Hall.
27. Pereira, D. *Wind rose*. 2015; Available from: <https://se.mathworks.com/matlabcentral/fileexchange/47248-wind-rose>.

9 Appendix

Appendix A: Acceleration data for all nodes in x-, y- and z-direction

Appendix B: PSD for all nodes in x-, y- and z-direction

Appendix C: G-link 200 and WASDA-2000 datasheet

Appendix D: MATLAB code

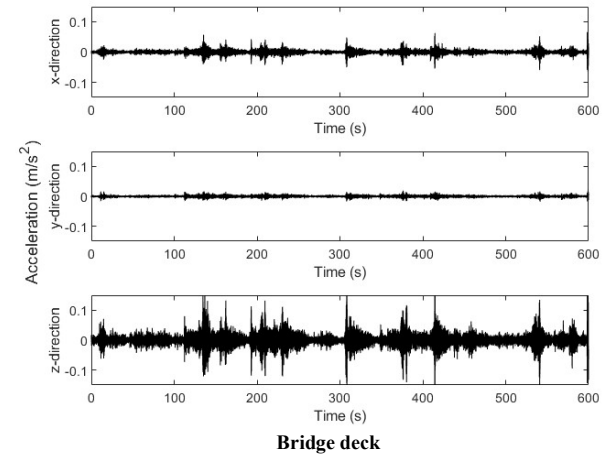
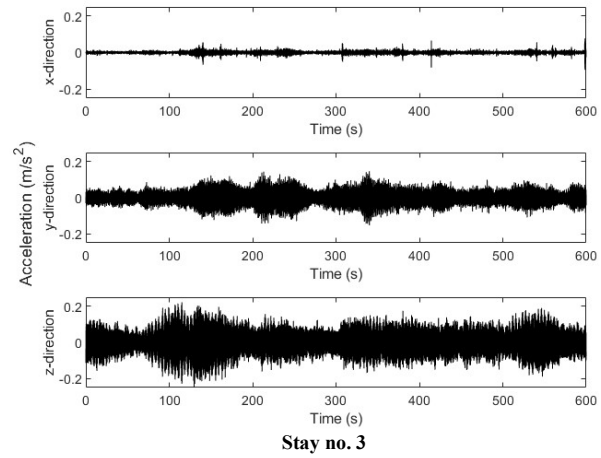
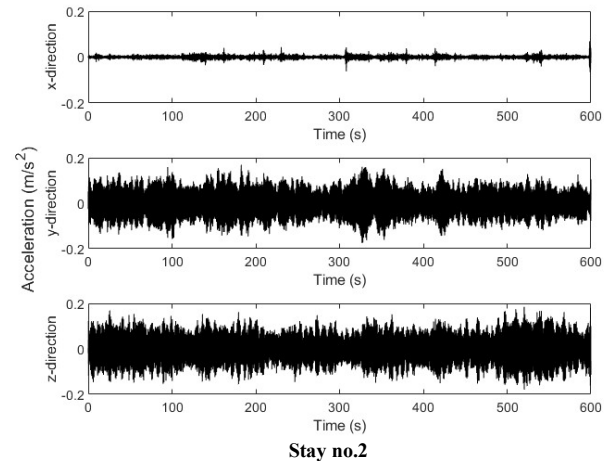
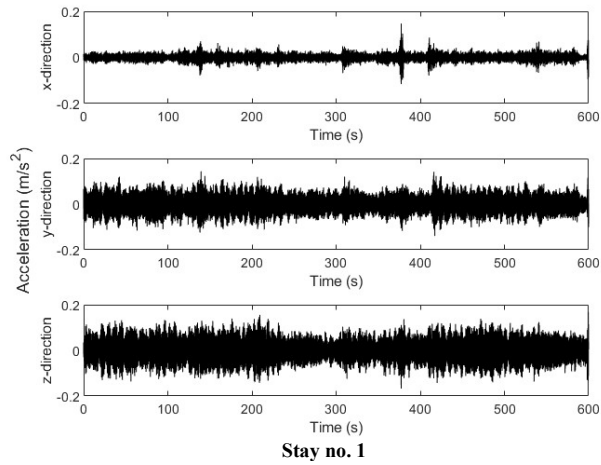
Appendix E: Weather on the days of observed vibrations

Appendix F: Calculation of tensile forces in the stays

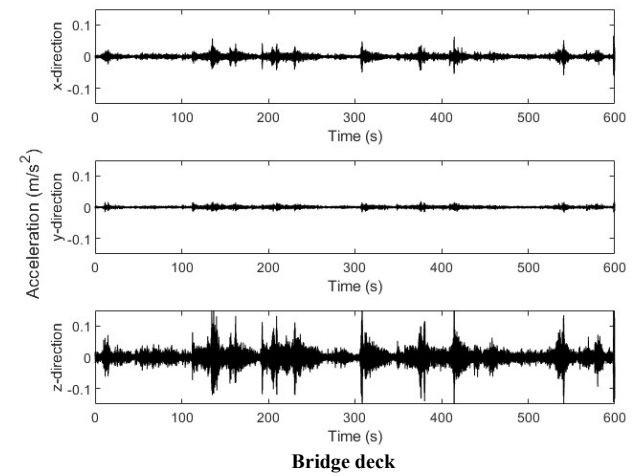
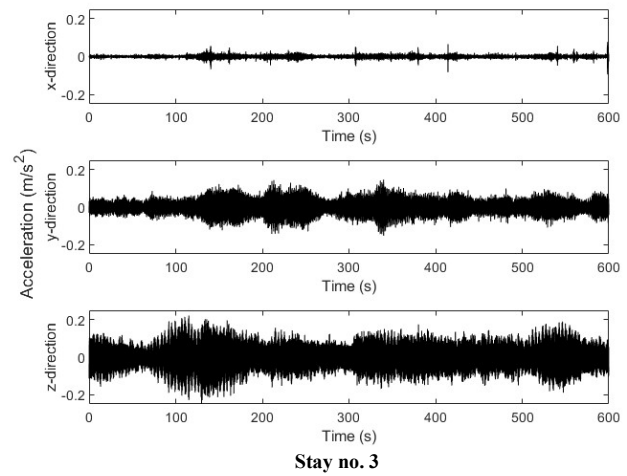
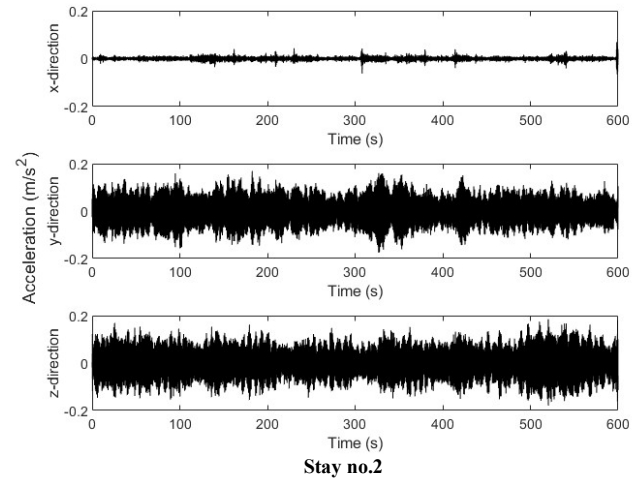
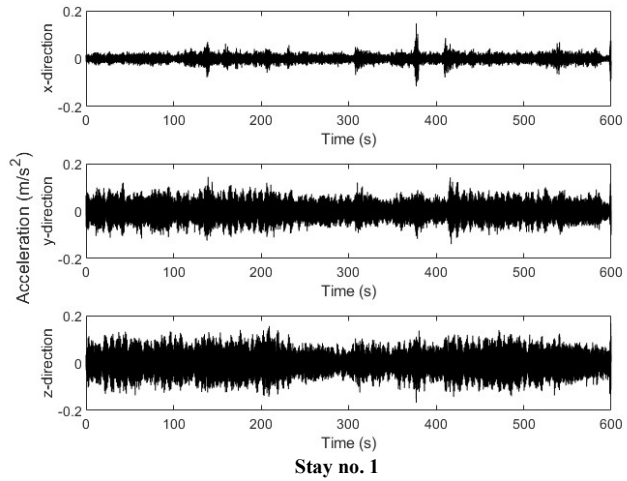
Appendix G: Damping ratio of each mode

Appendix A: Non-filtered acceleration response from data collection on 10/04/2019

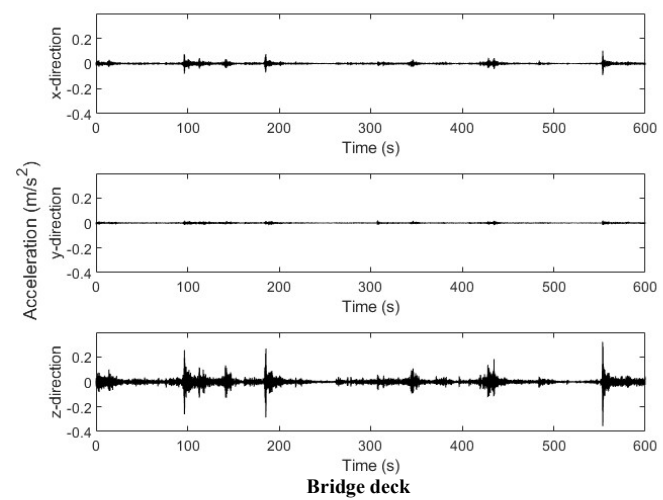
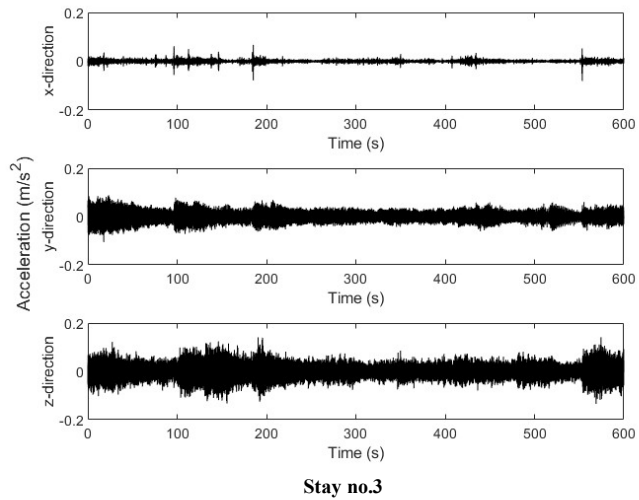
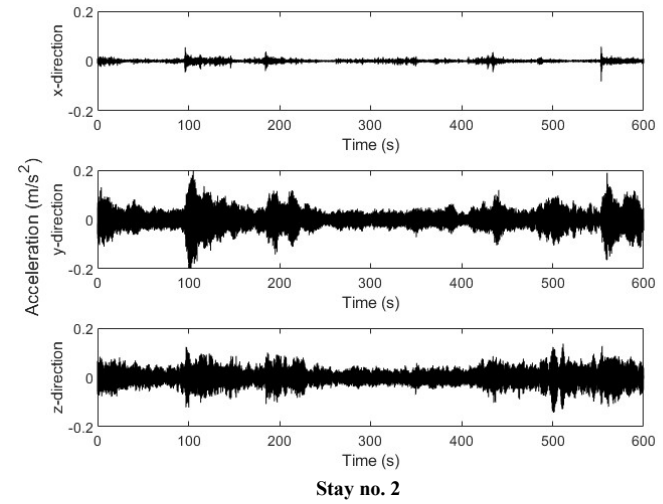
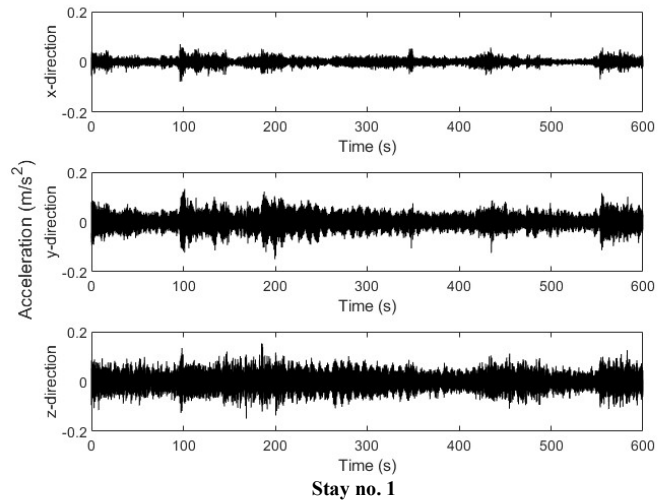
1st measurement:



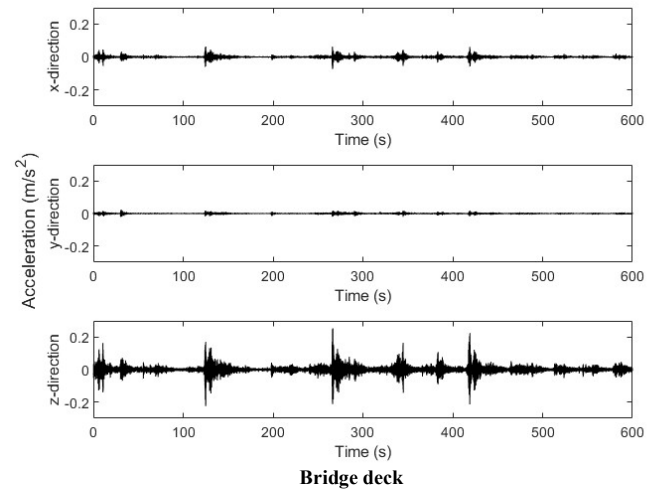
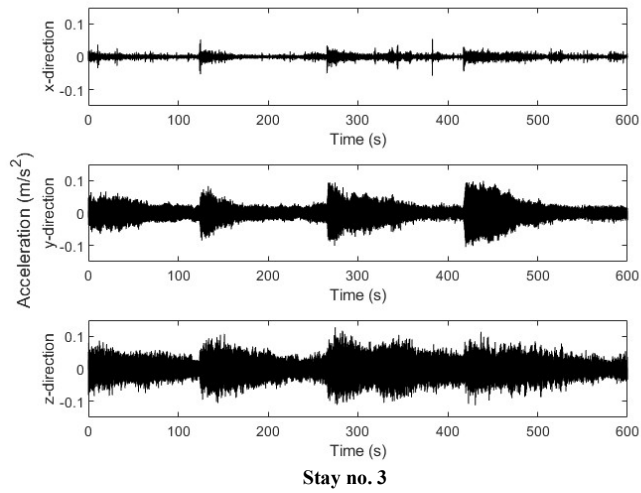
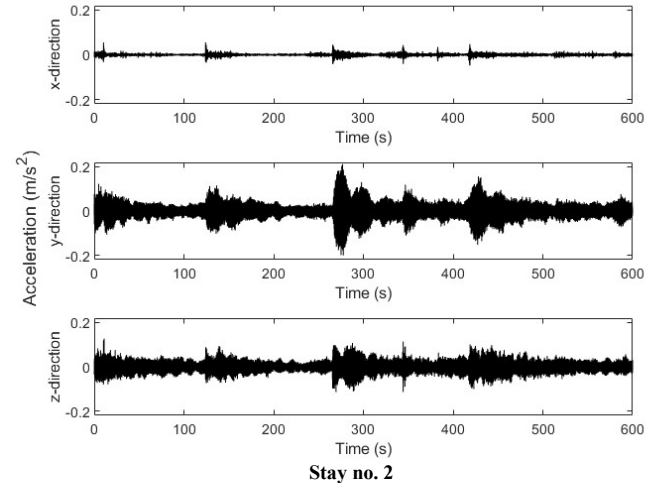
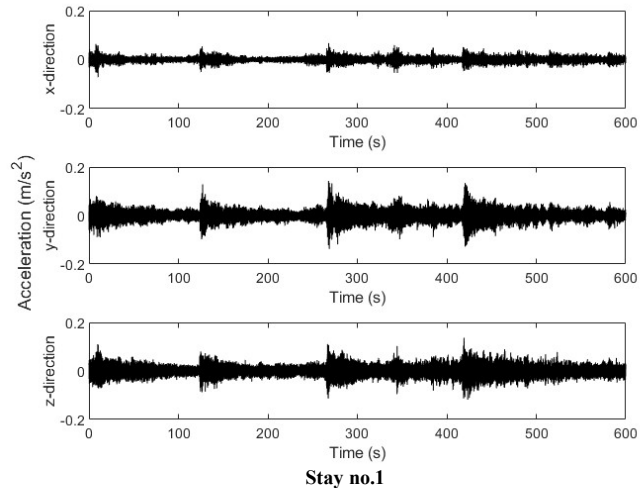
2nd measurement



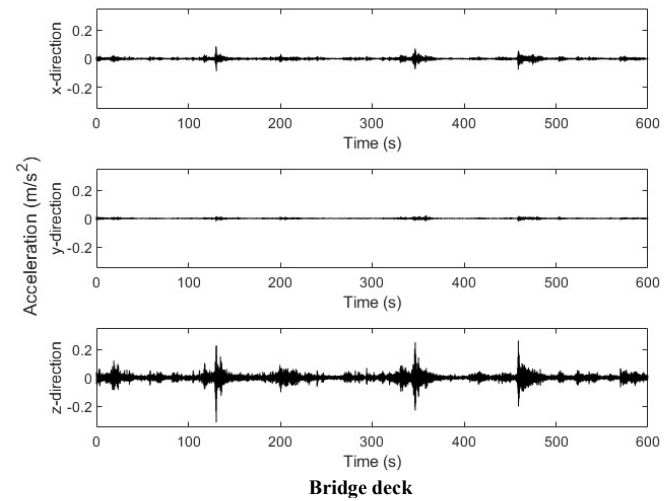
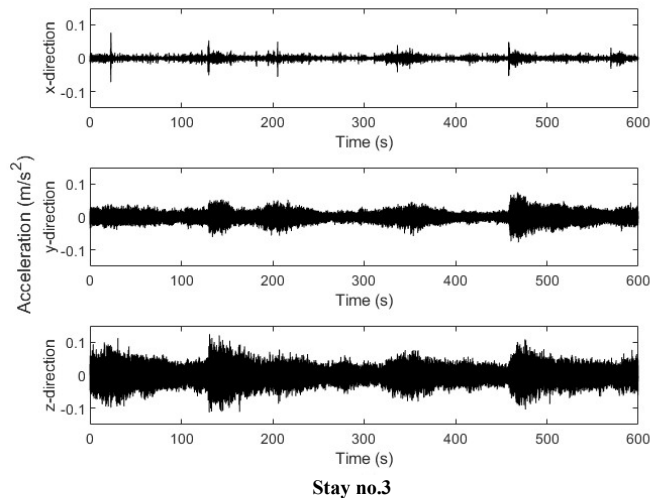
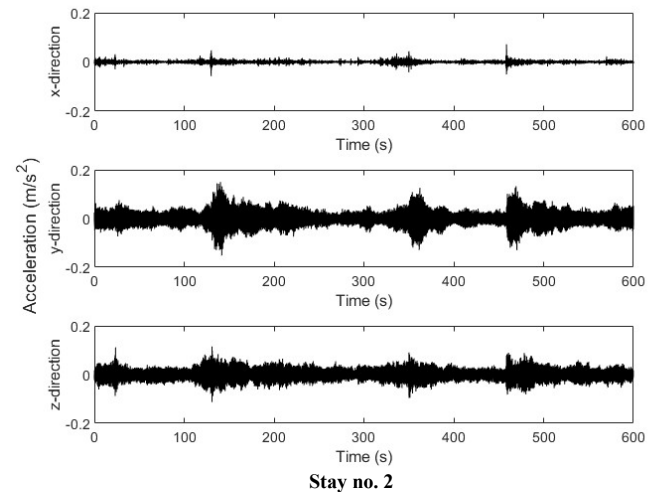
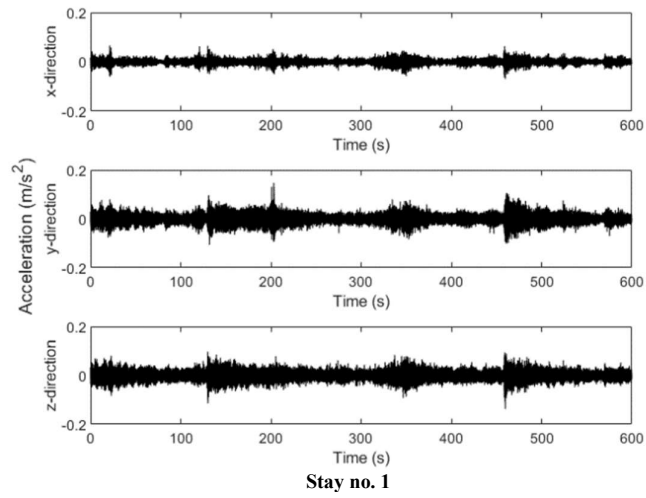
3rd measurement



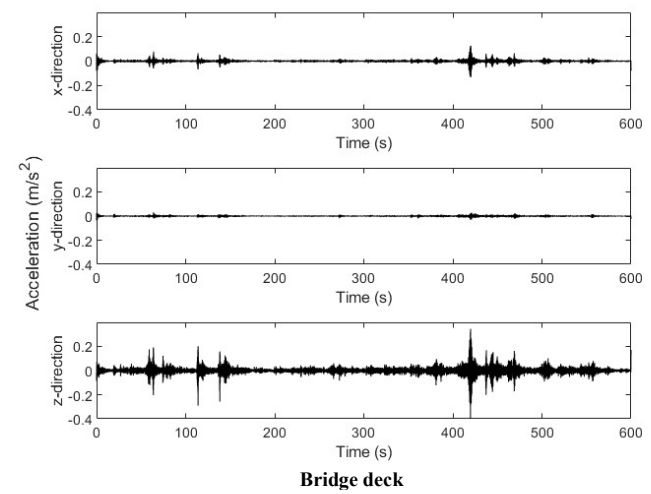
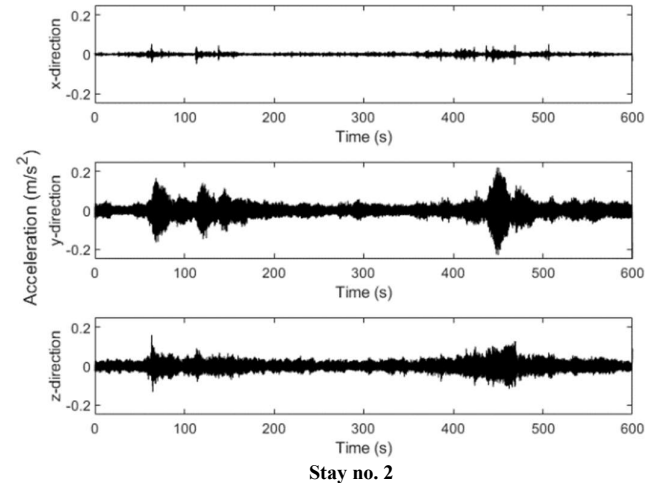
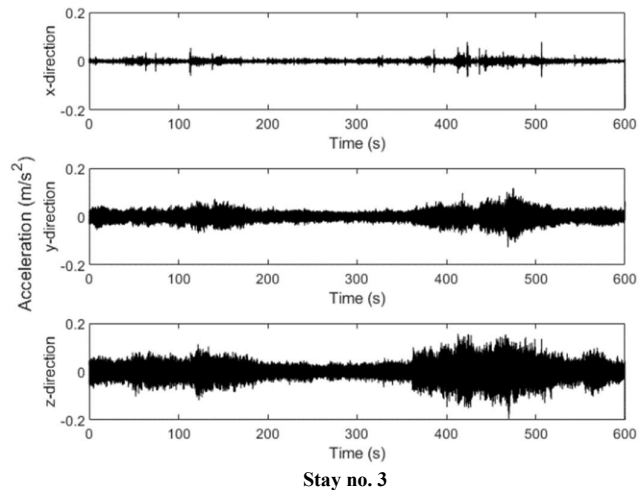
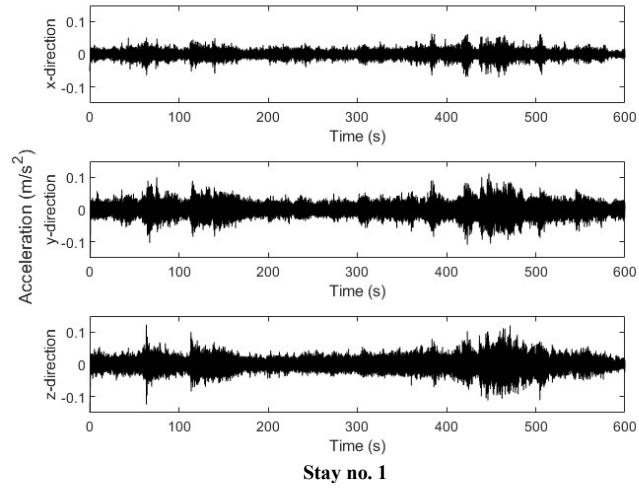
4th measurement



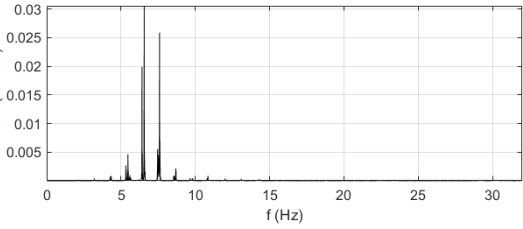
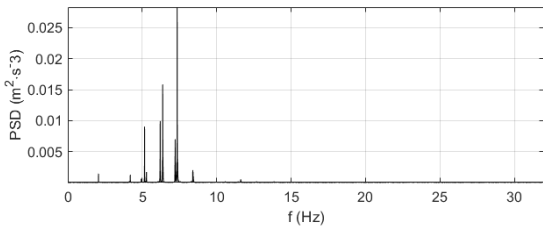
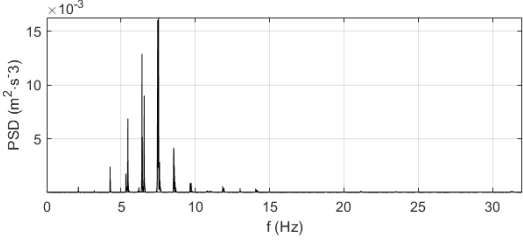
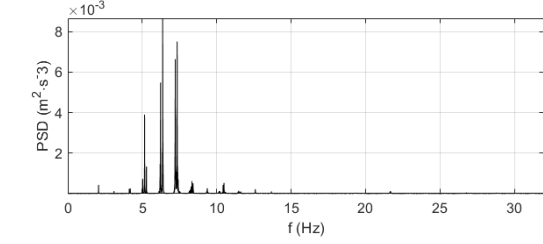
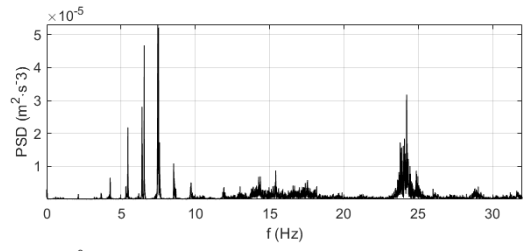
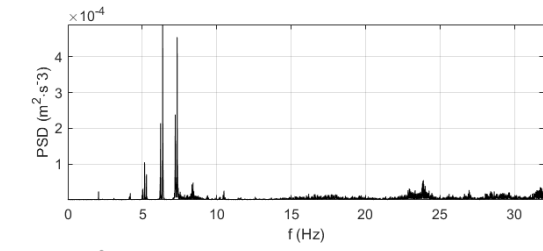
5th measurement



6th measurement

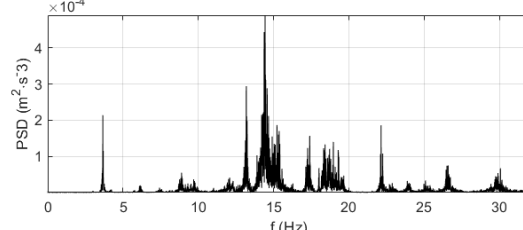
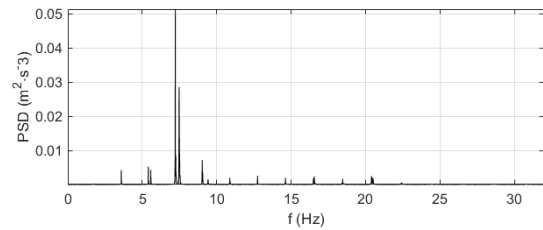
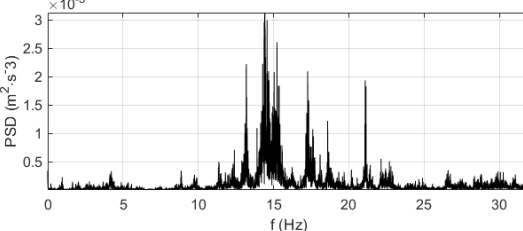
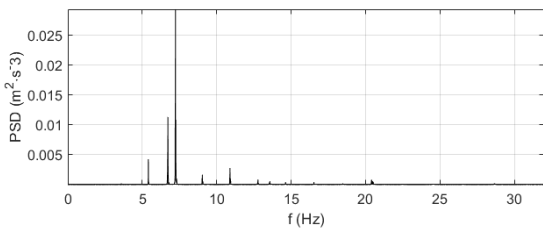
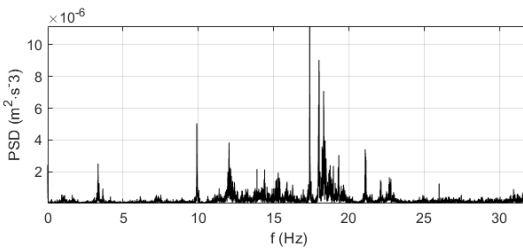
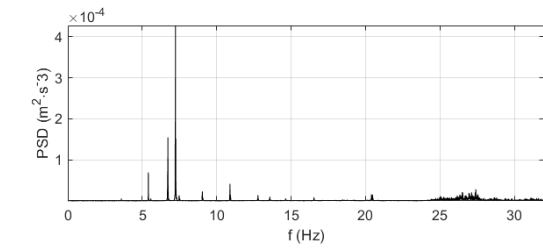


Appendix B: Power spectral density from 10/04/2019
1st measurement



Stay no. 1

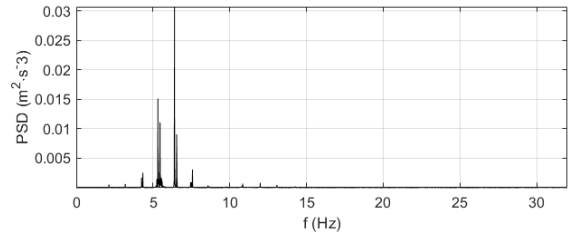
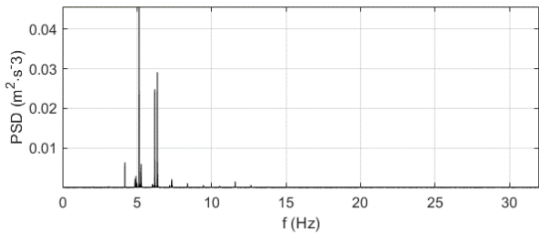
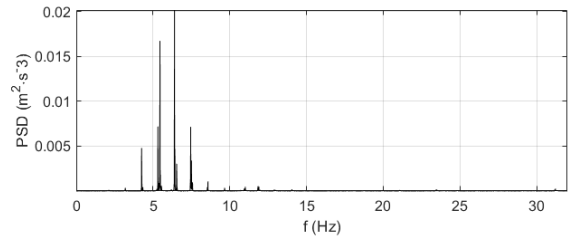
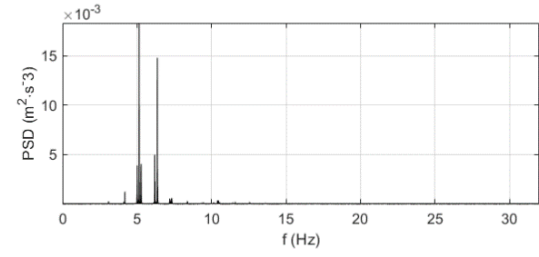
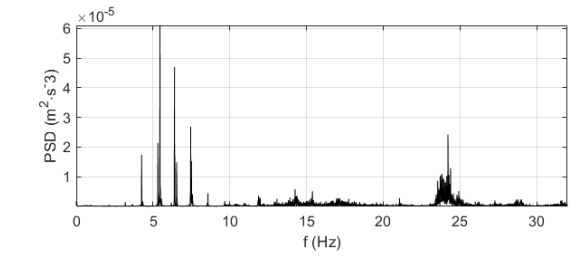
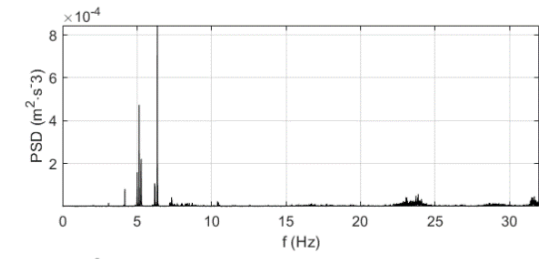
Stay no. 2



Stay no. 3

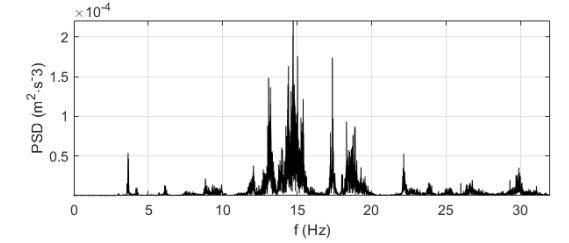
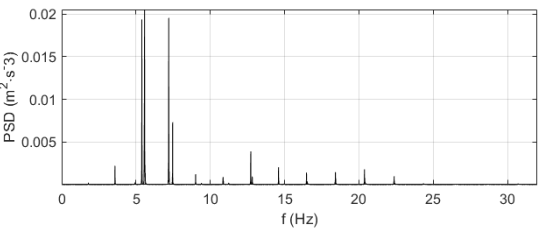
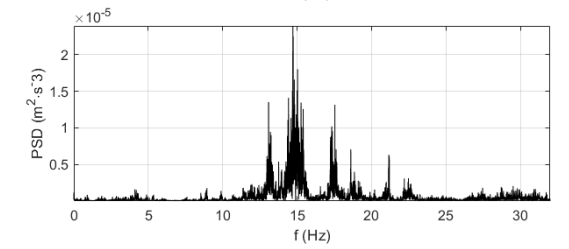
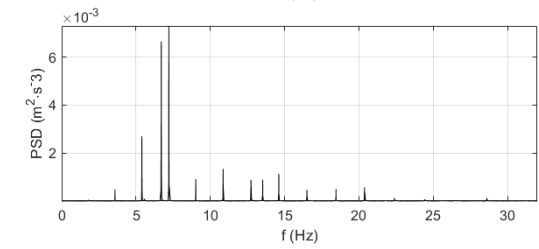
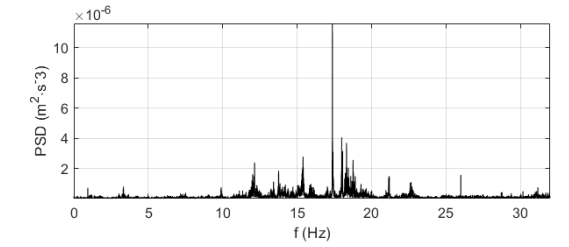
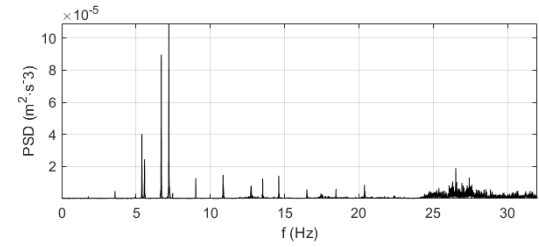
Bridge deck

2nd measurements



Stay no. 1

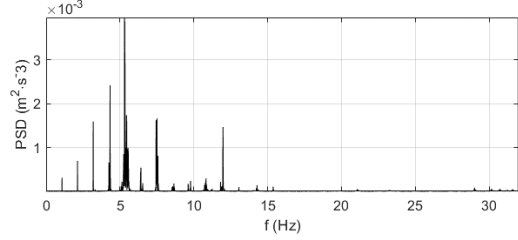
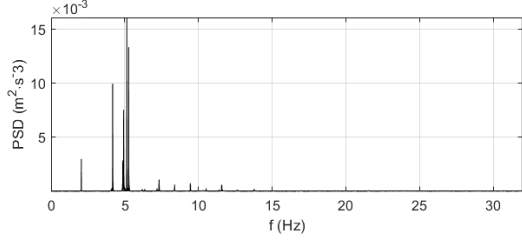
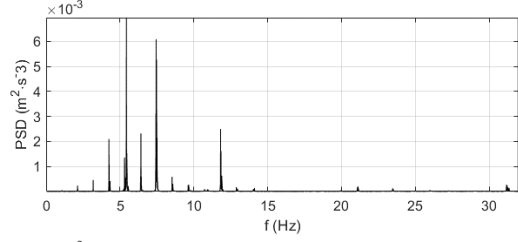
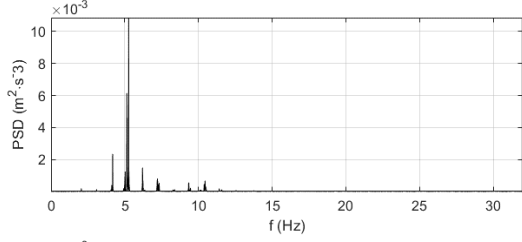
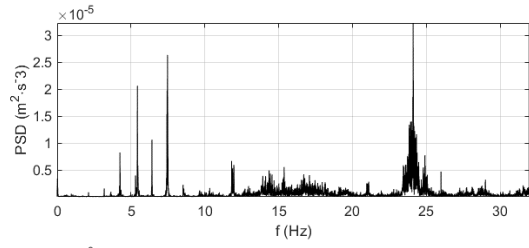
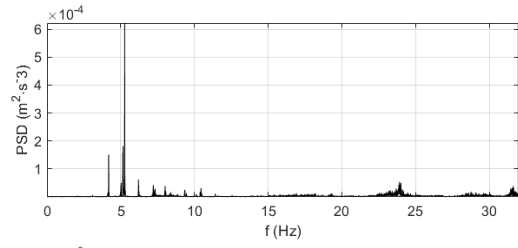
Stay no. 2



Stay no. 3

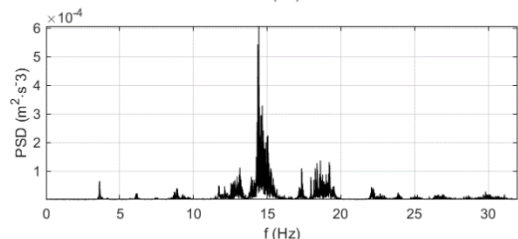
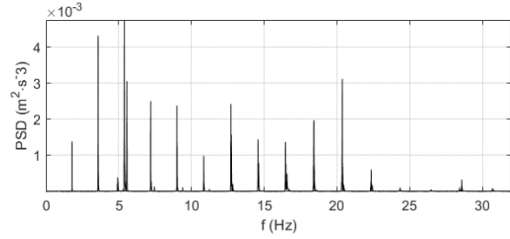
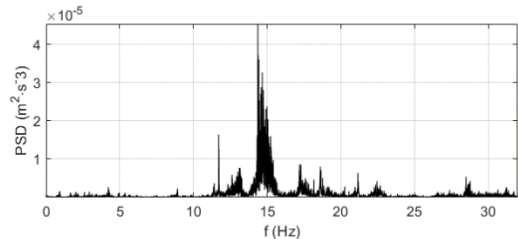
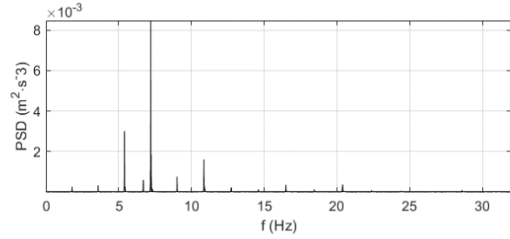
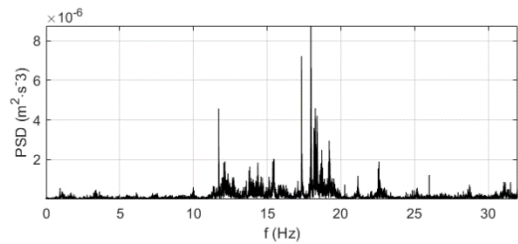
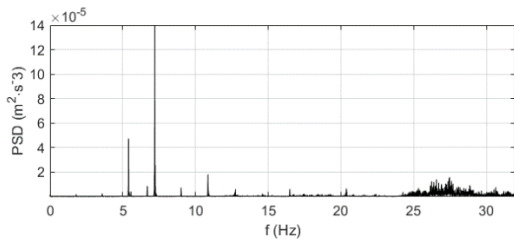
Bridge deck

3rd measurement



Stay no. 1

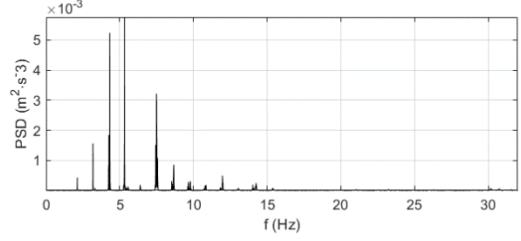
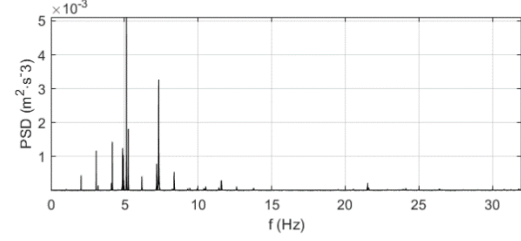
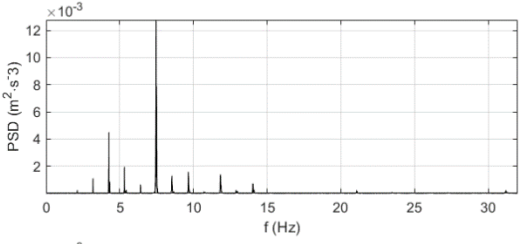
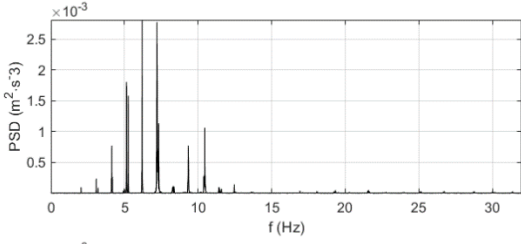
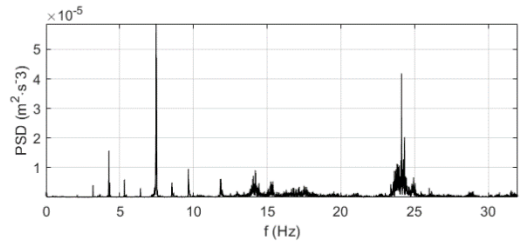
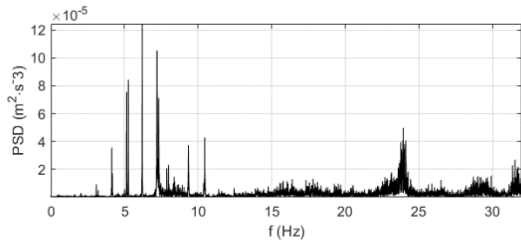
Stay no. 2



Stay no. 3

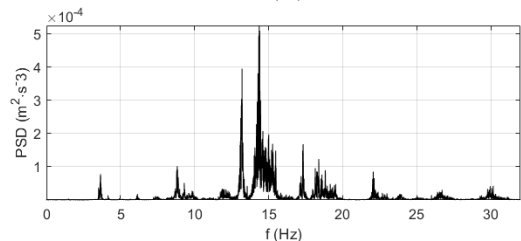
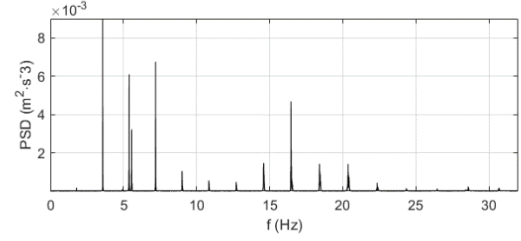
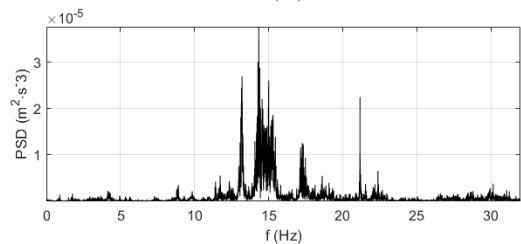
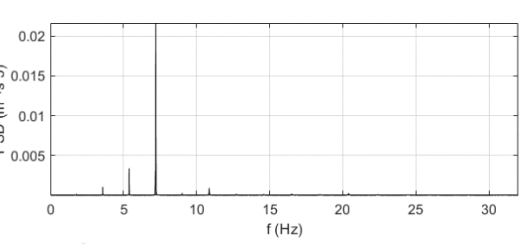
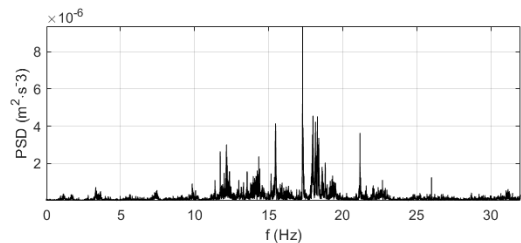
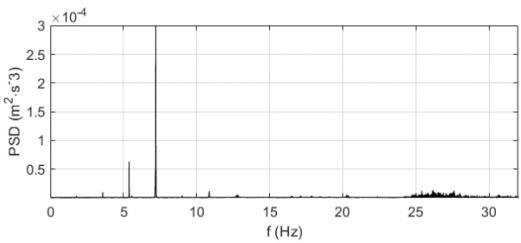
Bridge deck

4th measurement



Stay no. 1

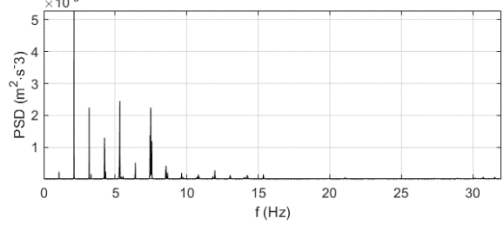
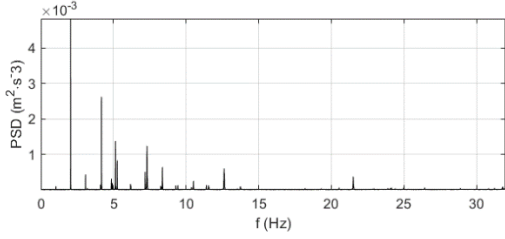
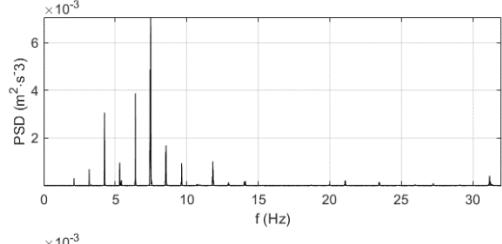
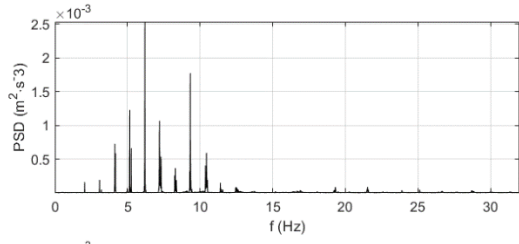
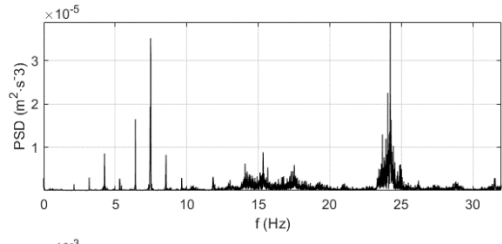
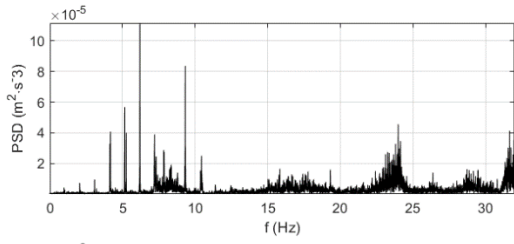
Stay no. 2



Stay no. 3

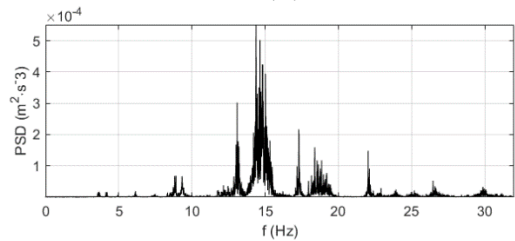
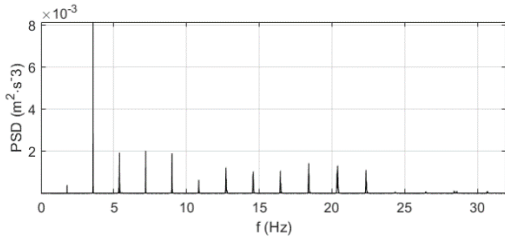
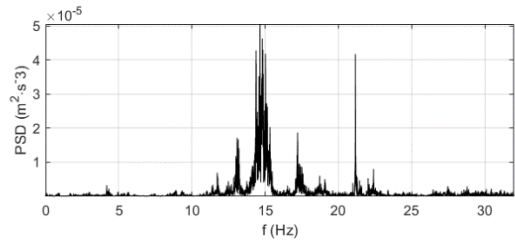
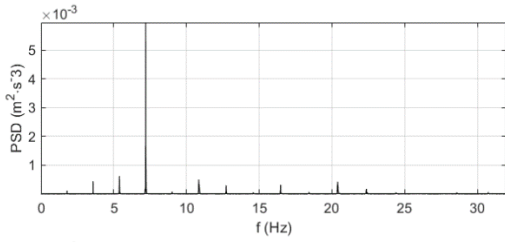
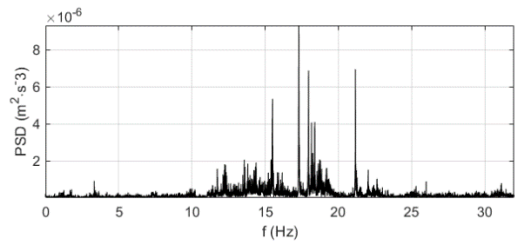
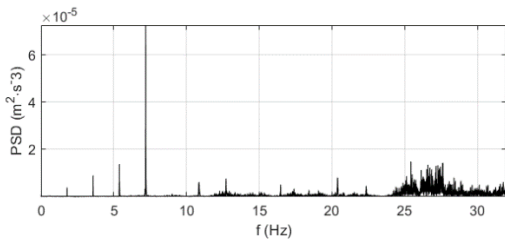
Bridge deck

5th measurement



Stay no. 1

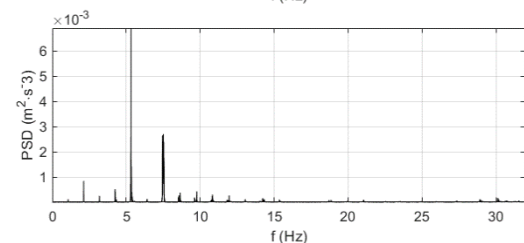
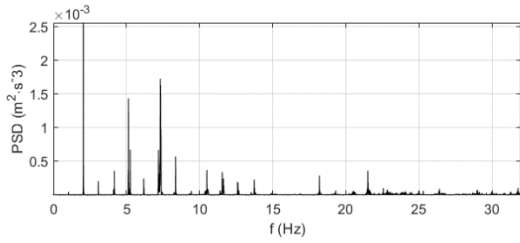
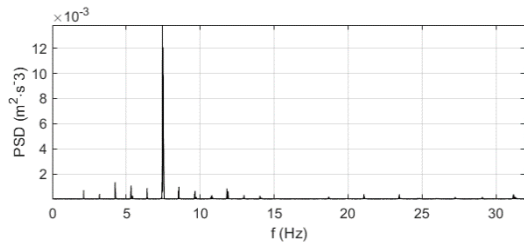
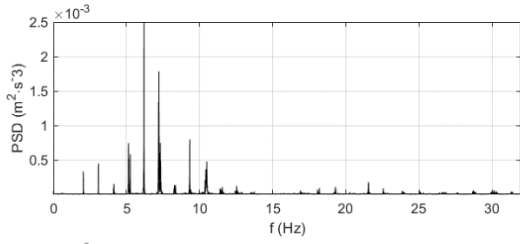
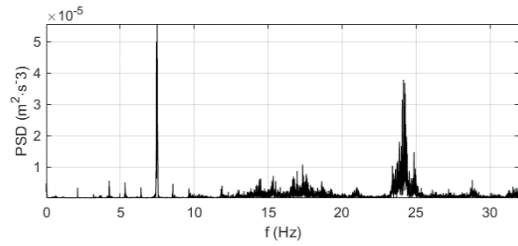
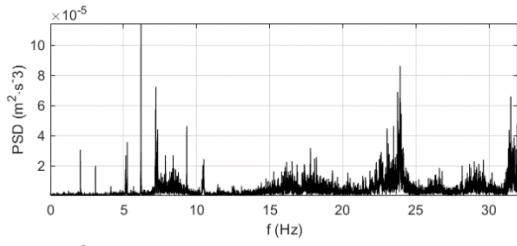
Stay no. 2



Stay no. 3

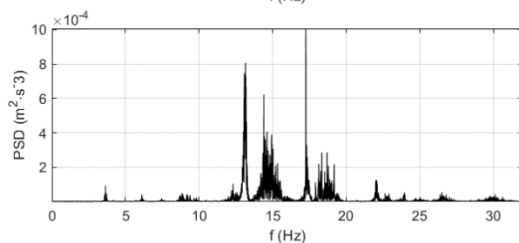
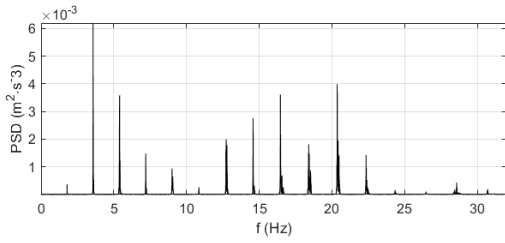
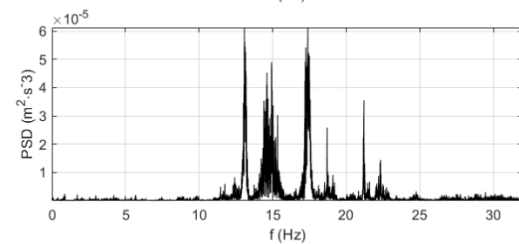
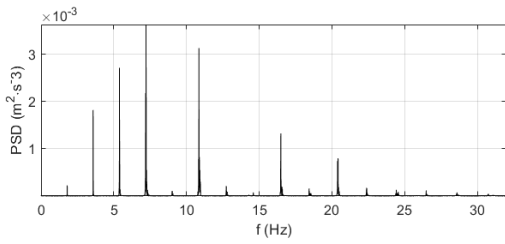
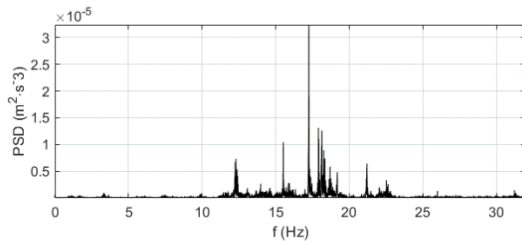
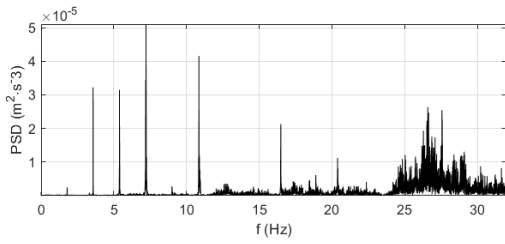
Bridge deck

6th measurement



Stay no. 1

Stay no. 2



Stay no. 3

Bridge deck

G-Link[®]-200

Wireless Accelerometer Node

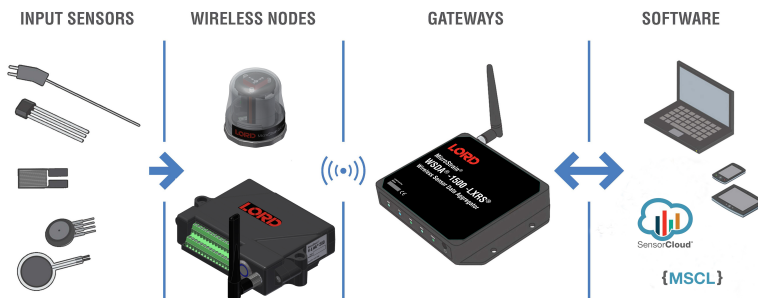


G-Link[®]-200 - ruggedized high-speed triaxial accelerometer node

LORD Sensing Wireless Sensor Networks enable simultaneous, high-speed sensing and data aggregation from scalable sensor networks. Our wireless sensing systems are ideal for test and measurement, remote monitoring, system performance analysis, and embedded applications.

The G-Link-200 has an on-board triaxial accelerometer that allows high-resolution data acquisition with extremely low noise and drift. Additionally, derived vibration parameters allow for long-term monitoring of key performance indicators while maximizing battery life.

Users can easily program nodes for continuous, periodic burst, or event-triggered sampling with the SensorConnect software. The optional web-based SensorCloud interface optimizes data aggregation, analysis, presentation, and alerts for sensor data from remote networks.



Product Highlights

- On-board triaxial accelerometer with ± 2 to ± 40 g measurement range
- Continuous, periodic burst, and event-triggered sampling
- Output raw acceleration waveform data or derived vibration parameters (Velocity, Amplitude, Crest Factor)
- LXRS protocol allows lossless data collection, scalable networks, and node synchronization of ± 50 μ s.
- 1 Sample per hour to 4096 Samples per second
- Ruggedized IP-67 rated enclosure

Features and Benefits

High Performance

- User-configurable low and high pass filters
- Extremely low noise on all axis 25μ g/ $\sqrt{\text{Hz}}$ or 80μ g/ $\sqrt{\text{Hz}}$
- High accuracy temperature sensor ± 0.1 $^{\circ}\text{C}$
- Wireless range up to 2 km (800 m typical)
- Datalog up to 8 million data points

Ease of Use

- End-to-End wireless sensing solution reduces development and deployment time
- Remote configuration, acquisition, and display of sensor data with SensorConnect
- Optional web-based SensorCloud platform optimizes data storage, viewing, alerts, and analysis.
- Easy custom integration with open-source, comprehensive communications and command library (API)

Applications

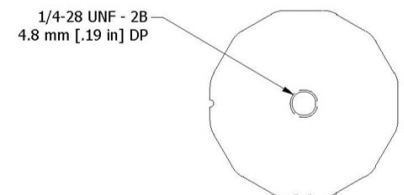
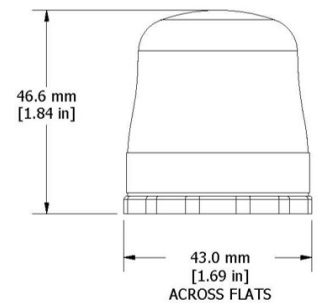
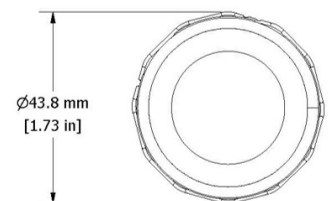
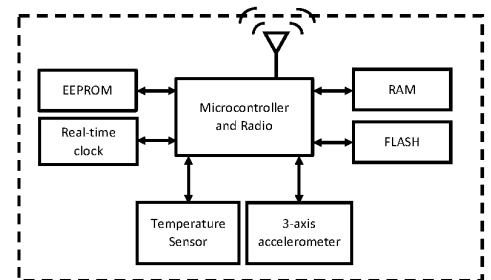
- Vibration monitoring
- Condition based maintenance (CBM)
- Impact and event monitoring
- Health monitoring of rotating components, aircraft, structures, and vehicles

Specifications

Accelerometer Channels		
	8 g	40 g
Measurement range	±2 g, ±4 g, or ±8 g configurable	±10 g, ±20 g, or ±40 g configurable
Noise density	25 µg/√Hz	80 µg/√Hz
0 g offset	±25 mg (±2 g)	±50 mg (±10 g)
0 g offset vs temperature	±.1 mg/°C (typical), ±.15 mg/°C (maximum)	±0.5 mg/°C (typical), ±0.75 mg/°C (maximum)
Integrated Sensors	Triaxial MEMS accelerometer, 3 channels	
Accelerometer bandwidth	DC to 1 kHz	
Resolution	20-bit	
Scale factor error	< 1% full-scale	
Cross axis sensitivity	1%	
Sensitivity change (temperature)	±0.01%/°C	
Anti-aliasing filter	1.5 kHz (-6 dB attenuation)	
Low-pass digital filter	26 to 800 Hz - configurable	
High-pass digital filter	Off to 2.5 Hz - configurable	
Integrated Temperature Channel		
Measurement range	-40 °C to 85 °C	
Accuracy	±0.1 °C (over full range)	
Sampling		
Sampling modes	Continuous, periodic burst, event triggered	
Output options	Acceleration, Derived channels: Velocity (IPS _{rms}), Amplitude (G _{rms} and G _{pk-pk}) and Crest Factor	
Sampling rates	1 sample/hour to 4096 samples/second	
Sample rate stability	±5 ppm	
Network capacity	Up to 128 nodes per RF channel (bandwidth calculator:) http://www.microstrain.com/configure-your-system	
Node synchronization	±50 µsec	
Data storage capacity	16 M Bytes (up to 8,000,000 data points)	
Operating Parameters		
Wireless communication range	Outdoor/line-of-sight: 2 km (ideal)*, 800 m (typical)**, Indoor/obstructions: 50 m (typical)**	
Radio frequency (RF) transceiver carrier	License-free 2.405 to 2.480 GHz with 16 channels	
RF transmit power	User-adjustable from 0 dBm to 20 dBm. Power output restricted regionally to operate within legal limits	
Power source	3 x 3.6 V, ½ AA batteries (Saft LS 14250 recommended)	
Battery input range	0.8 V to 5.5 V	
Operating temperature	-40 °C to +85 °C	
Physical Specifications		
Dimensions	46.6 mm x 43 mm x 44 mm	
Mounting	¼ - 28 UNF - 2B 4.8 mm [.19 in] DP.	
Weight	Node with 3 batteries: 122 grams	
Environmental rating	IP67	
Enclosure material	300 series stainless steel with polycarbonate cover	
Integration		
Compatible gateways	All WSDA base stations and gateways	
Software	SensorCloud, SensorConnect, Windows 7, 8 & 10 compatible	
Software development kit (SDK)	http://www.microstrain.com/software/mscl	
Regulatory compliance	FCC (USA), IC (Canada), CE (European Union), JET (Japan)	

*Measured with antennas elevated, no obstructions, no RF interferers.

**Actual range varies with conditions



LORD SENSING

LORD Corporation
MicroStrain[®] Sensing Systems
459 Hurricane Lane, Suite 102
Williston, VT 05495 USA

ph: 802-862-6629
sensing_sales@LORD.com
sensing_support@LORD.com

WSDA[®]-2000

Wireless Sensor Data Aggregator



WSDA-2000 Network-ready gateway for high-speed, sophisticated data aggregation, with J1939 CAN and Ethernet interfaces

The WSDA[®]-2000 supports LORD Sensing's latest LXRS+ wireless communication protocol and all LXRS- enabled modes, providing high-speed sampling, ± 50 microseconds node-to-node synchronization and lossless data throughput under most operating conditions.

LORD Sensing Wireless Sensor Networks enable simultaneous, high-speed sensing and data aggregation from scalable sensor networks. Our wireless sensing systems are ideal for test and measurement, remote monitoring, system performance analysis, and embedded applications.

The gateways are the heart of the LORD Sensing wireless sensing system. They coordinate and maintain wireless transmissions across a network of distributed wireless sensor nodes.



PRODUCT HIGHLIGHTS

- Compatible with LORD Sensing LXRS and LXRS+ sensor nodes
- USB and Ethernet-based gateway configures, coordinates, and collects sensor data from a scalable network of wireless sensor nodes
- Configurable to operate with a static IP, a DHCP-enabled LAN, or as a datalogger to local memory
- Push all or selected sensor data to a J1939 CAN bus
- Seamless integration with SensorCloud[™] for secure, web-based data access from around the world

FEATURES AND BENEFITS

HIGH PERFORMANCE

- Lossless data throughput and synchronized node-to-node sampling of ± 50 μ S in LXRS+ and LXRS-enabled modes
- Wireless range up to 2 km (800 m typical)

EASE OF USE

- Remote configuration, acquisition, and display of sensor data with SensorConnect[™]
- Data visualization through web-based SensorCloud portal for quick data navigation and analysis
- Easy custom integration with open-source, comprehensive communications and command library (API)
- Connect the gateway to a cellular or Wi-Fi modem for wireless connectivity to the host network

COST EFFECTIVE

- Hundreds of sensors managed from a single gateway
- Reduction of costs associated with wiring

APPLICATIONS

- Remote and web-based wireless sensor data acquisition
- Condition-based monitoring
- Equipment performance monitoring, verification, evaluation, and diagnostics
- System control

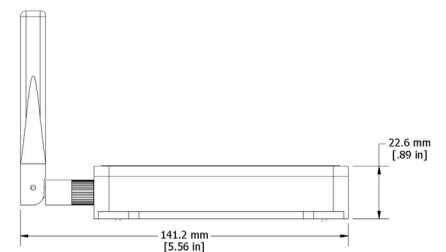
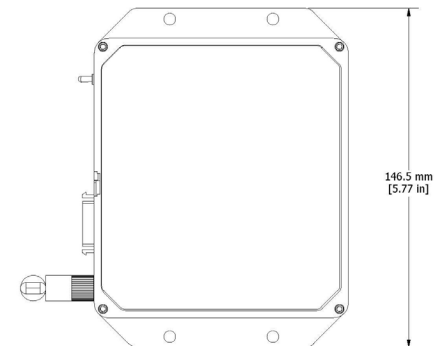
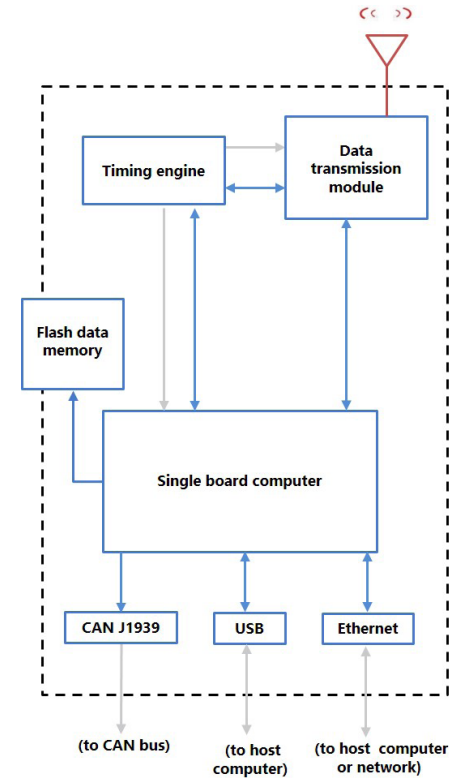
WSDA[®]-2000 Wireless Sensor Data Aggregator

Specifications

General			
Processor	ARM [®] Cortex [™] A8, 1 GHz		
Operating system	Linux		
Connectivity	Ethernet IEEE 802.3 10/100 Mbps, IEEE 802.15.4 and Proprietary wireless, J1939 CAN (output only), and USB 2.0 virtual Ethernet port		
Internet standards	HTTP, HTTPS, TCP/IP, UPnP, UDP		
IP assignment	IPV4 Static or DHCP		
Data storage memory	4 G bytes Micro SD (optional upgrade to 8 or 16 GB)		
Time synchronization	Network time protocol (NTP), Real time clock (RTC), last used, manual entry		
CAN J1939 Output			
J1939 Bit Rate	250 K bps, 500 K bps, 1 M bps		
J1939 Source	Static or dynamic via SAE Name		
J1939 Destination	Static or SAE Name		
J1939 Modes	Tunnel data to destination using PGN 0xEF00, or broadcast data values using PGNs 0xFF00 – 0xFFFF		
Standard bus termination	120 Ω		
Sampling			
Supported node sampling modes	Synchronized, low duty cycle, continuous, periodic burst, event-triggered, and datalogging		
Synchronization beacon interval	1 Hz beacon provides ± 50 µsec node-to-node synchronization		
Synchronization beacon stability	± 5 ppm		
Network capacity	Up to 2000 nodes per RF channel (& per gateway) depending on number of active channels and sampling settings. See system bandwidth calculator: http://www.microstrain.com/configure-your-system		
Operating Parameters			
Wireless Communication Range		Typical*	Ideal**
	LXRS	1 km	2 km
	LXRS+	400 m	1 km
Radio frequency (RF) transceiver carrier	License-free 2.405 to 2.480 GHz with 16 channels		
RF communication protocol	IEEE 802.15.4 and Proprietary		
RF transmit power	User-adjustable from 0 dBm to 20 dBm. Power output restricted regionally to operate within legal requirements		
Power source	9.0 to 30.0 V dc (Universal 15 V dc, 1.3 A AC/DC converter included in starter kit)		
Power consumption	2850 mW (max), 2400 mW (typ) @ 15 V		
Operating temperature	-40°C to +85°C		
Physical Specifications			
Dimensions	147 mm x 110 mm x 23 mm without antenna		
Weight	343 grams		
Enclosure material	Black anodized aluminum		
Integration			
Connectors	USB, RJ45 jack, 26 pin multi-port, 2.1mm power jack		
Communications cable	USB, Ethernet (CAT6 cable included in starter kit)		
Compatible nodes	All LORD Sensing LXRS [®] and LXRS+ nodes		
Firmware	Firmware and OS upgradeable through web interface		
Software	SensorCloud SensorConnect [™] 8.3 or newer, Windows 7, 8 & 10 compatible		
Regulatory compliance	FCC (U.S.), IC (Canada), CE (European Union)		

*Actual range varies with conditions.

**Measured with antennas elevated, no obstructions, no RF interferences.



LORD Sensing MicroStrain

459 Hurricane Lane Suite 102

Williston, VT 05495 • USA

www.microstrain.com

©2019 LORD Corporation Document 8400-0121 (Revision A). Subject to change without notice.

Customer Support Center (in United States & Canada)

Tel: +1.802.862.6629

Email: sensing_support@LORD.com

For a listing of our worldwide locations, visit LORD.com

LORD SENSING
MicroStrain

Appendix D

The code was written by Nicolò Daniotti and later edited by the author

```
-----  
  
clc; close all; clearvars;  
  
load('Bybrua_05_10min.mat'); % load the data  
data.Acc = fillmissing(data.Acc,'linear');  
fprintf(['Time:      ', data.time, '\n']) % First time step  
fprintf(['NaN : ', num2str(sum(isnan(data.Acc))), '\n']) % Number of  
NaN  
fs = data.fs; % sampling frq (Hz)  
dt = 1/fs; % time step (s)  
N = size(data.Acc,1); % Number of samples  
t = [0:N-1]*dt; % time vector
```

Time history and PSD

```
indx = 9; % Select the accelerometer and channel according to  
data.sensors  
NW = 2; % Number of segments  
nfft = round(N/NW); % NFFT points  
  
x = 9.81*data.Acc(:,indx); % Acceleration signal  
[Sx,f] = pwelch(detrend(x),nfft,round(nfft/2),nfft,fs); % PSD  
  
[b,a] = butter(8, [7/32 8/32]); %Butterworth filter  
x_filtered = filter(b,a,detrend(x)); %Filtered acceleration response  
  
figure(1);  
plot(t,detrend(x),'b'); %Plots the acceleration  
xlabel('Time (s)');  
ylabel('Acceleration (m/s^2)');  
axis tight; grid on;  
% ylim([-0.2 0.2])  
xlim([200 400]);  
  
figure(2);  
plot(t,x_filtered,'g'); %Plots the filtered acceleration  
xlabel('Time (s)');  
ylabel('Acceleration (m/s^2)');  
axis tight; grid on;  
xlim([200 400]);  
  
figure(3);  
plot(f,Sx,'k'); %Plots the PSD  
xlabel('Frequency (Hz)');  
ylabel('Amplitude (m^2\cdots^-3)');  
axis tight; grid on;
```

```
findpeaks(Sx,f,'MinPeakProminence',4e-7,'Annotate','extents') %finds
peaks of a minimum height
[pks,locs,widths,proms] = findpeaks(Sx,f); %Plots the height and
width of peak at height/2
widths;
xlim([0 2])

figure(3)
semilogy(f,Sx,'k'); %Plots the PSD with a logarithmic y-axis
xlabel('Frequency (Hz)');
ylabel('Amplitude (m^2\cdots^-3)');
axis tight; grid on;
xlim([0 10]);

A1 = rmmissing(data.Acc(:,1:3)); % 4251
A2 = rmmissing(data.Acc(:,4:6)); % 12045
A3 = rmmissing(data.Acc(:,7:9)); % 12046
A4 = rmmissing(data.Acc(:,10:12)); % 12047
```

Published with MATLAB® R2018b

Appendix E: Weather on the days of observed vibrations

	Wind direction	Wind speed m/s	Air density (hPa)	Rain (mm/hr)	Temperature °C
06.09.2006 00:00	15	0,8	1014,3	0	12,7
06.09.2006 01:00	185	1,4	1013,7	0	12,1
06.09.2006 02:00	166	1,5	1013	0	12
06.09.2006 03:00	182	1,7	1012,7	0	11,9
06.09.2006 04:00	140	2,4	1011,9	0	11,9
06.09.2006 05:00	132	2,1	1011	0	12
06.09.2006 06:00	60	0,2	1010,6	0,1	12
06.09.2006 07:00	127	1,6	1010	0,1	12,1
06.09.2006 08:00	99	1,6	1009,1	0,5	12
06.09.2006 09:00	109	1,4	1008,3	1	12,4
06.09.2006 10:00	140	0,9	1007,5	0,8	12,4
06.09.2006 11:00	114	1,3	1006,5	0,7	12,8
06.09.2006 12:00	126	4,6	1005,6	1,8	12,9
06.09.2006 13:00	84	0,6	1005,4	1,6	13,3
06.09.2006 14:00	304	2	1005	3,2	13,3
06.09.2006 15:00	108	2,8	1004,6	5,3	13,7
06.09.2006 16:00	137	2,4	1004,3	2,8	14
06.09.2006 17:00	182	4,6	1004,2	0,9	15
06.09.2006 18:00	263	5	1004,3	0,2	15,1
06.09.2006 19:00	284	8	1004,9	0,3	14,4
06.09.2006 20:00	289	6,6	1005,5	0	13,9
06.09.2006 21:00	287	4,7	1005,8	0	13,8
06.09.2006 22:00	277	5	1005,9	0	14
06.09.2006 23:00	262	2,2	1005,7	0	13,8
15.02.2014 00:00	133	9,5	987,8	0	5,6
15.02.2014 01:00	126	11,8	985	0	5,5
15.02.2014 02:00	130	10,8	983,2	0	5,6
15.02.2014 03:00	134	10,6	980,8	0	3,5
15.02.2014 04:00	125	12,1	977,6	0,2	3,7
15.02.2014 05:00	131	14,5	975,1	0,7	4,5
15.02.2014 06:00	124	14,5	974	0,9	3,6
15.02.2014 07:00	123	14,1	972,8	0,2	3,8
15.02.2014 08:00	124	11	972,1	1,3	3,9
15.02.2014 09:00	121	8,5	971,5	1	4,7
15.02.2014 10:00	149	8,7	971	1	5,4
15.02.2014 11:00	154	9,4	970,6	1,6	6,4
15.02.2014 12:00	157	9,8	970,1	0,5	6,7
15.02.2014 13:00	159	11	969,4	0,2	6,9
15.02.2014 14:00	162	10,2	969	0,2	6,3
15.02.2014 15:00	154	11,2	968,6	0,1	5,7
15.02.2014 16:00	139	10,1	968	1,3	5,7
15.02.2014 17:00	150	9,4	968,3	1,1	6,3
15.02.2014 18:00	172	9,5	968,3	2,9	6,4
15.02.2014 19:00	184	9,3	969,2	1,3	6,6

15.02.2014 20:00	193	8	970,2	1,3	6,8
15.02.2014 21:00	196	6,8	971,1	1,3	6,7
15.02.2014 22:00	188	6,8	971,8	0,1	6,3
01.11.2018 00:00	134	6,2	1011,4	0	8,2
01.11.2018 01:00	144	7,4	1011,4	0	8,3
01.11.2018 02:00	147	6,1	1011,4	0	8,2
01.11.2018 03:00	143	5,5	1011,6	0,4	8,1
01.11.2018 04:00	141	6,2	1011,4	0	8,8
01.11.2018 05:00	134	5,6	1011,2	0	9
01.11.2018 06:00	129	5,9	1011,4	0,5	8,6
01.11.2018 07:00	136	6,2	1010,8	0,1	9,1
01.11.2018 08:00	132	6,4	1010,5	0	9
01.11.2018 09:00	133	7,3	1010,1	0	9,3
01.11.2018 10:00	119	8,6	1009	0	9,9
01.11.2018 11:00	134	8,7	1008,4	0	10,2
01.11.2018 12:00	125	8,2	1008,1	0	9,9
01.11.2018 13:00	127	8,6	1007,5	0,2	10,1
01.11.2018 14:00	131	9,8	1007	0,1	10,2
01.11.2018 15:00	125	11,1	1005,8	0,3	11,2
01.11.2018 16:00	137	10,1	1006,6	0	11,1
01.11.2018 17:00	124	9,3	1006,1	0	10,7
01.11.2018 18:00	125	8,2	1006,1	0,1	10,7
01.11.2018 19:00	131	8,6	1006,1	0	11
01.11.2018 20:00	129	7,2	1006,1	0,1	10,9
01.11.2018 21:00	122	7,2	1006,4	0	10,5
01.11.2018 22:00	125	8	1006,4	0	10,7
01.11.2018 23:00	123	8,9	1006,2	0	10,5
07.12.2018 00:00	198	4,8	998,1	0	7,6
07.12.2018 01:00	198	3,3	998,4	0	7,7
07.12.2018 02:00	201	3,1	998,2	0	7,1
07.12.2018 03:00	203	3,8	998,3	0	7,1
07.12.2018 04:00	212	3,9	997,9	0	8,2
07.12.2018 05:00	190	2,9	997,7	0,1	7
07.12.2018 06:00	159	2,9	996,7	0	6,3
07.12.2018 07:00	154	3,3	995,9	0	6,7
07.12.2018 08:00	142	4	994,7	0	6,5
07.12.2018 09:00	141	3,2	994,2	0	5,9
07.12.2018 10:00	138	5,1	993,4	0	6,9
07.12.2018 11:00	128	6,1	992	0	7,6
07.12.2018 12:00	129	6,2	990,5	0	7,9
07.12.2018 13:00	125	6,5	988,5	0,1	7,4
07.12.2018 14:00	118	6,9	986,1	0,9	7
07.12.2018 15:00	100	5,9	984	1,1	6,9
07.12.2018 16:00	123	6,6	982,3	1	7,9
07.12.2018 17:00	130	7,8	981,7	0,4	7,5
07.12.2018 18:00	147	7,7	981,6	0,6	6,8

07.12.2018 19:00	164	6,1	982,1	0,2	7
07.12.2018 20:00	183	3,6	982,3	0	6,4
07.12.2018 21:00	158	4,7	982,4	0	6,3
07.12.2018 22:00	157	5	982,3	0	6,1
07.12.2018 23:00	160	3,4	982	0	6,3

Appendix F: Calculation of tensile forces in the stays

Dead load concrete cross sections:

$$w_c = A * \rho$$

Area $A=8,56 \text{ m}^2$

Density of reinforced concrete $\rho=25 \text{ kN/m}^3$

$W_c=214 \text{ kN/m}$

Dead load of steel box girder:

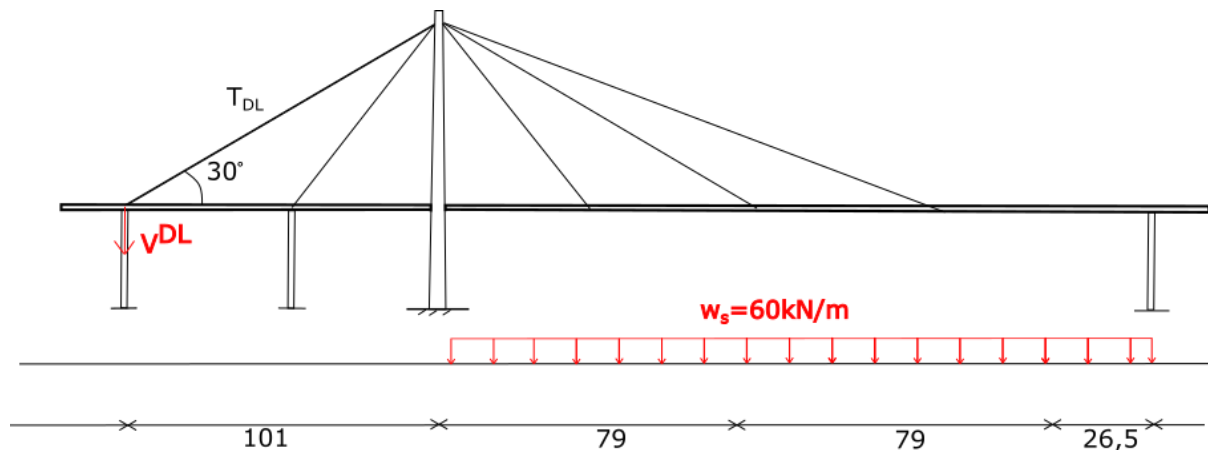
Total weight of steel structure $m=1100\ 000 \text{ kg}$

Total force $m*a=1100000 \text{ kg}*9,81 \text{ m/s}^2 = 10791 \text{ kN} \approx 11000 \text{ kN}$

$W_s=11000 \text{ kN}/185 \text{ m} = 59,5 \text{ kN/m} \approx 60 \text{ kN/m}$

Force in backstay cable calculated from Svensson [1] chapter 4.5.4.2, cable stayed bridge with side spans resting on piers. Main span loads transferred via the forestays to a concentrated backstay anchored to a hold down pier:

The 16 individual anchor cables (8 on each side) are regarded as one cable.



$$V^{DL} = 60 \text{ kN/m} * 58 \text{ m} * (79/101) = 7400 \text{ kN}$$

$$T^{DL,16} = 7400 \text{ kN} / \sin 30^\circ = 14830 \approx 15000 \text{ kN}$$

$$\text{Cable force in each individual cable } T^{DL} = 15000 \text{ kN} / 16 = 937 \text{ kN} \approx 940 \text{ kN}$$

1. Svensson, H., *Cable-stayed bridges : 40 years of experience worldwide*, in *Cable-stayed bridges : forty years of experience worldwide*. 2012, Ernst & Sohn: Zeuthen.

Appendix G: Damping ratio of each mode

Stay cable 1										
Identified frequencies					Identified frequencies					
y	f1	f2	Damping ratio	Damping ratio (%)	z	f1	f2	Damping ratio	Damping Ratio (%)	Average damping per mode (%)
	-	-			1,037	1,035	1,039	0,002	0,193	0,193
2,05	2,0477	2,058	0,003	0,251	2,053	2,049	2,055	0,001	0,146	0,199
3,083	3,0799	3,0889	0,001	0,147	3,08	3,078	3,083	0,001	0,081	0,114
4,137	4,133	4,143	0,001	0,121	4,173	4,17	4,181	0,001	0,132	0,126
5,137	5,135	5,142	0,001	0,068	4,873	4,871	4,878	0,001	0,072	0,070
5,26	5,258	5,266	0,001	0,076	5,137	5,135	5,142	0,001	0,068	0,072
6,203	6,198	6,208	0,001	0,081						0,081
Stay cable 2										
y					z					
1,063	1,058	1,065	0,003	0,329	1,07	1,065	1,075	0,005	0,467	0,398
2,12	2,117	2,126	0,002	0,212	2,12	2,118	2,124	0,001	0,142	0,177
3,19	3,182	3,193	0,002	0,172	3,183	3,181	3,189	0,001	0,126	0,149
4,267	4,264	4,269	0,001	0,059	4,327	4,325	4,331	0,001	0,069	0,064
5,26	5,311	5,319	0,001	0,076	5,327	5,324	5,331	0,001	0,066	0,071
6,407	6,404	6,424	0,002	0,156	6,39	6,387	6,412	0,002	0,196	0,176
Stay cable 3										
y					z					
1,797	1,792	1,799	0,002	0,195	1,793	1,79	1,796	0,002	0,167	0,181
3,583	3,581	3,586	0,001	0,070	3,58	3,577	3,584	0,001	0,098	0,084
5,39	5,386	5,394	0,001	0,074	5,39	5,385	5,393	0,001	0,074	0,074
7,21	7,206	7,22	0,001	0,097	7,197	7,193	7,2	0,000	0,049	0,073
9,017	9,005	9,022	0,001	0,094	9,007	9,005	9,009	0,000	0,022	0,058
10,87	10,86	10,88	0,001	0,092	10,84	10,84	10,85	0,000	0,046	0,069
Bridge deck										
y					z					
0,1533	0,15	0,1609	0,036	3,555	0,27	0,2677	0,275	0,014	1,352	2,453
0,89	0,886	0,8961	0,006	0,567	0,447	0,4442	0,4495	0,006	0,593	0,580
1,757	1,754	1,761	0,002	0,199	0,89	0,8869	0,8948	0,004	0,444	0,322
2,933	2,92	2,94	0,003	0,341	1,49	1,486	1,493	0,002	0,235	0,288
4,15	4,14	4,155	0,002	0,181	3,657	3,651	3,663	0,002	0,164	0,172
4,943	4,939	4,948	0,001	0,091	4,16	4,157	4,165	0,001	0,096	0,094
5,333	5,331	5,338	0,001	0,066						0,066